6-8-2020

Intercellular Communication in the Mouse Ovarian Follicle Analyzed by Three-Dimensional Electron Microscopy

Valentina Baena Echeverri
University of Connecticut - Storrs, valenbaenae@gmail.com

Intercellular Communication in the Mouse Ovarian Follicle Analyzed by Three-Dimensional Electron Microscopy

Valentina Baena Echeverri, PhD
University of Connecticut, 2020

Throughout follicle development, oocytes and somatic granulosa cells depend on each other for proper development. Granulosa cells provide nutrients and other small molecules that govern the meiotic cycle of the oocyte. cGMP, produced by the natriuretic peptide receptor 2 (NPR2) in the granulosa cells, diffuses through gap junctions across the many cell layers of the follicle until it reaches the oocyte. High levels of cGMP in the oocyte keep it in meiotic arrest until luteinizing hormone, which binds to its receptor expressed on the outer-most granulosa cells, inactivates NPR2, causing cGMP levels to drop and meiosis to resume in the oocyte. Without proper communication of these cells, the oocyte does not develop properly and meiosis resumes spontaneously. Transzonal projections (TZPs) are thin cytoplasmic extensions sent by cumulus cells that traverse the zona pellucida and become the means for direct communication between the somatic cells and the oocyte. In this dissertation, we used large-volume three-dimensional electron microscopy to analyze TZPs in antral follicles. This study revealed the intricate network that TZPs make to connect with each other and with the oocyte. We also localized the LH receptor and NPR2 proteins in-vivo and provide new ideas for how these two proteins interact with each other across cells. Intercellular communication in the ovarian follicle is crucial for various functions that ultimately lead to a healthy fertilizable oocyte. Uncovering the mechanisms for this communication is vital for our understanding of human reproduction.

Intercellular Communication in the Mouse Ovarian Follicle Analyzed by Three-Dimensional Electron Microscopy

Valentina Baena Echeverri

B.S., Lindenwood University, 2013

A Dissertation

Submitted in Partial Fulfillment of the

Requirements for the Degree of

Doctor of Philosophy

at the

University of Connecticut

2020

APPROVAL PAGE

Doctor of Philosophy Dissertation

Intercellular Communication in the Mouse Ovarian Follicle Analyzed by Three-Dimensional Electron Microscopy

Presented by

Valentina Baena Echeverri, B.S.

Major Advisor_____

Mark Terasaki, Ph.D.

Associate Advisor_____

Laurinda Jaffe, Ph.D.

Associate Advisor_____

Ann Cowan, Ph.D.

Associate Advisor_____

Siu-Pok Yee, Ph.D.

Associate Advisor_____

Kimberly Dodge-Kafka, Ph.D.

University of Connecticut

2020

PREFACE

Portions of this dissertation have been published:

Baena, V., and Terasaki, M. (2019). Three-dimensional organization of transzonal projections and other cytoplasmic extensions in the mouse ovarian follicle. Scientific Reports *9*, 1262.

Baena, V., Schalek, R.L., Lichtman, J.W., and Terasaki, M. (2019). Serial-section electron microscopy using automated tape-collecting ultramicrotome (ATUM). Methods in Cell Biology. *152*, 41–67.

Baena, V., Owen, C.M., Uliasz, T.F., Lowther, K.M., Yee, S.-P., Terasaki, M., Egbert, J.R., and Jaffe, L.A. (2020). Cellular heterogeneity of the LH receptor and its significance for cyclic GMP signaling in mouse preovulatory follicles. Endocrinology (*in press*). And BioRxiv 2020.02.06.937995.

ACKNOWLEDGEMENTS

This dissertation is dedicated to my father, Jorge Baena, who passed away just a few months before the completion of this dissertation. Without a formal scientific education, he taught me how be a scientist from my early years by encouraging me to be curious and observe things closely. Seeing me become a scientist was his great joy.

I also dedicate this dissertation to my mother, Isabel Echeverri, who has supported me with unconditional love through every step of my life.

I would like to thank my entire family, but especially my three aunts, Ana Maria Ocampo, Luz Angela Baena, and Martha Lucia Baena. Without their support and hard work, I would not have been able to complete my undergraduate studies in the USA and may not have had a chance to join a Ph.D. program. I would also like to thank my cousins Felipe, Juan Pablo, Alejandro, and Mateo. Our sibling-like bond has been my motor through the hardest times.

I thank my mentor, Mark Terasaki for teaching me everything I know and for introducing me to my now favorite field of electron microscopy. I am very lucky for having had the opportunity to do science alongside him and learn his unique approach to scientific questions. I would also like to thank Laurinda Jaffe for always being willing and happy to answer my questions, discuss ideas and results, and for her unconditional support towards my all-around well being.

I would like to thank my friends who I had the luck to meet in this program and who undoubtedly will now be life-long friends: Ninna Shuhaibar, Ashley Russo, and Mariam George, for making grad school an unforgettably fun experience through their friendship. I also thank my

boyfriend, Jonathan Lovas, for his unconditional love and support during my last year of graduate school.

Lastly, I would like to thank the great mentors I have encountered throughout my graduate studies for passing so much of their knowledge with patience and passion onto me: Rachael Norris, Leia Shuhaibar, Jeremy Egbert, Giulia Vigone, Tracy Uliasz, Melanie Fisher, Maya Yankova, and Arthur Hand. Thank you.

TABLE OF CONTENTS

LIST OF FIGURES

Chapter 4

Chapter 5

ABBREVIATIONS

TZPs	Transzonal projections
NPR2	Natriuretic peptide receptor 2
LH	Luteinizing hormone
LHR	Luteinizing hormone receptor
cAMP	Cyclic adenosine monophosphate
cGMP	Cyclic guanosine monophosphate
GPR3	G-protein coupled receptor 3
PDE3A	Phosphodiesterase 3A
FRET	Förster resonance energy transfer
EGF	Epidermal growth factor
EGFR	Epidermal growth factor receptor
FSH	Follicle stimulating hormone
FSHR	Follicle stimulating hormone receptor
PKA	Protein kinase A
ATUM	Automated Tape-Collecting Ultramicrotome
TGF-β	Transforming growth factor-beta
GDF-9	Growth differentiation factor-9
BMP-15	Bone morphogenic protein-15
DPP	Decapentaplegic
hCG	Human chorionic gonadotropin hormone
PMSG	Pregnant mare serum gonadotropin hormone
DAB	3,3’-diaminobenzidine

Chapter 1

Introduction

I. The mammalian ovarian follicle

Structure and cellular organization

The basic unit of the mammalian ovary is the ovarian follicle. An ovarian follicle consists of an oocyte that is surrounded by somatic cells, all of which are enclosed by a basement membrane (referred to as basal lamina from here on). The size of the follicle changes drastically as follicle development progresses (Fig. 1.1). The ultimate size of the preovulatory follicle is proportional to the size of the animal and thus greatly variable. In mice the diameter of a preovulatory follicle is ~400 μm, in humans ~2 cm, and in a large animal such as a rhinocerous, it is ~12 cm (Bächler et al., 2014). The number of somatic cells that surround the oocyte also changes drastically based on the stage of development of the follicle, from ~5 cells in a primordial follicle (Fig. 1.1A) to ~1000 cells in preovulatory follicles in mice (Griffin et al., 2006) (Fig. 1.1D).

In the preovulatory stage (the last stage of follicle development), the somatic cells surrounding the oocyte have differentiated to form 3 different sub-types (Fig. 1.1D). The cells directly adjacent to the oocyte are known as cumulus granulosa cells, and the cells lining the inside of the basal lamina are known as mural granulosa. These are further divided into inner and outer mural granulosa cells based morphologically on their proximity to the basal lamina and genetically by the expression of specific markers (Lipner and Cross, 1968; Wigglesworth et al., 2015). At the preovulatory stage, a fluid-filled cavity known as the antrum is very prominent. The antrum begins to form at the secondary stage of follicle development, when two layers of granulosa cells surround the oocyte, and it continues to expand exponentially. The great variation in follicle size across species is primarily driven by an increase in the follicular fluid volume

found in the antral cavity, while the thickness of the mural granulosa cell layer remains fairly constant across species (Bächler et al., 2014).

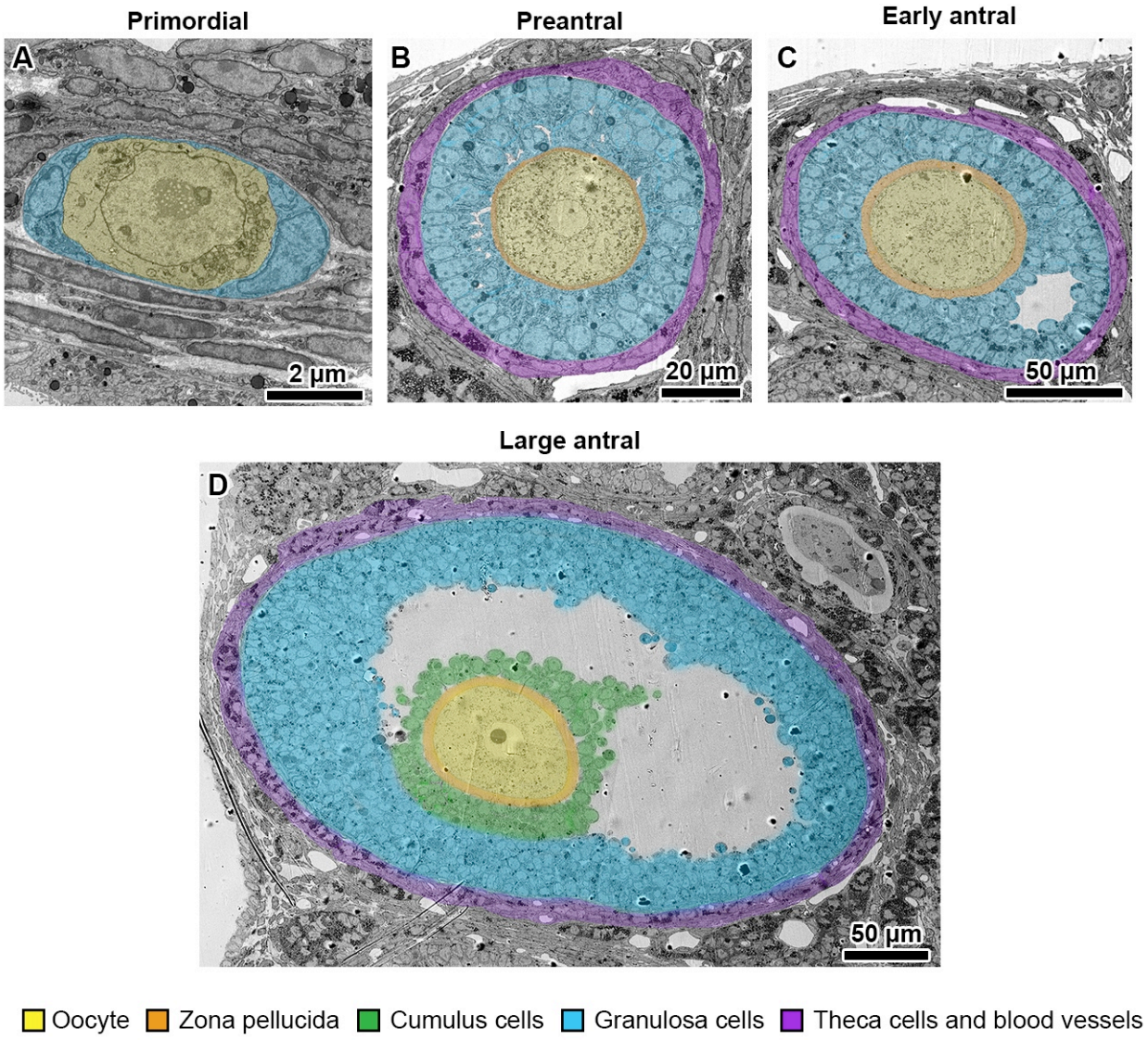

Figure 1.1. Follicle development. Electron micrographs showing follicles at different developmental stages in a 25-day old mouse ovary. **(A)** Primordial follicle consisting of a small immature oocyte surrounded by a few flat somatic cells. **(B)** Preantral follicle showing a layer cuboidal granulosa cells and a second layer that is starting to form. The zona pellucida around the oocyte is thin as it is still being deposited. Theca cells have been recruited at this stage. **(C)** Early antral follicle, marked by the beginning of the formation of the antral cavity (white space on the lower right). This follicle has an almost fully-grown oocyte and zona pellucida. **(D)** Large antral (also called Graafian) follicle consisting of a fully-grown oocyte that is meiotic competent, differentiated cumulus cells, and a prominent antral cavity.

On the outside of the follicle, adjacent to the basal lamina, two layers of theca cells are found. Theca cells play the important role of producing androgens, which are then transformed into estrogens by the granulosa cells (Fortune and Armstrong, 1978; Richards et al, 2018). Embedded within these layers are blood vessels, immune cells, and other components of connective tissue that support follicle structure and provide nutrients to the inside of the follicle.

This structure of the ovarian follicle poses an interesting biological challenge; unlike most tissues, the inside of the ovarian follicle is not infiltrated by blood vessels. During the process of folliculogenesis (the growth and development of a follicle and its oocyte prior to ovulation), all the nutrients and hormones carried in the blood are delivered to the outside of the follicle by the blood vessels found in the theca cell layers. Some of these nutrients and hormones regulate important functions in the oocyte, but in many cases, the oocyte does not have receptors to sense them directly. In such cases, the oocyte relies entirely on the granulosa cells around it to sense molecules from outside and within the follicle and then send secondary signals to it. A specific example of this is described in the next section of this introduction, and in Chapter 4 of this dissertation.

Intercellular communication within the follicle.

How signals are transmitted across these ~10 cell layers from the outside of the follicle to the oocyte remains an active research interest in reproductive biology. One of the ways signals are transmitted throughout the follicle is through gap junctions. Numerous gap junctions primarily composed of connexin-43 connect all the granulosa cells to each other (Mayerhoferand and Garfield 1995), and gap junctions primarily composed of connexin-37 (possibly in

combination with connexin-43) connect cumulus cells to the oocyte (Simon et al., 1997; Simon et al., 2006). These gap junctions are crucial for transmitting secondary messengers, metabolites, ions, and other molecules less than 1 kDa in size (Bruzzone et al., 1996; Kidder and Mhawi, 2002).

Signals are also transmitted extracellularly across these cell layers, largely aided by the antral fluid. As the follicle develops, granulosa cells secrete molecules such as hyaluronan and proteoglycans (Clarke et al., 2006; Bellin et al., 1983; Yanagishita et al., 1983). Some of these molecules are too large (>100 kDa) to escape from within follicle due to the basal lamina (also referred to as the blood-follicle barrier), and instead concentrate in the follicular fluid. This leads to the formation of an osmotic gradient in the follicular fluid, which draws in fluid from the outside the follicle (Rodgers and Irving-Rodgers, 2010; Gosden et al., 1988). A wide variety of factors have been found in the follicular fluid, including hormones, growth factors, proteins, and sugars (Revelli et al., 2009), all of which can participate in the relay of messages between granulosa cells and the oocyte (Park et al., 2004; Eppig, 1994).

Tranzonal projections connect granulosa cells to the oocyte.

Gap junction formation requires the cell membranes from the two cells involved to be in direct contact with each other so that their channel proteins (connexins) can interact and form the gap junction plaque (Evans and Martin, 2002). The requirement of cumulus cells and the oocyte to remain in direct apposition with each other becomes hindered in the secondary stage of follicle development, when the oocyte begins to deposit a glycoprotein-rich matrix called the zona pellucida.

The zona pellucida is important for fertilization of the oocyte and early embryonic development of the zygote (Hartman et al., 1972; Dean, 1992), but within the follicle, it acts as a physical barrier that separates the cumulus cell bodies and the oocyte, impeding the formation of direct gap junction plaques between each other. In the presence of the zona pellucida, cumulus cells maintain their communication with the oocyte by sending cytoplasmic projections across it (Motta et al., 1994; Clarke, 2018) (Fig. 1.2). These projections, known as transzonal projections (TZPs), are primarily actin-based but a minority of them is tubulin-based (Albertini and Rider, 1994) (Fig. 1.3A-B). Gap junctions and adherens junctions have been detected at their tips where they make contact with the oocyte (Anderson and Albertini, 1976; Mora et al., 2012), making them crucial structures for the passage of secondary messengers, nutrients, and any other signal that is normally transmitted across gap junctions between the granulosa cells of the follicle and the oocyte.

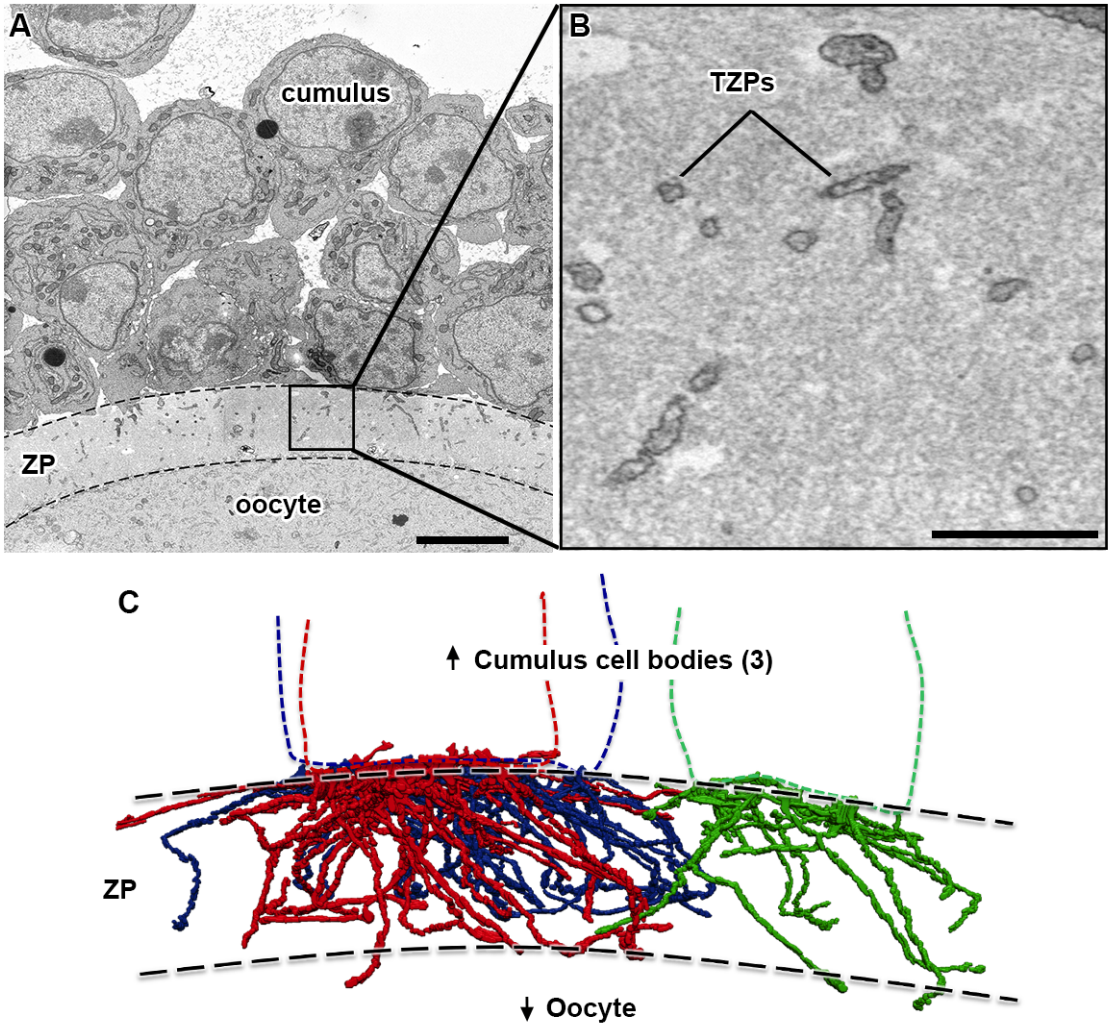

Figure 1.2. Tanszonal projections seen by electron microscopy. (A) Electron micrograph of a cross-section through cumulus cells, zona pellucida, and oocyte. **(B)** High-magnification view of the square marked in (A) showing TZPs in cross-section. **(C)** Reconstruction of every TZP sent by 3 cumulus cells. TZPs were segmented from 405 serial electron micrographs. ZP, zona pellucida. Scale bars: (A) 5 µm, (B) 1µm.

The large density of TZPs in the zona pellucida, and their small size has made molecular studies of TZPs challenging, as individual TZPs are hardly resolved by light microscopy, and electron microscopy cannot provide information on their dynamics. Notable progress in understanding the molecular machinery that make-up and regulate TZPs has been made by studying them in small follicles or in isolated cumulus-oocyte complexes that were removed from their innate follicle environment and cultured under controlled conditions. From one such

study, a predicted timeline of TZP dynamics was inferred (El-Hayek et al., 2018). Actin-labeled TZPs were counted at different stages of oocyte growth, showing that actin-based TZPs increase in number as the oocyte grows (Fig. 1.3C). This study provided the first experimental evidence that TZPs may be dynamic structures, possibly growing and retracting throughout the course of follicle development. Conversely, the number of tubulin-based TZPs does not increase, suggesting that these remain stable and attached to the oocyte continuously (Fig. 1.3C).

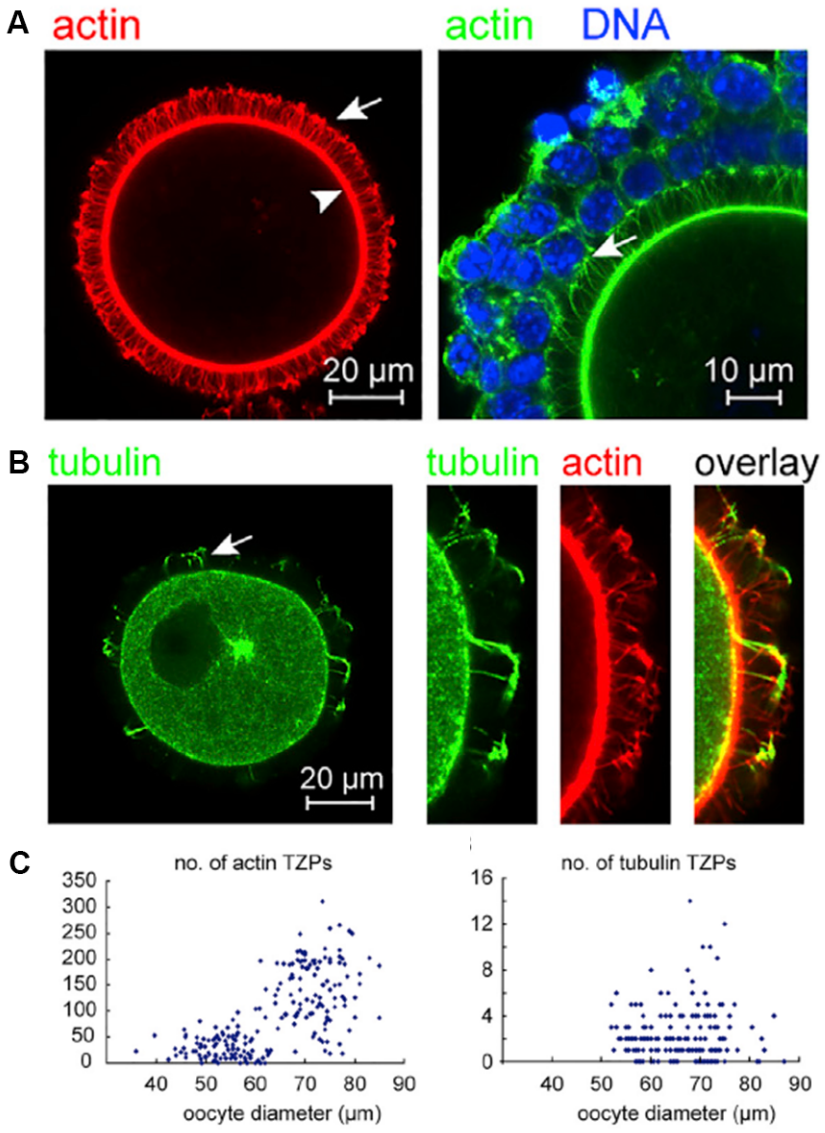

Figure 1.3. Tanszonal projections seen by fluorescence microscopy. (A) Left: TZPs (arrow) embedded in the zona pellucida were labeled with phalloidin. The cumulus cells were removed to enhance the observation of TZPs.

The oocyte cortex is marked by the arrowhead. Right: A granulosa-oocyte complex showing TZPs labeled with phalloidin. **(B)** Oocytes and TZPs stained with anti-tubulin and phalloidin. Most TZPs are actin-rich, some contain tubulin (arrow), and some contain both (overlay). **(C)** The number of actin-based TZPs increases as the oocyte gets larger whereas the number of tubulin-based TZPs remains the same. Oocytes and TZPs at different stages of growth were labeled for actin or tubulin and the number of TZPs around the periphery of the oocyte were manually counted. Adapted from El-Hayek et al., 2019.

In Chapter 3 of this dissertation, we add important information about TZPs by providing a first-ever view of their three-dimensional organization using serial section electron microscopy (Baena and Terasaki, 2019) (Fig. 1.2). Structural studies such as ours complement mechanistic studies such as the one described above by filling the gap in our understanding of how TZPs are organized, and thus creating new ideas for biochemical, in-vivo, and in-vitro research of TZPs.

II. The meiotic cycle of the mammalian oocyte

Before ovulation, oocytes are arrested in meiosis

Mammalian oocytes start meiosis during embryonic development but become arrested in prophase I shortly after (Bromfield and Piersanti, 2019). This arrest is maintained until the female begins the reproductive stage of her life cycle. Starting in puberty and ending in menopause, oocytes resume meiosis in preparation for fertilization in a highly controlled manner (Holt et al., 2013; Jaffe and Egbert 2017). The resumption of meiosis is initiated by luteinizing hormone (LH), released from the anterior pituitary in a surge-like manner during each normal reproductive cycle. Its action is described below.

Meiotic arrest of the fully-grown oocyte is maintained by high levels of cyclic adenosine monophosphate (cAMP) made in the oocyte by an adenylyl cyclase linked to a constitutively active G-protein coupled receptor known as GPR3 (Horner et al. 2003, 1985; Mehlmann, 2014). Since the adenylyl cyclase is continuously active, cAMP levels in the oocyte are controlled by its

breakdown rate. Phosphodiesterase 3A (PDE3A) breaks down cAMP in the oocyte (Masciarelli et al., 2004). PDE3A activity is kept low during meiotic arrest by another second messenger, cyclic guanosine monophosphate (cGMP), which competitively inhibits PDE3A (Hambleton et al., 2005; Vaccari et al., 2009)), keeping the oocyte in meiotic arrest in this way (Norris et al., 2009; Shuhaibar et al., 2015).

Granulosa cells control cGMP production to regulate the meiotic cycle of the oocyte

cGMP is made by the guanylyl cyclase known as natriuretic peptide receptor 2 (NPR2) or guanylyl cyclase B. Localization of NPR2 mRNA has shown that it is most highly expressed in the cumulus cells, less highly in mural granulosa cells, and not expressed by the oocyte (Zhang et al., 2010). Imaging of cGMP dynamics by Förster resonance energy transfer (FRET) confocal microscopy has shown that upon treatment with LH, cGMP levels drop due to inactivation of NPR2 (Egbert et al., 2014). The decrease of cGMP is first in the outer mural granulosa cells, then in the cumulus cells, and by 10 minutes after LH, cGMP in the oocyte falls to 50% of its original concentration (Shuhaibar et al., 2015).

When NPR2 is mutated to remain constitutively active, and thus cGMP levels remain high even in the presence of LH, meiotic resumption of the oocyte after LH is delayed from 2-6 hours in wildtype follicles, to 8-12 hours in NPR2 mutant follicles (Shuhaibar et al., 2016). Interestingly, these oocytes still resume meiosis, suggesting and confirming that there are redundant mechanisms that can lead to the resumption of meiosis of the oocyte before fertilization. One of these mechanisms is mediated by Epidermal Growth Factor (EGF)-like growth factors epiregulin and amphiregulin. Production and secretion of these factors by

granulosa cells increases in the follicle after treatment with LH (Park et al., 2004), and treatment of follicles with exogenous epiregulin or amphiregulin causes resumption of meiosis of the oocyte via a decrease in cGMP (Norris et al., 2010; Liu et al., 2014).

III. Hormones that regulate the meiotic cycle of the oocyte

The role of hormones in the mammalian reproductive cycle.

The female reproductive cycle is synchronized by 4 key hormones: estrogen and progesterone, which are both made in the ovary, and follicle stimulating hormone (FSH) and LH, which are made in the anterior pituitary gland in the brain (Hawkins and Matzuk, 2008; Richards and Pangas, 2010). These hormones are transported in the blood throughout the whole body, performing their endocrine function in this way and thus regulating each other. FSH rises early in the reproductive cycle and acts on granulosa cells to stimulate proliferation, causing follicles to grow. Granulosa cells produce estrogen in response to FSH; consequently, as granulosa cells proliferate, estrogen levels rise. When estrogen reaches a certain threshold level, a release of LH is triggered (known as the LH surge). LH acts on preovulatory follicles to initiate the resumption of meiosis of the oocyte and the entire ovulatory process of the follicle, which results in the ejection of the oocyte from within the ovary. Upon ovulation, the granulosa cells that remain in the ovary switch to mainly produce progesterone and collectively become the corpus luteum. Progesterone from the corpus luteum supports early pregnancy and delays the start of the next reproductive cycle in the case that the oocyte is fertilized. If there is no fertilization or implantation of the embryo, the corpus luteum degenerates, and the next cycle begins (Hunzicker-Dunn and Mayo, 2006).

In addition to causing follicle growth, FSH acts on the outer mural granulosa cells of preovulatory follicles to stimulate the expression of the LH receptor (LHR) (Bortolussi et al., 1977; Eppig et al., 1997). In this way, only preovulatory follicles respond to the LH surge, and not smaller follicles which may have immature oocytes. However, it is not well understood why only the outer mural granulosa cells of preovulatory follicles express the LHR, and not inner mural granulosa cells or mural granulosa cells of smaller follicles, all of which express the FSH receptor (FSHR) (Camp et al., 1991; Hardy et al., 2017).

LH restarts meiosis in the oocyte and initiates the process of ovulation.

LH binding to its receptor, a 7-transmembrane G protein-coupled receptor, causes the activation of an adenylyl cyclase through a G_s protein. This initiates a variety of downstream signals through the cAMP-dependent protein kinase A (PKA) (Ascoli et al., 2002). One of the specific events that results from LHR activation is the follicle-wide decrease in cGMP, which as mentioned above, leads to the resumption of meiosis of the oocyte (Fig. 1.4). Two mechanisms have been shown to be involved in this process: 1) the dephosphorylation and inactivation of NPR2 through an incompletely understood mechanism that is gap junction-dependent (Robinson et al., 2012; Egbert et al., 2014; and Chapter 4 of this dissertation). 2) Increased secretion of EGF-like ligands amphiregulin and epiregulin by granulosa cells, which act in a paracrine fashion to activate EGF receptors (EGFR) and downstream signals in other granulosa cells, possibly transported by the follicular fluid (Park et al., 2004; Conti et al., 2012). The specific mechanisms by which LHR activation causes the dephosphorylation of NPR2 and how EGFR activation leads to a decrease in cGMP are not yet fully understood.

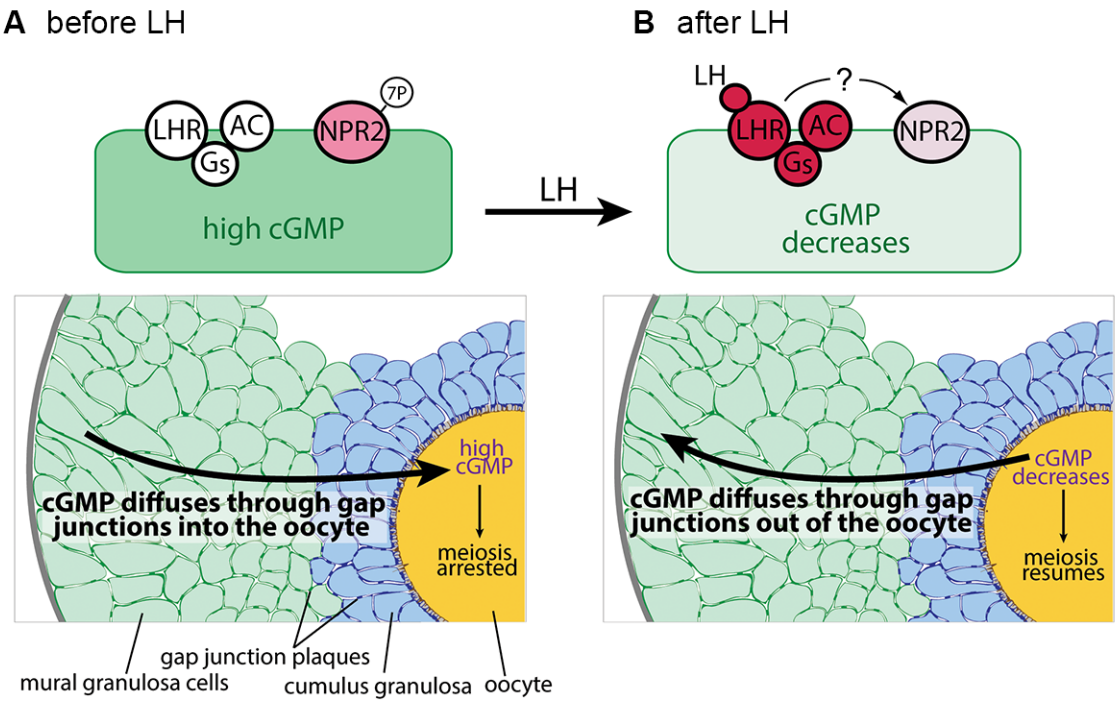

Figure 1.4. cGMP from the granulosa cells controls the meiotic cycle of the oocyte. (A) Before LH, cGMP is maintained at high levels due to the high rate of production of cGMP by the guanylyl cyclase NPR2 expressed by mural and cumulus granulosa cells. cGMP diffuses into the oocyte through gap junctions where it acts to keep it arrested in meiosis. Mural granulosa cells of the preovulatory follicle express LHR, coupled to an adenylyl cylcase, but it is not active before LH. **(B)** When LH binds to its receptor on outer mural granulosa cells, it causes the inactivation of NPR2, partly by dephosphorylation. Inactivation of NPR2 leads to a decrease in production of cGMP, which diffuses down its gradient from the oocyte to the outside of the follicle. When cGMP levels drop in the oocyte, meiosis resumes. Modified from Shuhaibar et al., 2015.

In addition to restarting meiosis, LH causes multiple responses in the follicle: cumulus cells begin a process of expansion by depositing a hyaluronan-rich matrix, the oocyte increases its calcium stores in preparation for fertilization, and granulosa cells start the process that expels the oocyte and reprograms them to become the corpus luteum. All of these processes must happen in a highly synchronized manner to ensure that: 1) the oocyte has halved its number of chromosomes through meiotic cell division. 2) The cumulus cells that are expelled with the oocyte have expanded to allow fertilization of the oocyte. 3) Calcium stores in the oocyte are abundant and ready for release to block the fusion of multiple sperm. 4) The corpus luteum is

properly established when fertilization and implantation take place to support pregnancy. Uncovering the pathways for how LH triggers all of these events in synchrony is undoubtedly crucial for understanding female fertility and early embryonic development.

Localization of LHR and NPR2 in the follicle.

Before the study described in chapter 4 of this dissertation, there was a limited understanding of the precise localization of the LHR and NPR2 proteins due to the difficulty of generating antibodies against G protein-coupled receptors (such as LHR) and guanylyl cyclases (such as NPR2). The best studies to date localized these receptors by their mRNA expression or by autoradiography of radioactively labeled hormones that had been applied to tissue sections (Bortolussi et al., 1977; Bortolussi et al., 1979; Eppig et al., 1997; Zhang et al., 2010) (Fig. 1.5).

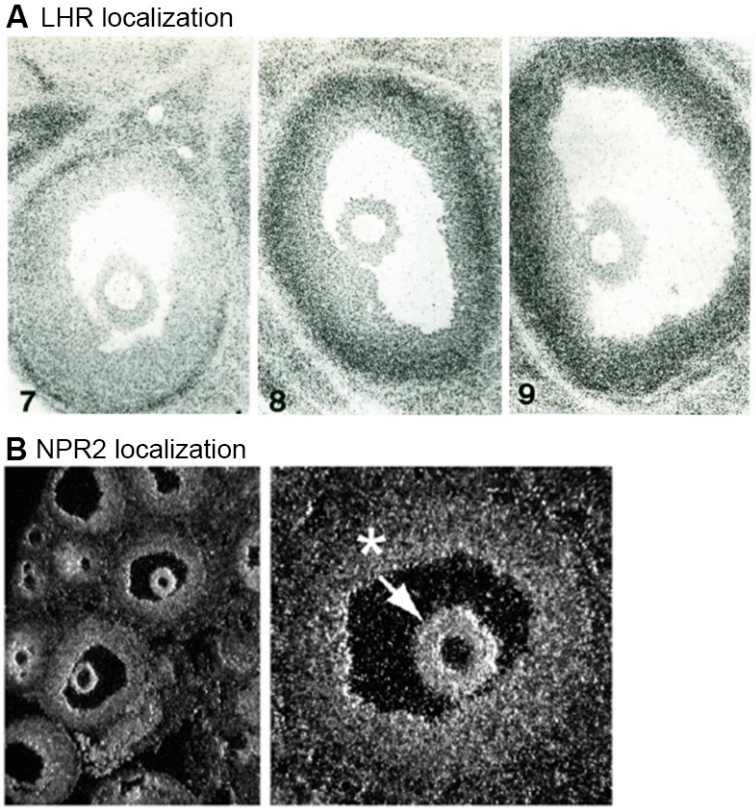

Figure 1.5. Localization studies of LHR and NPR2 before our study. (A) Binding of ^{125}I-HCG (LHR agonist) on rat ovary sections throughout the estrus cycle. Left: follicle at metestrus (before FSH rise) shows binding only in theca cells. Middle: follicle at diestrus (1 day after FSH rises) shows binding in theca and granulosa cells. Right: follicle at proestrus (right before the LH surge) shows that LH binding increases as the follicle increases in diameter and is only seen on the outer-most cells of the follicle. Adapted from Bortolussi et al., 1979. **(B)** Expression of NPR2 mRNA by granulosa cells. Highest concentration is seen in the cumulus cells and in the granulosa cells outlining the antrum. Asterisk indicates mural granulosa cells and arrow indicates cumulus cells. Adapted from Zhang et al., 2010.

Important information about factors that regulate LHR expression was also known. In-vitro studies had shown that in addition to FSH, components of the basal lamina are important stimulators of LHR mRNA expression in granulosa cells, and oocyte-secreted factors are the main inhibitor of LHR expression (Eppig et al., 1997) (Fig. 1.6). It was also known that LHR could quickly act on NPR2, but the mechanism remains incompletely understood. To better understand these cell signaling processes, this dissertation investigates the localization of LHR and NPR2 in-vivo at high single-cell resolution (Baena et al., 2020).

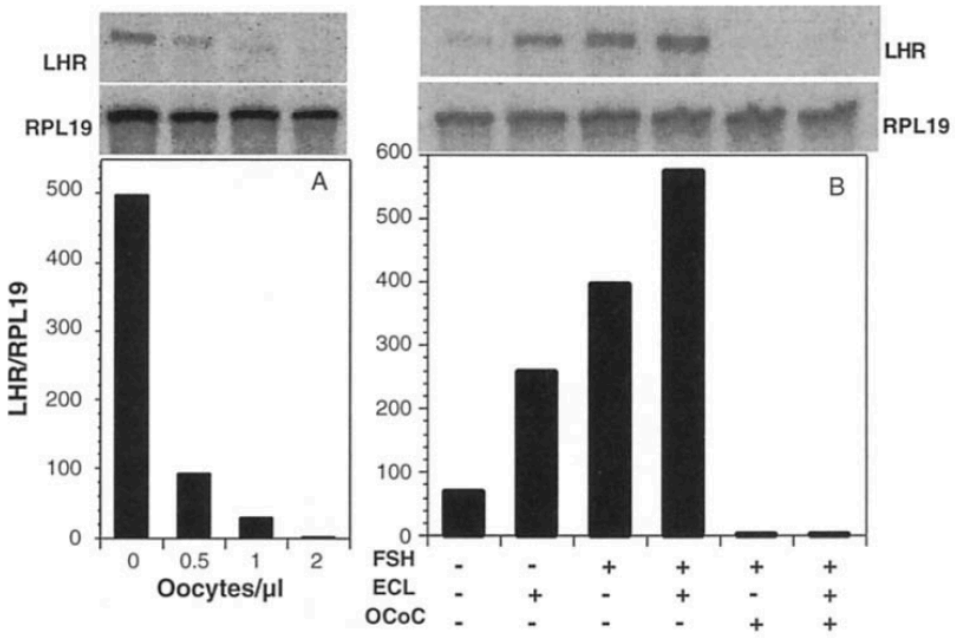

Figure 1.6. Oocytes suppress LHR expression by granulosa cells in culture. (A) Dose-dependent inhibition of LHR mRNA by granulosa cells. 2 oocytes per µl were required for complete suppression. **(B)** Effect of FSH, components of the basal lamina, and oocytes on LHR mRNA levels. The effect of basal lamina components was tested by coating the wells on which granulosa cells were grown with entactin, collagen IV, and laminin. Reproduced from Eppig et al., 1997.

IV. Three-dimensional electron microscopy as a driving method for cell biology research.

Electron microscopy can provide sub-nanometer resolution in the X and Y dimensions, and when combined with consecutive serial imaging, add nanometer-resolution in the Z dimension. This technique, known as serial section electron microscopy, offers information for biological structures with a resolution that is unmatched by light microscopy.

Historically, serial section electron microscopy was achieved by collecting sections manually; a laborious process requiring advanced knowledge in ultramicrotomy and practitioners with fine motors skills, followed by countless hours of imaging on a microscope. In recent years, however, driven mostly by the challenge of identifying the map of neuronal connections in the

brain (Denk et al., 2012), several new methods for serial section electron microscopy (or three-dimensional electron microscopy) have been developed (Titze and Genoud, 2016). These methods prioritize automation as much as possible in every step of the pipeline, pushing the limits in the number of sections that can be collected and subsequently imaged, and minimizing human errors, which are prone to arise when undertaking a repetitive task (e.g. manually imaging hundreds of serial sections).

In the Terasaki Lab, we adopted the method for serial section electron microscopy known as Automated Tape-Collecting Ultramicrotome (ATUM) (Kasthuri et al., 2015) and applied it to investigate questions in cell biology, rather than large-scale neuronal mapping (Baena et al., 2019, and chapter 2 of this dissertation). Using this technology, we are able to acquire three-dimensional volumes at varying resolutions. The highest resolution provides a view of the inside of cells to understand how intracellular components are organized, an intermediate resolution provides a view of how cells communicate with each other within a tissue, and a lower resolution allows for an analysis of how different tissues are arranged to form an organ. The unmatched power of this technique lies in that the tissue sections can be 4-5 times larger in size (up to 2 mm in length in the x and y dimensions) than what is possible with traditional electron microscopy techniques, the sections can be stored virtually indefinitely, and they can be imaged at high resolution multiple times.

The results in Chapter 3 of this dissertation were entirely acquired from this methodology, and key results in Chapter 4 were acquired by combining this method with a technique for labeling antigens by electron microscopy. Lastly, during my Ph.D. training I also participated in numerous collaborative studies that benefitted from analyses using this technique. These studies provided the following information: 1) A detailed description of Claudin-5+

immune cells in the process of extravasation through the blood brain barrier in a mouse model of neuroinflammation (Paul et al., 2016). 2) The three-dimensional characterization of the rare Tuft cell found in the intestinal epithelium by correlative light-electron microscopy (Hoover et al., 2017). 3) Morphological changes in the ER of axons in Drosophila larvae with mutations resembling those found in patients with Hereditary Spastic Paraplegia (Yalçin et al., 2017). 4) The localization of phosphorylated connexin-43 in mouse ovarian follicles using immunogold labeling in serial sections (Norris et al., 2017). 5) The description of cytoplasmic extensions that connect developing spermatogonia in mouse testes (Niedenberger et al., 2018).

The following three chapters of this dissertation consist of our studies investigating the intercellular communication in the mouse ovarian follicle. Chapter 2 describes our advances in the methodology for three-dimensional electron microscopy, which we applied to these studies. Chapter 3 provides a detailed description of TZPs and other cytoplasmic extensions that somatic cells use to communicate with each other and with the oocyte within the follicle. And in chapter 4, we show for the first time the expression of LHR and NPR2 proteins in-vivo using immunofluorescence and immunogold techniques.

Chapter 2

Serial-section electron microscopy using automated tape-collecting ultramicrotome (ATUM)

Baena, V., Schalek, R.L., Lichtman, J.W., Terasaki, M., 2019. Chapter 3 - Serial-section electron microscopy using automated tape-collecting ultramicrotome (ATUM), in: Müller-Reichert, T., Pigino, G. (Eds.), Methods in Cell Biology, Three-Dimensional Electron Microscopy. Academic Press, pp. 41–67. https://doi.org/10.1016/bs.mcb.2019.04.004

Contributions: VB did most of the writing, and all of the figures except for one.

CHAPTER

Serial-section electron microscopy using automated tape-collecting ultramicrotome (ATUM)

3

Valentina Baena[a], Richard Lee Schalek[b], Jeff William Lichtman[b], Mark Terasaki[a,*]

[a]*Deparment of Cell Biology, University of Connecticut Health Center, Farmington, CT, United States*

[b]*Department of Molecular and Cellular Biology, Center for Brain Science, Harvard University, Cambridge, MA, United States*

**Corresponding author: e-mail address: terasaki@uchc.edu*

Chapter outline

Methods in Cell Biology, Volume 152, ISSN 0091-679X, https://doi.org/10.1016/bs.mcb.2019.04.004

Abstract

The Automated Tape-Collecting Ultramicrotome (ATUM) is a tape-reeling device that is placed in a water-filled diamond knife boat to collect serial sections as they are cut by a conventional ultramicrotome. The ATUM can collect thousands of sections of many different shapes and sizes, which are subsequently imaged by a scanning electron microscope. This method has been used for large-scale connectomics projects of mouse brain, and is well suited for other smaller-scale studies of tissues, cells, and organisms. Here, we describe basic procedures for preparing a block for ATUM sectioning, handling of the ATUM, tape preparation, post-treatment of sections, and considerations for mapping, imaging, and aligning the serial sections.

1 Introduction

New ways to obtain 3-dimensional ultrastructural data are opening exciting frontiers in biology. In the ATUM (Automated Tape Collecting Ultramicrotome) method, sections are cut in a traditional way using an ultramicrotome and diamond knife with a water boat. The sections are picked up on moving tape and then imaged with a scanning electron microscope (SEM). The method was developed by Ken Hayworth, Richard Schalek (sectioning device) and Bobby Kasthuri, and Juan Carlos Tapia

(tape imaging method) in the Lichtman lab and was first used to image all the cellular constituents including every synapse, axon and dendrite in a 50-μm cube of mouse cerebral cortex (Kasthuri et al., 2015). This effort involved imaging ~2000 sections (30 nm thick) at an *xy* resolution of 3 nm per pixel (16,384 × 16,384 pixels). Much of the analysis was done using a computer-assisted manual tracing and segmentation tool (VAST, Berger, Seung, & Lichtman, 2018).

This early effort has been followed by reconstructing neuronal circuits in ~1000-fold larger volumes (cubic millimeter scale). The sectioning approach is quite fast, so the bottleneck has been image acquisition time as the volume size has increased. This limitation has stimulated significant progress on several fronts, such as the Multi-beam SEM combining 61 (or 91) single beams (Eberle et al., 2015), supercomputer alignment (Hildebrand et al., 2017; Morgan, Berger, Wetzel, & Lichtman, 2016), and automated segmentation (Ai-Awami et al., 2016; Januszewski et al., 2018).

The underlying procedures of the ATUM method are also still under development. These include fixation/processing, cutting, collecting, protein localization (Fang et al., 2018; Norris, Baena, & Terasaki, 2017), and imaging. These are all being explored extensively, and improvements can be expected.

Our goal in this chapter is to discuss aspects of the ATUM method that will first concern a new lab that is setting up the technique. Also, because these basic procedures are often sufficient for projects in cell biology, which may involve smaller volumes compared to connectomics, we do not emphasize the special challenges related to extremely large petabyte-scale volumes being contemplated in neuroscience projects.

2 Methods

2.1 Specimen preparation

Preparing a biological sample for ATUM-based imaging with a SEM involves many of the same chemicals and procedures commonly used for conventional imaging with a transmission electron microscope (TEM), with the only notable difference that more heavy-metal staining is usually needed for ATUM-based SEM imaging compared to TEM imaging. This need is related to the requirement to generate images quickly with the intrinsically slower point by point scanning approach than is required in the widefield transmission electron microscopy strategy. If the electron beam hovers over one pixel briefly, there needs to be a lot of stain (i.e., osmium) to get a recordable signal.

Like any electron microscopy method, ATUM-based projects rely on proper initial sample fixation and subsequent processing. There are many excellent articles on the subject of fixing and processing biological specimens for electron microscopy. A good introductory source is found in the textbook (Bozzola & Russell, 1999), and there are many protocols and methods available for specific tissues and animal models, most of which are well suited for ATUM-based

SEM imaging (McDonald et al., 2010; Tapia et al., 2012). Most protocols are optimized for the preservation and staining of membranes, while compromising other cellular components such as the cytoskeleton. The solutions used for the primary fixation and heavy metal staining can be adjusted to highlight other cellular components as desired but will not be discussed here.

Ideally, the sample to be examined will be processed with a protocol optimized for ATUM-based SEM imaging (Baena & Terasaki, 2019; Tapia et al., 2012), however, if the sample has already been processed for conventional TEM imaging, it can also be used for ATUM-based SEM imaging. In such case, additional heavy-metal contrast is applied to the serial sections after they have been cut, collected on tape, and the tape has been affixed to a wafer (see Section 2.8 for post-staining sections).

The resin formulation used for tissue embedding is important for ATUM sectioning since it needs to have uniform cutting properties for the hundreds or thousands of serial sections. We typically use epon resin, although other resins have been found to be appropriate. The components used to make resin can be combined in different ratios to control the hardness of the polymerized block. A block made with a hard resin formulation will make cutting ultrathin sections (30–60 nm) much easier, but the sections may be more prone to form wrinkles at the interface between the tissue and the resin. To aid in preventing this, it is recommended to keep the ratio of tissue-to-resin on the section high (discussed in more detail in Section 2.3). For cutting and collecting thick sections (200–500 nm), we recommend using a soft resin formulation to further reduce the probability of wrinkle formation.

2.2 Ultramicrotome

For the beginner, the ultramicrotome can present some exceptional challenges. In particular, the user has to understand the complex geometrical relationships between 6 degrees of freedom (*X* and *Y* axes of the knife holder, rotational angle of the knife holder, clearance angle of the knife holder, and the pitch and rotation of the block). These parameters are set by viewing the knife holder and block in three dimensions using the binocular stereomicroscope that is equipped with the ultramicrotome. Successful positioning of the knife and block requires manipulating a number of very small adjustments, which becomes less difficult with practice and training. Importantly, the tape-based approach does not in any way eliminate the need for a skilled practitioner of ultramicrotomy, thereby we recommend spending time learning the basics of ultramicrotomy and getting used to using diamond knives and an ultramicrotome. Excellent introductory material can be found in Bozzola and Russell (1999), Hagler (2007), and Maunsbach and Afzelius (1998).

Our own serial sections have been generated and collected using both RMC Powertome (Boeckeler Instruments, Inc. Tucson, AZ) and Leica UC6 ultramicrotomes (Leiva Microsystems Inc., Buffalo Grove, IL). The ultramicrotomy table and the room environment are important for the successful collection of ultrathin serial sections and are discussed below (see Section 2.6).

2.3 Trimming the block

Appropriate trimming of the block face is critical for the continuous and reliable collection of serial sections on tape. Though many of the physical and mechanical requirements of blocks used in ATUM-based serial electron microscopy are similar to blocks used in conventional electron microscopy techniques, the number of serial sections cut and collected by tape usually exceeds the number of serial sections in traditional electron microscopy by hundreds or thousands. The up-scaling in the number of serial sections requires that the tissue blocks have uniform cutting properties and that the cutting face (i.e., block face) is well trimmed on its sides and to an appropriate depth (also known as the mesa).

The block face size and shape is generally dictated by the tissue geometry and by the width of the diamond knife, which rarely exceeds 4 mm. The tape conveyor (ATUM) can collect tissue sections of any size or shape, and the sections can be picked up independently or as a ribbon. Very often, the block face shape and the smoothness of the trimmed edges will dictate the ease of cutting and collecting sections. Therefore, we highly encourage the ATUM practitioner to optimize each sample block face carefully and individually. Below, we discuss useful considerations for trimming a block for ATUM-based SEM imaging.

2.3.1 Block face size

It is generally valuable to trim the block face such that the amount of non-relevant surface is minimized. A useful rule is to trim away most, or if possible, all of the resin that does not contain the tissue being studied. Trimming away empty resin leads to a high tissue-to-resin ratio on the block face, which will make cutting and collecting sections easier than when the ratio is low. This approach reduces the possibility of wrinkles forming on the sections and also helps to extend the lifetime of the diamond knife. Creating a block face with a high tissue-to-resin ratio is not always possible to accomplish when working with very small samples as this would result in a very small block face. In these cases, small samples can be embedded with supporting tissue (such as brain or liver) around them in order to create a larger block face with a high tissue-to-resin ratio (Hildebrand et al., 2017).

The dimensions of our typical block faces vary greatly depending on the sample being studied. Generally, they tend to be no larger than 4 mm × 2 mm (length × width) or smaller than 0.5 mm × 0.5 mm. A large block face will usually provide sections that get picked-up independently from each other on the tape, making their collection easier. A disadvantage of working with a large block face is that the sections are more likely to have sectioning artifacts such as compression from passing through the knife edge and wrinkles. The smaller the block face, the less likely it is for the sections to acquire sectioning artifacts, however, if the sections are small enough, then two or more sections will collect in the space between the knife edge and the tape collector before they are picked up. It is problematic if they become separated and drift because this may cause the sections to get picked up out of order or drift past the side of the collector and not get picked up at all. If the small sections

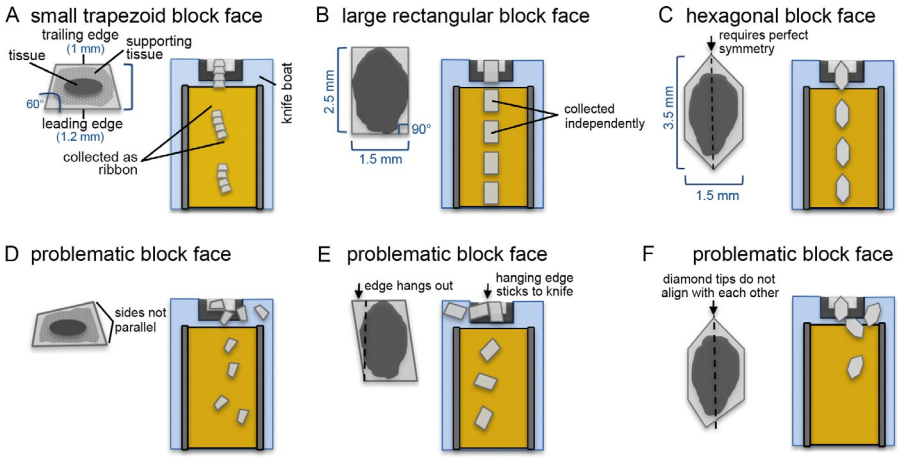

FIG. 1

Schematic of typical block face shapes and a prediction on how they are picked up by the tape. (A) A properly trimmed trapezoid block face tends to give sections that form ribbons. This shape is desirable when the block face is small. (B) A properly trimmed rectangular block face tends to give sections that are picked up independently. (C) An elongated hexagonal-shaped block face eliminates the formation of ribbons. (D) Example of an inappropriately trimmed block face. The leading and trailing edges are not parallel to each other. This leads to an abrupt rotation of the section after the trailing edge is cut, which may lead to some sections becoming stalled on the knife boat. (E) Example of an inappropriately trimmed block face. The trailing edge is longer on one side than the leading edge. The hanging edge tends to stick to the diamond knife edge, impeding the section from moving toward the tape. (F) Example of an inappropriately trimmed block face. The tips of the hexagonal-shaped block face do not align with each other, causing the sections to rotate in the knife boat.

are trimmed so that they adhere to each other to form a ribbon, the tape collector is usually able to pick them up successfully (Fig. 1A).

Fig. 1A and B illustrates the behavior of a small and a large block face shape, and consecutive section uptake by the tape. The tradeoff between section size, ease of pick-up, and tendency of artifact formation should be evaluated by the microtomist for each sample and will become more intuitive after considerable practice.

2.3.2 Block face shape

For post-imaging stitching and alignment purposes, it is useful to give the block face a shape that facilitates the collection of sequential sections that remain aligned during the cutting procedure. We recommend using a rectangular or trapezoid-shaped block face almost exclusively. A trapezoid block face consists of parallel leading (bottom) and trailing (top) edges, and side edges that form 45° to 60° angles with the leading edge, resulting in a trailing edge that is shorter than the leading edge. Trapezoid block

faces provide the most stable sections, which often remain attached to each other as ribbons (Fig. 1A). A rectangular block face has 90° angles on all corners and the trailing and leading edges are of equal length. Rectangular sections can be collected as ribbons or independently depending on the length of the side edges. Side edges of ~4 mm allow for a direct-to-tape collecting approach, in which the leading edge is picked up by the tape conveyor while the rest of the section is being cut (Fig. 1B). This creates a gap between adjacent sections, which becomes helpful during wafer mapping (see Section 2.9).

For both trapezoid and rectangular block face shapes, it is crucial to keep the leading and trailing edges parallel to each other, otherwise sections will rotate when the following section is cut, and may stall on the knife boat (Fig. 1D). Similarly, a trailing edge that does not match (or is longer than) the leading edge may cause sections to rotate due to the unmatched portion of the trailing edge becoming stuck to the diamond knife (Fig. 1E). The rotation of sections by itself is not fatal as this can be easily corrected during the wafer mapping. It only becomes a problem if the sections float away from the tape conveyor in the knife boat and become disordered or separated.

In certain cases, the microtomist will want to avoid collecting sections as ribbons because it may become difficult to determine where one section ends and another one starts on the tape, especially when the ribbons consist of sections that are small and rectangular or squared. For this, we have used an elongated hexagon-shaped block face (Hildebrand et al., 2017; Morgan et al., 2016). In this approach, the user begins with a rectangular block face (~4 mm × 2 mm), but then the trailing and leading edges are trimmed into half diamonds that are symmetrical to each other (Fig. 1C). With this block face, the trailing edge does not stick to the diamond knife edge or to the following section, thereby eliminating the formation of ribbons. This block face shape requires perfectly symmetrical trimming so that the ends of the diamond align to each other on adjacent sections (Fig. 1F).

There are many ways to collect serial sections which do not require any of the block face shapes mentioned here. In many cases, non-conventional block face shapes will be needed for particular tissue geometries. We highly encourage the microtomist to experiment with different block face shapes, and to adjust the trimming as needed for each block and for the number of sections wished to be collected.

2.3.3 Trimming tools

For block trimming, several types of tools can be used: razor blades, glass knives, and diamond trimming knives. We have extensively tested these trimming tools for the purpose of providing block faces that are useful for the cutting and collection of serial sections.

- Standard single-edged razor blades work well for an initial rough trimming of the block face. The blades are inexpensive, but practice is required to produce evenly trimmed sides and care must be taken not to cut one's fingers.
- Glass knives have a long history in the preparation of biological tissue for electron microscopy (Bozzola & Russell, 1999). Glass knives are fabricated using

a glass knife breaker, which produces 45° knives from 6.4, 8 and 10 mm thick glass (Hagler, 2007). Traditionally, glass knives are used for generating sections but they dull quickly and so are not ideal for serial sections. They can be used to trim blocks, but caution must be exercised if using both glass and diamond knives intermittently because glass shards embedded into the resin block can chip the diamond knife.

- Diamond trimming tools are used exclusively in our laboratories. Though much more expensive than the aforementioned tools, diamond knife tools provide consistently smooth and straight edges. The Trim 45 diamond knife tool (Diatome, Hatfield, PA) and the Trim 90 tool (Diatome, Hatfield, PA) (Fig. 2A) produce the best-finished surfaces (Fig. 2B). The Trim 90 tool has an additional polished facet that produces a smoother mesa sidewall surface compared to the Trim 45. A smoother mesa sidewall increases the likelihood that an ultrathin section will cut and move smoothly across the knife edge.

The trimming speed and size is important for creating a smooth mesa. For trimming the block face and sidewalls with a diamond trimming knife, we set the ultramicrotome feed size to 300–500 nm at a speed of 50–80 mm/s.

2.4 ATUM

The automated tape-collecting ultramicrotome (ATUM) is a device that facilitates the collection of hundreds to thousands of sections on tape while they are simultaneously cut with an ultramicrotome. The ATUM works by reeling tape similarly to a conveyor belt. The tape collects the sections as the cutting proceeds. The speed at

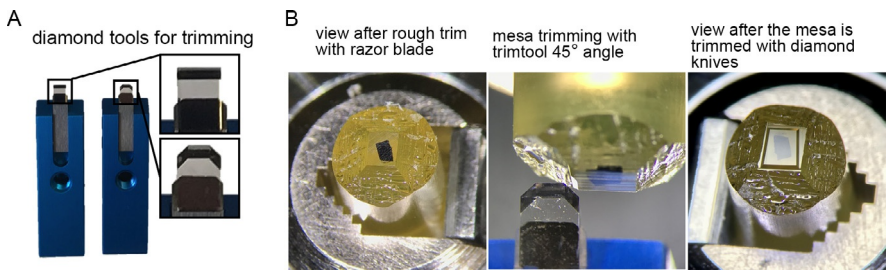

FIG. 2

Trimming a block for the ATUM. (A) Common diamond trimming knives used for shaping the block face and mesa. A single edge-razor blade is used for an initial rough trimming, then, diamond trimming knives such as Trimtool 45° (left) and Trimtool 90° (right) (Diatome-US, Hatfield, PA) are used to shape and smoothen the block face and mesa. (B) Pictures of a block face during the trimming procedure. Left: A block face after rough trimming with a razor blade. Middle: trimming of the mesa with the side of a Trimtool 45° (Diatome-US, Hatfield, PA). Right: view of a trapezoid-shaped block face and mesa after trimming with diamond knives.

which the tape moves is adjusted such that it is the same or slightly faster than the cutting speed of the ultramicrotome.

Ideally, the ATUM is set up so that as a section is cut, it pushes the previously cut section over the moving tape, which is in turn pulling some of the water with it. The section floats on the water over the tape and is pulled away from the diamond knife edge by the action of the water being pulled by the moving tape. Eventually, the water recedes and the section attaches to the tape, at which point it begins to dry on its way toward the take-up reel.

Although most of our data was acquired using a custom-built ATUM, a commercial version is available through RMC-Boeckeler (Tucson, AZ) called "ATUMtome" when combined with their PowerTome ultramicrotome. We will use the terms "ATUM" to refer to the tape-collecting device by itself, and "ATUMtome" when it is combined with the ultramicrotome.

2.4.1 ATUM parts

Fig. 3A shows some of the primary components of the RMC-Boeckeler version of the ATUM. These include a supply reel for the tape, a take-up reel, a tape tensioner and slip clutch to maintain tension, the tape snout which is placed inside the knife boat, bottom and top pinch rollers, *Z*-height control, and a syringe pump to maintain the water level in the knife, which is controlled automatically by a camera that looks at the water meniscus. In addition, the ATUM may be equipped with a Static Ionizer used to eliminate static charge which builds-up on the block face during sectioning

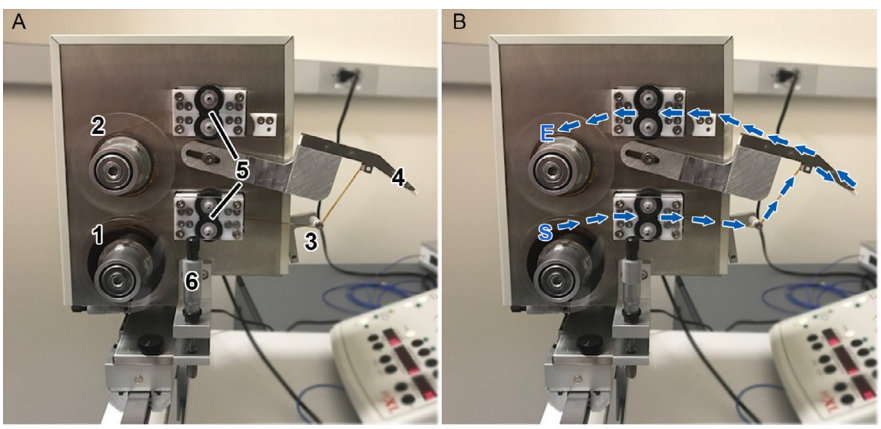

FIG. 3

Components of the ATUM and path of the tape through the ATUM. (A) Picture of the ATUM indicating its main components. (1) Supply reel for the tape, (2) a take-up reel, (3) tape tensioner, (4) snout, (5) bottom and top pinch rollers, and (6) Z-height control. (B) The path of the tape begins at the supply reel (S), goes through the bottom pinch rollers (set in the "on" position), around the tensioner arm roller, around the snout, through the top pinch rollers, and ends at the take-up reel (E) to which it is attached with adhesive tape.

(Diatome Static Line Ionizer II, Electron Microscopy Sciences, Hatfield PA). This may be placed approximately 5 cm away, facing the side of the block face (not shown). In addition to the hardware, the ATUM requires control software, which is provided by the manufacturer.

2.4.2 Setting up the ATUM: Tape feeding

The path of the tape through the ATUM starts at the supply reel, moves through the lower tape guides and lower pinch rollers, past the tensioner arm, into the diamond knife boat, over the tip of the tape snout, out of the diamond knife boat, through the upper tape guides and the upper pinch rollers, and onto the take-up reel (Fig. 3B). The tape is moved along this path by the lower and upper pinch roller motors, while tension before the lower pinch roller and after the upper pinch roller are supplied by feed and take-up reel tensioner motors attached to the slip clutches. The tension is adjusted to a certain value in the ATUM software following the manufacturer's recommendations.

Gloves should be worn when handling tape to avoid contaminating it with grease that would in turn contaminate the SEM chamber. The tape is fed to the ATUM manually by taking the end of the tape from the supply reel and feeding it to the bottom pinch rollers which are set in the "on" position in the ATUM software. As the tape moves through the bottom pinch rollers, the operator directs it around the tensioner arm roller, around the snout, through the top pinch rollers, and then it is adhered to the take-up reel with adhesive tape. After this stage, the snout can be positioned in the diamond knife water boat.

2.4.3 Setting up the ATUM: Positioning of the snout and starting a cutting run

Once the microtomist is satisfied with the shape and size of the block face, the sides of the mesa are trimmed and smooth, and the cutting face has the sample area of interest, the ATUM can be positioned for the collection of sections. Note that ultrathin (30–60 nm) cutting of serial sections (>100 sections) is performed only with diamond knives. Our serial sections are cut using either an Ultra 35° or Ultra 45° diamond knife (Diatome, Hatfield, PA) with widths up to 4 mm. Diamond knives with a larger boat (Ultra Jumbo, Diatome, Hatfield, PA), especially useful for accommodating the ATUM, are now sold commercially.

- Begin by overfilling the knife boat with water. This is advised because the water level on the knife boat is lowered when the ATUM is dipped in, causing the diamond knife edge to become dry. For a beginner, it is sometimes easier to lower the snout into an empty knife boat so that the clearance between the boat and the snout can be easily seen. The knife boat can be filled with water after the snout has been positioned.
- Place the ATUM perpendicularly to the diamond knife edge over the knife boat (Fig. 4A).
- Slowly lower the snout into the water until it is ~2 mm deep (Fig. 4B) being cautious not to touch the walls of the boat while lowering the snout.

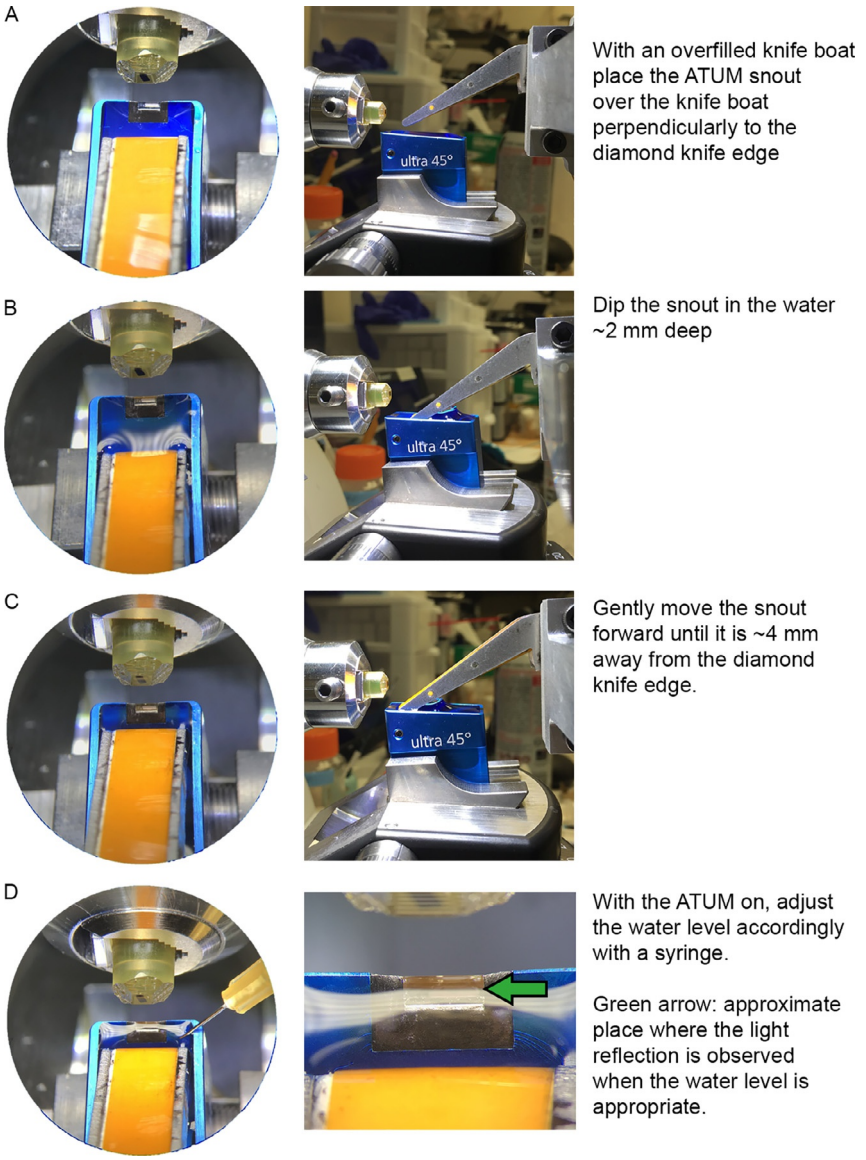

FIG. 4

Procedure to position the ATUM snout in the knife boat. (A–D) Panels on the left show view as seen from the ultramicrotome binoculars. Panels on the right show view as seen from the side (except for (D), which shows view from binoculars). Text provides summarized procedure for placing the ATUM snout in the knife boat.

- Advance the snout toward the knife edge until it is ~4 mm away from it (Fig. 4C).
  - Take caution while doing this because if the snout is placed too deep in the water boat, the metal sides of the snout may touch the front curved wall of the knife boat, which may in turn push the knife closer to the block, resulting in a thick section being cut the next time the microtome wheel is turned. The operator can look at the snout and assess its depth and proximity to the diamond knife edge by looking both from the top and from the side intermittently.
- When the snout is at the appropriate depth and distance from the diamond knife edge, turn the ATUM on using the software (the cutting speed should be set to 0.6–0.3 mm/s at this stage). The water will initially travel upwards with the tape, and then recede until it reaches an equilibrated level.
- After the water has equilibrated, adjust the level by using a 25-gage syringe to add or remove water as needed. The correct water level can be estimated by looking at the reflection of the ultramicrotome lights on the water with the ultramicrotome binoculars (Fig. 4D). The ATUM snout should sink ~2 mm deep in the water and it should not make contact with any of the knife boat walls.
- With the ATUM "on" (tape moving), cut a few sections by manually turning the ultramicrotome wheel. Adjust the water level again if needed and move the snout closer (if possible) or further from the diamond knife edge such that it is positioned at ~1.5 lengths of a section.
  - Note that a distance of 1.5 lengths of a section is only a suggestion for beginners, and may not be achievable if working with small sections. As the ATUM user becomes experienced, they may choose to adjust the snout distance differently for every block.
- After successfully cutting and collecting a few sections manually, start the automatic cutting with the ultramicrotome at a thickness of 60 nm (if the ultimate goal is to cut ultrathin sections), or 500 nm (if the ultimate goal is to cut thick sections) at a cutting speed of 0.3–0.6 mm/s. Allow enough time for the ATUMtome to cut and collect ~20 sections.
  - Try not to touch the ATUMtome or the table it rests on, disturb the sections with your breath, or make jerky movements around the area when the ATUMtome is automatically cutting. Even small vibrations can affect the cutting procedure and cause the ultramicrotome to cut thick-and-thin sections, skip cutting a section, or create chatter on the sections (see Section 2.6 for consideration on the room environment).
- While the ATUMtome is automatically cutting, pay close attention to the way the sections are collected by the tape and assess whether it is "reliable."
  A reliable cutting round should theoretically allow the operator to leave the room without worrying about whether the sections are being collected in the right order or if they are becoming lost in the knife boat. However, we encourage the beginner ATUM user to stay and observe the cutting round (usually via a camera set up on the microtome binoculars), again exercising caution as to not touch the ATUMtome or disturb the environment.
  - If the sections are rotating severely and floating away in the water boat, stop the cutting run while the ultramicrotome is in the advance position, then try to

move the ATUM snout closer to the diamond knife edge so that the tape can collect the sections before they float away. Often times, however, section rotation is caused by the way in which the block face was trimmed, especially when the leading and trailing edges are not parallel to each other. If necessary, remove the ATUM from the knife boat and re-trim the block to fix any irregularities.

- If the initial cutting and collection of sections is successful, begin to decrease the thickness of the sections in 5–10 nm intervals cutting ~5 consecutive sections on each interval until the desired thickness is achieved. Adjust the cutting speed accordingly based on the section thickness. The cutting speed we work at ranges from 0.6 to 0.1 mm/s for section thicknesses from 500 to 20 nm. The thickness and cutting speed can be adjusted while the microtome is in the advance position.
  - Note that the thinner the sections are, the more difficult the cutting run becomes. In our experience, ≥60 nm is generally easy, 50–40 nm is feasible with the right block face shape, and ≤30 nm is difficult, requiring perfect trimming of the block face and the right resin hardness (harder rather than softer resin formulation).
- The automatic water level control system equipped with the ATUMtome can be set up at this point following the manufacturers' instructions.

2.4.4 Finishing the cutting run

When enough sections have been collected, stop the automatic cutting while the ultramicrotome is in the advance mode. Raise the nose of the ATUM above the height of the knife boat and move it backwards and to the side. At this point, the tape can be reeled using the ATUM software until the last section is on the take-up reel. Cut the tape with scissors at a point between the top pinch rollers and the take-up reel.

2.5 Collection tape preparation

2.5.1 Collection tapes

A number of plastic tapes have been used to collect sections, including: Kapton HN, aluminum-coated Kapton HN, polyether ether ketone (PEEK; Sheldahl, Northfiled, MN), and carbon nanotube (CNT)-coated polyethylene terephthalate (PET) tape (Kubota et al., 2018). Kapton tape (8 mm wide) is the most commonly used and widely available tape for ATUM projects.

The physical properties of the tape affect how the sections are picked up from the knife water boat. It is very valuable to make the tape more hydrophilic by treating it with a glow discharge system prior to the collection of sections. Additionally, the tape must provide a path to ground for the imaging electrons in the microscope. Without this path, electrons accumulate in the section and repel later-arriving electrons, thereby disrupting the imaging process. Except for the aluminum-coated Kapton and the CNT tape, the user must treat the tape to make it conductive, either by sputter coating with a metal or by depositing a thin film of carbon. Below we describe the suggested treatments for Kapton tape: plasma/glow discharge system and carbon coating.

2.5.2 Plasma/glow discharge system for tape

The polymer tapes in use are intrinsically hydrophobic, and thus not very wettable. By passing the tape through a glow discharge plasma system (before collecting sections), the ionized atoms in the plasma create polar functional groups on the tape surface. This makes the surface more hydrophilic, minimizing water beading and the concomitant stresses that occur as the water trapped between the tape and section evaporates. These stresses may cause wrinkles in the sections, therefore, we suggest always treating the tape with the glow discharge system before collecting sections.

There are many commercial glow discharge systems available for treating TEM grids, but the chamber that comes with them is typically not large enough for a source and a take-up reel for the tape plus a turning mechanism. A common solution to this is to construct a larger, custom Plexiglas chamber although a commercial product designed specifically for glow discharging tape is expected to become available from Zeiss.

In the system described in Fig. 5, a chamber was designed to fit on a Pelco EasiGlow system (Ted Pella, Redding, CA). The parts listed in the Materials section were used to build the chamber and tape transport mechanism. A continuously turning motor or a stepper motor coupled by a drive belt is used to move the tape.

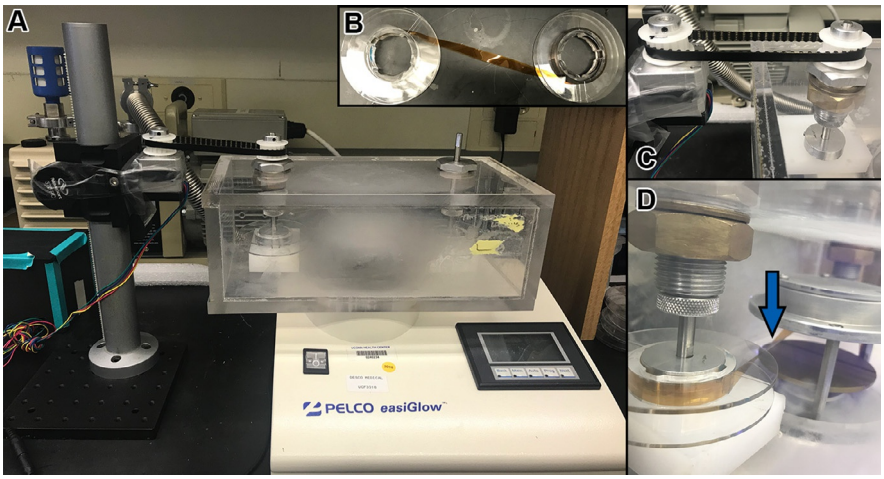

FIG. 5

Glow discharge system for tape. (A) Picture showing the PELCO easiGlow discharge unit (Ted Pella, Inc.) with a custom-made chamber. Within the chamber, the tape is passed from a source reel, through the glow discharge area, and is then collected on a take-up reel. The take-up reel is turned by a motor and a belt system (left). (B) Before placing the tape in the chamber, it is attached from the source reel to the take-up reel with adhesive tape. (C) Motor and belt system for turning reels with tape. (D) One of the reels is turned accordingly so that the tape runs parallel to the discharge plates and the underside of the tape (the side which will collect the sections) faces up as it runs in between the plates (blue arrow).

2.5.3 Carbon coating

If the user intends to image the specimen by secondary electron emission, the conductive carbon layer must be deposited on the tape before collecting the sections because a conductive layer on top of the section would interfere with the secondary electron emission. For backscatter imaging, the conductive layer can be applied before collecting sections or after the sections are collected and the tape is affixed to a wafer.

For carbon coating sections on tape affixed to a wafer, carbon evaporators commonly found in electron microscopy facilities can be used since their chambers are usually large enough for a wafer to fit in. In this approach, the wafer is placed in the carbon evaporation chamber and a film of carbon is deposited under vacuum.

2.6 Considerations for the ultramicrotomy room

Air currents from ventilation systems, windows, or fans can have a detrimental effect in the way sections are cut. Vibrations from the building, pedestrian traffic, and numerous other sources can disrupt the cutting and collection of sections, and can diminish the diamond knife lifetime. The room temperature and humidity should be controlled for consistent results.

2.6.1 Useful considerations to minimize disturbances

- Ideally, the room should be located on the lowest possible floor of the building, such as the basement.
- The room should be small and only used for the purpose of ultramicrotomy. Pedestrian traffic and opening/closing of doors should be minimal.
- Strong air vents should be covered or a plastic enclosure should be placed over the ATUMtome to shield it from air currents.
- The ATUMtome should be set on an ultramicrotomy table or an air table that is freely-floating using house air or a small compressor. The sides of the table should not touch the walls of the room.
- A room humidifier can be used to keep the humidity constant in order to achieve consistent results. The ideal relative humidity is 40–60% to avoid static electricity and the temperature stability should be about ± 1 °C per hour.

2.7 Wafer fabrication

2.7.1 Wafer specifics

The primary purpose of the wafer is to provide a flat, stable and electrically conductive surface for adhering the tape with sections, which can then be mounted on an SEM stage. Generally, silicon wafers are specified by diameter, dopant, orientation, resistivity, thickness, polish, and grade. We typically use 100 mm (diameter) silicon wafers (University Wafer, South Boston, MA). We have found that wafers with a thickness of at least 500 µm and with a single side polish (the top surface) are sufficient for most ATUM projects. Wafers with thicknesses <500 µm tend to be too fragile and are not advised. While a double sided polished wafer can be used, the

wafer cost increases by ~60% and does not provide a significant advantage. To our knowledge, both N- or P-doped wafers, with a low resistivity ranging from 0 to 100 Ω-cm can be used for ATUM-based projects.

2.7.2 Mounting tape on a wafer

The space used for wafer fabrication should be clean and as dust-free as possible. Gloves should be worn when handling tape and wafers in order to aid in maintaining a clean SEM chamber.

- Remove the take-up reel from the ATUM and place it on a reel holder (Fig. 6A) with the sections facing up. Placing the reel holder on a cutting board facilitates unreeling and cutting the tape.
- Lay down strips of double-sided carbon tape on the wafer parallel to each other (Fig. 6B, left). Some space should be allotted on the wafer surface to allow for labeling and placement of fiducials (if required for wafer mapping).
- Unreel the tape with the sections facing up and cut it with a scalpel into strips that are the same length as the double-sided carbon tape strips that were laid down on the wafer. It is helpful to use the paper/plastic cover of the double-sided tape as a reference for the length of the Kapton tape strips.
- Using two forceps, take the strips of Kapton tape with sections and lay it over the adhesive carbon tape (Fig. 6B, middle). Avoid touching the sections with the forceps. A seam roller can be used to press the Kapton tape against the adhesive tape.

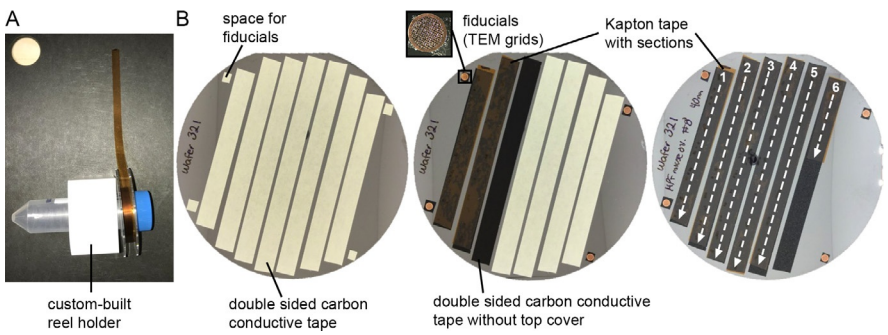

FIG. 6

Mounting tape with sections on a wafer. (A) A custom-built reel holder holing a reel with tape with sections. The tape has been spread over a cutting board so that it can be cut into strips. (B) Procedure showing how a wafer is made. Left: strips of double sided carbon conductive tape are laid down along the wafer surface. Small squares for adhering fiducials are placed where appropriate. Middle: the Kapton tape with sections is cut into strips that are then placed over the adhesive carbon tape guides. Right: The orientation and order of the strips of tape should be kept consistent throughout the wafer. In this case, the order of the sections goes from top to bottom and from left to right. The wafer will be mapped in this order.

- Continue to lay the rest of the Kapton tape strips over the carbon tape guides. Use caution to keep the order and orientation of the sections consistent throughout the wafer (e.g., the order of the sections goes from top to bottom and from left to right) (Fig. 6B, right).
- Copper tape or carbon adhesive tape can be used to provide additional grounding of the tape to the wafer.
- Label the wafer and attach fiducial TEM grids, if needed (Fig. 6B, middle). At this point, the wafer can be coated with carbon if the sample will be used for backscattered electron imaging.
- Use a dust-blowing device to clean the surface of the wafer and sections before placing the wafer in the SEM chamber. Wafers with sections can be placed in Petri dishes or compact-disc boxes and stored in airtight boxes indefinitely.

2.8 Post-staining sections on wafers

Processing biological samples for ATUM-based SEM imaging usually requires more heavy metal staining than samples processed for TEM imaging. Good heavy metal contrasting can be easily obtained by staining the tissue en-bloc as described in Section 2.1. If the contrast is still limited, additional membrane contrast can be obtained by post-staining sections on tape, in a similar way to post-staining sections on TEM grids.

After adhering the Kapton tape with sections to the wafer, we recommend placing the wafer in a high vacuum for a few minutes before starting the post-staining procedure. This will allow the Kapton tape to adhere tightly to the carbon tape, reducing the risk of trapping aqueous solutions between the two tapes during the post-staining procedure. The vacuum used for carbon evaporation or the SEM chamber vacuum work well for this purpose. Treating the wafer with affixed tape with a glow discharge system prior to the post-staining procedure will help by making the tape more wettable and allowing the reagents to spread across the sections more easily.

Typical post-staining reagents include 4% uranyl acetate (aqueous or in methanol) and stabilized lead citrate. These solutions are usually drawn into a 10 mL syringe and applied through a 0.22 µm filter directly on the sections. The solutions are washed off by submerging the wafer in double distilled water in 150 mm Petri dishes. Additional post-stain solutions may be applied to the wet sections and the washing steps are repeated.

The following post-stain solutions have provided us good results for sections on Kapton tape, but not aluminum tape. Any other post-staining protocol for TEM grids should work as well.

Uranyl acetate: 1–4% in water for 5 min.
Water washes: 3 × 3 min each with double distilled water in 150 mm Petri dishes with gentle agitation.
Lead: 0.5% stabilized lead citrate in water for 3 min.
Water washes: 3 × 3 min each with double distilled water in 150 mm Petri dishes with gentle agitation.

As with TEM grids, the water washes should be generous and the post-stain reagents should never be allowed to dry on the sections as this may cause heavy metal precipitates that will affect the quality of the images. After the final water wash, use a hair drier or dust-blowing device along the tape to blow off the water and avoid accumulations of large drops of water. The wafer is then placed in a 60 °C oven for 5–10 min or until it is completely dry. It is critical to remove all the water before placing the wafer in the SEM chamber.

2.9 Imaging and wafer mapping

Imaging is often the most problematic step in the ATUM workflow, and it seems to be particularly true for new labs. This section discusses why imaging can be challenging. Because multiple brands of microscopes can be used (i.e., Zeiss and Thermo Fisher/FEI) as well as several software programs, we will deal more with generalities than with detailed procedures.

2.9.1 Microscope parameters

One important choice is whether to use secondary electron emission or backscatter electron imaging. Acquisition by secondary electron emission can be 10 times faster, because the detector signal chain in the electron detector is faster and more efficient than backscatter detection. On the other hand, backscatter imaging produces images of larger dynamic range, which leads to higher contrast. In addition the scanned electron voltage in backscattered mode is higher (~10 kV) than in secondary mode (~2 kV) meaning the images will be sharper. The choice of detector will dictate when the carbon layer is added to the sample. As discussed in Section 2.5, secondary electron emission imaging requires the carbon layer to be deposited on the tape underneath the sections while for backscatter electron imagining, it can be deposited either underneath or on top of the sections.

2.9.2 Automated imaging

It is very possible to manually collect serial section images. A microscope operator with no time pressure and infinite patience will make perfectly centered, in-focus data. So, for any project, there is a fail-safe way to get the data! The problem is that manual collection is so time-consuming and is beset by errors as fatigue and tediousness set in. In practice, manual serial imaging is not a viable solution except for small series (<100 sections) or other unusual circumstances that require it.

Fortunately, modern SEMs have excellent automation capabilities. The microscope will reliably go to a specified location, perform an auto-focus/auto-stigmation operation, and take a picture with the specified pixel resolution and pixel number.

A typical large size for a section is 2000 µm × 2000 µm square (i.e., 2 mm × 2 mm). The sections are on a silicon wafer which is held securely on a moveable microscope stage within the SEM chamber. The sections are sometimes picked up in different orientations (see Fig. 1). Every point in every section has a unique *x*–*y* coordinate

on the microscope stage. In order to automate image collection, one must therefore determine, for each section, the points corresponding to the center of the biological structure of interest.

2.9.3 Pixel math

The user should learn "pixel math." This is somewhat akin to learning "solution math" for making solutions in the lab. This only involves arithmetic, but an error can have big consequences. It is not difficult to be off by 1000-fold or more due to the wrong use of units or by multiplying instead of dividing. In general, some basic calculations are necessary to optimize image collection; usually one is balancing the quality of the data (resolution, noise level), which necessarily slows the imaging, against the time involved in obtaining the image.

Three key quantities are the number of pixels, resolution, and field of view (FOV; which can also be called ROI = region of interest, both refer to the height and width of the area of the image). In survey mode, the microscope is typically set to obtain 1024×1024 pixel images, whereas in data collection mode, this can be $16{,}384 \times 16{,}384$ or even higher on some SEMs. At 1 nanoAmp of current, the beam resolution (spot size) is ~2–3 nm (depending on the voltage). (The SEM range of pixel resolution is between ~2 and ~2000 nm per pixel). These three quantities are related by an equation: the field of view is equal to the number of pixels multiplied by the pixel size. For instance, a low resolution image of 1024 pixels at 2000 nm per pixel has a field of view of 2048 nm = 2 mm.

A fourth key quantity is the pixel dwell time. This is how long the beam takes to scan each pixel. A typical value might be in the range of 100 ns to 1 µs per pixel. Longer dwell times result in less noisy images but correspondingly longer acquisition times. A 1024×1024 pixel image with 1 µs dwell time is obtained in 1 s. A 4096×4096 pixel image with the same dwell time will take 16 s.

As an example of how to use these quantities, one can consider how the accuracy of the stage motor can affect automated imaging. For the standard stage on a Zeiss SEM, this accuracy is ±4 µm (more accurate and correspondingly more expensive stages are available). A targeting map that is more accurate than this is superfluous. This limitation also has consequences for the field of view of automated collection. For a high-resolution image at 4 nm per pixel, this error corresponds to 1000 pixels. In other words, the field of view can be off by 1000 pixels due to stage positioning error. It would be necessary to take $\sim 10\text{k} \times 10\text{k}$ pixel images in order to reduce this error to 10% of the field of view. The large image guarantees that the center of the field of view is present in each section. A $10\text{k} \times 10\text{k}$ pixel image with 1 µs dwell time takes 100 s ($10{,}000 \times 10{,}000 \times 1$ µs), so that a high-resolution imaging run of 200 sections would take 5.5 h.

2.9.4 Software for automated image collection

A computer program is required for automated image collection. This program is installed on a second computer that can bypass the main computer to control functions of the SEM. This third party or custom in-house software keeps track

of each section and its rotation. Moreover, it allows the operator to specify the imaging conditions: pixel dimensions, nm per pixel, pixel dwell time, brightness and contrast, stigmation, scan rotation as well as adjusting parameters for auto-focus.

Several software options exist, but the Atlas 4/Atlas 5 Array Tomography (AT) software for the Zeiss SEM is the most commonly used commercially available software. The non-commercial program Wafer Mapper (Hayworth et al., 2014) was used for Kasthuri et al. (2015) and is available for download online (https://software.rc.fas.harvard.edu/lichtman/LGN/WaferMapper.html). The MATLAB® wrapper that connects to the Atlas API (application programming interface) has not yet been modified for the new Atlas 5 AT software. For FEI microscopes, we use a MATLAB®-based custom software program called SEM Navigator written by Daniel Berger of the Lichtman lab.

2.9.5 Initial mapping

One approach is to use the SEM to take a low-resolution image of the wafer. This takes ~2 h because the largest field of view of the SEM is about 2 mm × 2 mm, which is small compared to the 100 mm diameter silicon wafer. There are faster ways to take an initial image outside the microscope. One solution is to use a Zeiss Axio Imager microscope with a motorized stage to take a mosaic of images. This takes an image at a resolution of ~4 μm. Another solution is to take a picture of the wafer with a digital camera. The Terasaki lab uses the camera of an iPod touch with a custom-made photobox; the resolution of this image is ~200 μm. The photo box is a 6-in. cube made of white artist's cardboard. The bottom is open and lies on a black cardboard on the table. The wafer is placed on guidelines on the black cardboard and an iPod touch (or cell phone camera) lies on the top surface of the photobox, so that the wafer and camera are in the same relative position each time. Because the camera is directly above the wafer, the camera takes a reflected image of itself. To minimize the size of this reflection, the photobox has a small hole to accommodate just the lens of the iPod touch. The position of the photobox is adjusted so that the reflection does not lie on top of a section (Fig. 6B shows wafer images taken with this photobox). To provide uniform lighting inside the box, a single LED strip light is taped along the four walls about an inch above the bottom of the box.

The wafer image must then be aligned with the microscope stage coordinates. This is done by placing two to four special EM grids (fiducials) at corners of the wafer (see Fig. 6B). These grids have a center hole that is 10 μm in diameter. In the photograph, pixel coordinates of the centers of the grids are determined. Then, in the SEM, the microscope stage x and y coordinates of these holes are determined. The photo and SEM coordinates are matched and some math and trigonometry is done to scale and rotate the coordinate systems so that photograph coordinates of each section can be converted into microscope stage coordinates.

2.9.6 Mapping

A map (also called region of interest target map) consists of a coordinate system for each section: an origin (x and y coordinates of a specific point on the wafer) and the orientation of the x and y axes. The x–y axes of the section are perpendicular to each other, but depending on the section, are rotated at an angle relative to the x and y axes of the stage.

The Atlas 5 AT program uses one of the corners as the origin of the coordinate system for each section. The user makes a template of the first section, and then aligns this template on each section.

There are two factors that introduce error into the map. One is the significant variation from section to section in the appearance of the corner at high magnification, so that the corner location is ill defined at high resolution. Another source of error is distortions in the sections such as compression or folds, even tears. The map assumes a rigid area that is mapped by a coordinate system, and these irregularities introduce errors in locating structures within the section.

In practice, the mapping error can be as large as 50 µm or more. If the final imaging resolution is 5 nm per pixel, 50 µm corresponds to an error of 10,000 pixels, and the number of pixels imaged must be significantly larger than this to obtain any useful data by automated collection. There are three kinds of solutions to this problem: (1) user assisted automatic imaging, (2) imaging of a field of view much larger than the mapping error, and (3) a local coordinate system based on image alignment.

User assisted automated imaging: For this approach, the program moves the stage to the approximate position of the structure of interest, and the user adjusts the stage position. The coordinates are either saved for a later automated imaging run, or the user immediately acquires a data image. The second alternative can require the user to spend long stretches of time at the microscope.

Large field of view: In this approach, the automated imaging run is programmed with a field of view that is compatible with the map error. For instance, to accommodate a relatively small mapping error of 20 µm, one would want a ~200 µm field of view. If the desired resolution is 5 nm per pixel, this requires a $40{,}000 \times 40{,}000$ pixel image. The SEM cannot acquire a single image of this size but creates a tile of smaller images to cover this field of view. For instance, $16{,}000 \times 16{,}000$ pixel images can be tiled 3×3 to cover this field of view. The drawback of this approach is that acquisition of large fields of view comes at the expense of much longer imaging times.

Local coordinate system: Instead of using the corner of the section as the origin of the coordinate system, the origin is centered on a feature of interest in the specimen (Fig. 7). The origin changes if one decides to image another feature of interest on the sections. This approach was taken in Kasthuri et al. (2015) by using Wafer Mapper, a MATLAB® program written in Jeff Lichtman's lab (2014). As mentioned above, this program is not yet compatible with later versions of Atlas 5 AT software.

Another approach uses FIJI/Image J alignment algorithms in conjunction with the Atlas 4 or 5 software (Baena & Terasaki, 2019; Terasaki, 2018). The following is a

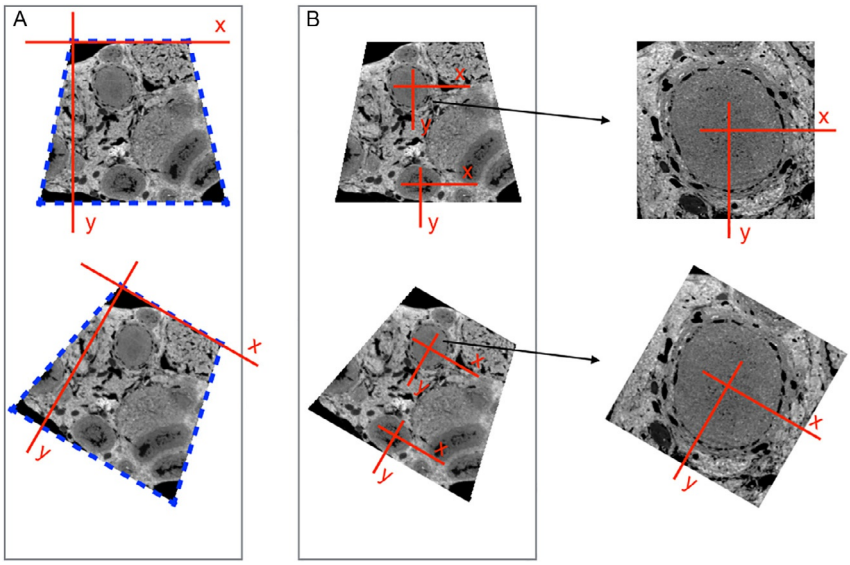

FIG. 7

Two different strategies for mapping sections. (A) With the Atlas 5 AT software, a template for the section outline is made of the first section (blue dashed lines), and this is aligned with each of the following sections. The origin of the coordinate system for each section is at one corner of the section. (B) In the alternative method, the coordinate system is defined relative to a biological structure in the specimen. An alignment algorithm operates on the image, and shifts the origin from section to section. The text explains in detail why this is advantageous. Briefly, this procedure locates the coordinate system origin with higher accuracy. In addition, a local coordinate system reduces mapping errors due to wrinkles/compression in the sections.

brief description of the workflow: The initial wafer photograph is opened in Image J, and by clicking on the approximate centers of each section, their relative locations are recorded. To translate these relative locations to microscope stage coordinates, the EM grids (Fig. 6) are used as fiducials. The center of the EM grids locations on the stage are matched with the locations in the image, and a Python script calculates the stage coordinates for an initial map. The Atlas 5 AT program stores the map information in an *xml* file, and Python scripts are used to modify them. The initial map is used for a mapping imaging run at low resolution (typically 2048 pixels, 1000 nm per pixel). The images are aligned using the FIJI plugin Register Virtual Stack Slices. This plugin produces the alignment parameters of rotation and displacement. A Python script uses these parameters to make a more accurate map. A second imaging run at intermediate resolution (2048×2048 pixels, 100–300 nm per pixel) is done and aligned in the same way. After this, the map is often accurate enough for a data imaging run, though a third mapping imaging run is not uncommon. A Python script can be used to change the center point (origin) if the user wants

to image another structure in the section. Other scripts help with the auto-focus, remove damaged sections from the queue, and reorient the wafer if it is re-imaged at another time.

Although the workflow is well-defined, it may not go smoothly for various reasons, such as problems with the alignment algorithms. The convenience of automated imaging sometimes requires solving a long series of small and occasionally not so small problems. Setting up the imaging runs with the right parameters for autofocus is crucial. The autofocus procedure starts at an initial focus value, and the success rate is significantly better if this initial value is close to the true focus level. To get closer to the true focus level, we use autofocus in all (excluding the first) mapping runs. With each mapping run, we get an approximate focus value for each section. These values are then used as the initial focus level for the final imaging run.

2.9.7 Image alignment

Post-acquisition alignment is required because the sequence of acquired images is not well aligned, if only due to the stage positioning error. Images are aligned with reasonable accuracy and speed by FIJI/Image J alignment plug-ins. With the "Linear Stack Alignment with SIFT" plug-in, the entire series of images are loaded into RAM and the aligned images are also stored in RAM. This algorithm is impractical when the size of the stack is comparable to the RAM size. The "Register Virtual Stack Slices" plug-in holds only two images at a time in RAM as it aligns, so it is less limited to RAM size. In addition, this plug-in has a "save transforms" option to save the alignment parameters of rotation and displacement for each section, which can be used in other manipulations.

The alignment may fail for several reasons. One is the lack of features to align. This can come about from a damaged section, by low image contrast, or by dust contamination. The user can try to remedy this by retaking the image, deleting a section, enhancing contrast or deleting regions of an image that cause problems, etc.

The alignment may take an inordinate amount of time. One can align reduced versions of the original images and then scale the alignment parameters to modify the original images.

The alignment may fail at a more basic level because the FIJI/Image J plug-ins are not powerful enough to align complex patterns of compression/distortion in the image. This occurs particularly with large images. Supercomputer alignment methods have been used in this case (Hildebrand et al., 2017; Morgan et al., 2016).

The most satisfying part of the ATUM workflow is to finally view a well-aligned data set. We take leave now as the investigator settles down to analyze the 3 dimensional data for biological content.

3 Instruments and materials

3.1 Ultramicrotome and ATUM (ATUMtome)

- ATUMtome (RMC Boeckeler, Tucson, AZ). Ultramicrotome and tape collector sold together.

3.2 Diamond knives and trimming tools

- Ultra diamond knife, 35° or 45° angle, 3–4 mm edge size, wet (Ultra, Diatome-US, Hatfield, PA) for cutting thin sections (≤60 nm).
- Ultra diamond knife with a large boat, 35° or 45° angle, 3–4 mm edge size (Ultra Jumbo, Diatome, Hatfield, PA) for cutting thin sections (≤60 nm).
- Histo diamond knife, 4 mm edge size (Histo, Diatome-US, Hatfield, PA) for cutting thick sections (60–1000 nm).
- Trimming diamond knife, 45° angle (Trimtool, Diatome-US, Hatfield, PA) for trimming the block face and mesa.
- Trimming diamond knife, 90° angle (Trimtool, Diatome-US, Hatfield, PA) for trimming the block face and mesa.
- Single-edged razor blades (55411-055, VWR, Radnor, PA) for rough trimming of the block face.

3.3 Tools for ultramicrotomy

- Eyelash with handle, No. 1 superfine eyelash (113, Ted Pella, Inc., Redding, CA) for manipulating sections in the knife boat and cleaning the knife edge.
- Disposable syringe with needle, 1 mL syringe with 25 G needle (14-826-88, Fisher Scientific, Hampton, NH) for finely adjusting the water level in the knife boat.
- Disposable syringe, 10 mL (14-826-88, Fisher Scientific, Hampton, NH) to add water to the knife boat.
- Syringe filter, 25 mm (05-713-401 Fisher Scientific, Hampton, NH) to be used with 10 mL syringe above for adding water to the knife boat.
- Ionizer (Static Line Ionizer, Diatome-US, Hatfield, PA) for neutralizing electrostatic charge on the block face.

3.4 Wafers, tapes, and tools for wafer fabrication

- Silicon wafers, 100 mm diameter (see other specifics on Section 2.7) (3246, University Wafer, South Boston, MA).
- Kapton tape, 8 mm wide (item number not available currently).
- Carbon conductive tape, 8 mm wide, double coated (16073, Ted Pella, Inc., Redding, CA).
- Sharp scalpel (21909-654 disposable #10 scalpel, VWR International, Radnor, PA) for cutting Kapton and double-sided carbon tape.
- Cutting board (63308, Electron Microscopy Sciences, Hatfield, PA) to use as a surface for cutting tape.
- Serrated forceps (5441, Ted Pella, Inc., Redding, CA).
- TEM grids with center mark (G150, Ted Pella, Inc., Redding, CA) used as fiducials for wafer mapping.

- Dust blower (81710, Ted Pella, Inc., Redding, CA) for removing dust from the surface of the sections.
- Plastic reels for reeling the tape (RMC Boeckeler, Tucson, AZ).
- Seam roller (62395T69, McMaster-Carr, Robbinsville, NJ) to press the Kapton tape flat against the double-sided carbon adhesive tape.

3.5 Glow discharge

- Glow discharge system, PELCO easiGlow glow discharge unit (91000, Ted Pella, Inc., Redding, CA).
- Rotary pump for glow discharge unit (92081, RVP 200-7, Ted Pella, Inc., Redding, CA). Although the Glow discharge system has a suggested pump, we found that it was not powerful enough for the custom-built chamber used for glow discharge of tape.
- Dynamic O-Ring Shaft Seal (2) (FMH-25A, ¼″ aluminum, Kurt J. Lesker Co., Jefferson Hills, PA). For rotating the tape reels.
- Plexi Glass (2) 12×6, (2) 3.5×6, (2) 3.5×11. (Chemcast GP Acrylic Sheet, 0.5″ clear, Tap Plastics, San Leandro, CA).
- Plexiglas adhesive (Weld-On 4 Cement, 4oz, Tap Plastics, San Leandro, CA).
- Plexiglas adhesive applicator (SY20-65, Syringe Hypodermic Applicator, 18 gage, Tap Plastics, San Leandro, CA).
- Motor for automatic turning (ROB-09238, Stepper motor with cable, Sparkfun, Niwot, CO).
- Stepper motor driver (ROB-12779, EasiDriver, Sparkfun, Niwot, CO).
- Arduino board for motor (DEV-11021, Arduino Uno—R3, Sparkfun, Niwot, CO).

3.6 Carbon coating

- Carbon evaporator (DV-502B High Vacuum Evaporator, Denton Vacuum, Moorestown, NJ).
- Carbon rods pointed and presharpened (70220-01, Electron Microscopy Sciences, Hatfield, PA).

3.7 Supplies for post-staining wafers

- Uranyl acetate (22400, Electron Microscopy Sciences, Hatfield, PA).
- Lead citrate (17800, Electron Microscopy Sciences, Hatfield, PA).
- Petri dishes 150 mm diameter Falcon (351058, VWR, Radnor, PA).
- Syringe disposable 10 mL (72510, Electron Microscopy Sciences, Hatfield, PA).
- Syringe filters 0.2 um (67002-25, 25 mm, Electron Microscopy Sciences, Hatfield, PA).

Acknowledgment

We would like to thank Martina Schifferer for useful suggestions on the manuscript.

References

Ai-Awami, A. K., Beyer, J., Haehn, D., Kasthuri, N., Lichtman, J. W., Pfister, H., et al. (2016). NeuroBlocks—Visual tracking of segmentation and proofreading for large connectomics projects. *IEEE Transactions on Visualization and Computer Graphics*, *22*(1), 738–746. https://doi.org/10.1109/TVCG.2015.2467441.

Baena, V., & Terasaki, M. (2019). Three-dimensional organization of transzonal projections and other cytoplasmic extensions in the mouse ovarian follicle. *Scientific Reports*, *9*(1), 1262. https://doi.org/10.1038/s41598-018-37766-2.

Berger, D. R., Seung, H. S., & Lichtman, J. W. (2018). VAST (volume annotation and segmentation tool): Efficient manual and semi-automatic labeling of large 3D image stacks. *Frontiers in Neural Circuits*, *12*, 88. https://doi.org/10.3389/fncir.2018.00088.

Bozzola, J. J., & Russell, L. D. (1999). *Electron microscopy: Principles and techniques for biologists*. Jones & Bartlett Learning.

Eberle, A. L., Mikula, S., Schalek, R., Lichtman, J., Tate, M. L. K., & Zeidler, D. (2015). High-resolution, high-throughput imaging with a multibeam scanning electron microscope. *Journal of Microscopy*, *259*(2), 114–120. https://doi.org/10.1111/jmi.12224.

Fang, T., Lu, X., Berger, D., Gmeiner, C., Cho, J., Schalek, R., et al. (2018). Nanobody immunostaining for correlated light and electron microscopy with preservation of ultrastructure. *Nature Methods*, *15*(12), 1029. https://doi.org/10.1038/s41592-018-0177-x.

Hagler, H. K. (2007). Ultramicrotomy for biological electron microscopy. *Methods in Molecular Biology (Clifton, N.J.)*, *369*, 67–96. https://doi.org/10.1007/978-1-59745-294-6_5.

Hayworth, K. J., Morgan, J. L., Schalek, R., Berger, D. R., Hildebrand, D. G. C., & Lichtman, J. W. (2014). Imaging ATUM ultrathin section libraries with WaferMapper: A multi-scale approach to EM reconstruction of neural circuits. *Frontiers in Neural Circuits*, *8*, 68. https://doi.org/10.3389/fncir.2014.00068.

Hildebrand, D. G. C., Cicconet, M., Torres, R. M., Choi, W., Quan, T. M., Moon, J., et al. (2017). Whole-brain serial-section electron microscopy in larval zebrafish. *Nature*, *545*(7654), 345–349. https://doi.org/10.1038/nature22356.

Januszewski, M., Kornfeld, J., Li, P. H., Pope, A., Blakely, T., Lindsey, L., et al. (2018). High-precision automated reconstruction of neurons with flood-filling networks. *Nature Methods*, *15*(8), 605. https://doi.org/10.1038/s41592-018-0049-4.

Kasthuri, N., Hayworth, K. J., Berger, D. R., Schalek, R. L., Conchello, J. A., Knowles-Barley, S., et al. (2015). Saturated reconstruction of a volume of neocortex. *Cell*, *162*(3), 648–661. https://doi.org/10.1016/j.cell.2015.06.054.

Kubota, Y., Sohn, J., Hatada, S., Schurr, M., Straehle, J., Gour, A., et al. (2018). A carbon nanotube tape for serial-section electron microscopy of brain ultrastructure. *Nature Communications*, *9*(1), 437. https://doi.org/10.1038/s41467-017-02768-7.

Maunsbach, A. B., & Afzelius, B. A. (1998). *Biomedical electron microscopy: Illustrated methods and interpretations*. Elsevier.

McDonald, K., Schwarz, H., Müller-Reichert, T., Webb, R., Buser, C., & Morphew, M. (2010). "Tips and tricks" for high-pressure freezing of model systems. *Methods in Cell Biology*, *96*, 671–693. https://doi.org/10.1016/S0091-679X(10)96028-7.

Morgan, J. L., Berger, D. R., Wetzel, A. W., & Lichtman, J. W. (2016). The fuzzy logic of network connectivity in mouse visual thalamus. *Cell*, *165*(1), 192–206. https://doi.org/10.1016/j.cell.2016.02.033.

Norris, R. P., Baena, V., & Terasaki, M. (2017). Localization of phosphorylated connexin 43 using serial section immunogold electron microscopy. *Journal of Cell Science*, *130*(7), 1333–1340. https://doi.org/10.1242/jcs.198408.

Tapia, J. C., Kasthuri, N., Hayworth, K. J., Schalek, R., Lichtman, J. W., Smith, S. J., et al. (2012). High-contrast en bloc staining of neuronal tissue for field emission scanning electron microscopy. *Nature Protocols*, *7*(2), 193–206. https://doi.org/10.1038/nprot.2011.439.

Terasaki, M. (2018). Axonal endoplasmic reticulum is very narrow. *Journal of Cell Science*, *131*(4), pp. 548. https, //doi.org/10.1242/jcs.210450.

Chapter 3

Three-dimensional organization of transzonal projections and other cytoplasmic extensions in the mouse ovarian follicle

Baena, V., Terasaki, M., 2019. Three-dimensional organization of transzonal projections and other cytoplasmic extensions in the mouse ovarian follicle. Scientific Reports 9, 1262. https://doi.org/10.1038/s41598-018-37766-2

Contributions: V.B. did all of the experiments, data analysis, and made all of the figures in the manuscript. The writing was split between V.B. and MT. Project was conceptualized by M.T. and V.B.

SCIENTIFIC REPORTS

OPEN

Three-dimensional organization of transzonal projections and other cytoplasmic extensions in the mouse ovarian follicle

Received: 28 August 2018
Accepted: 7 December 2018
Published online: 04 February 2019

Valentina Baena & Mark Terasaki

Each mammalian oocyte is nurtured by its own multi-cellular structure, the ovarian follicle. We used new methods for serial section electron microscopy to examine entire cumulus and mural granulosa cells and their projections in mouse antral ovarian follicles. Transzonal projections (TZPs) are thin cytoplasmic projections that connect cumulus cells to the oocyte and are crucial for normal oocyte development. We studied these projections in detail and found that most TZPs do not reach the oocyte, and that they often branch and make gap junctions with each other. Furthermore, the TZPs that connect to the oocyte are usually contacted on their shaft by oocyte microvilli. Mural granulosa cells were found to possess randomly oriented cytoplasmic projections that are strikingly similar to the free-ended TZPs. We propose that granulosa cells use cytoplasmic projections to search for the oocyte, and cumulus cell differentiation results from a contact-mediated paracrine interaction with the oocyte.

The mammalian ovarian follicle is a complex tissue structure that nurtures the growth of the oocyte and also serves as the endocrine organ which supplies the female hormones estrogen and progesterone[1]. In the large antral stage, a basal lamina encloses about 1000 granulosa cells, which form multiple layers around the oocyte. The 2–3 layers of cells adjacent to the oocyte are known as cumulus cells (or cumulus granulosa cells), while the cells in the outer layers of the follicle are known as mural granulosa cells.

The follicle begins development as a small oocyte surrounded by a single layer of thin somatic cells ("primordial follicle") and grows to full size over the course of 3–4 estrus cycles[2] (each cycle is ~4 days). Follicle development involves multiple paracrine interactions[3,4]. For instance, growth-differentiation factor-9 (GDF9) is synthesized by the oocyte and is required for the follicle to develop past the single layer stage[5].

Early follicle growth is autonomous but later, the follicle becomes responsive to follicle stimulating hormone (FSH) from the pituitary. This hormone stimulates the differentiation of cumulus cells and outer mural granulosa cells, as well as the final stages of growth. The mural granulosa cells synthesize estrogen, and the hypothalamus monitors the number of mural granulosa cells by sensing the estrogen present in the blood. When this reaches a threshold level, the hypothalamus signals to the pituitary to release a pulse of luteinizing hormone[6] (LH). LH acts on the follicle to start the ovulation process: the mural granulosa cells are reprogrammed to synthesize progesterone, the oocyte resumes meiosis, and the cumulus cells reorganize (cumulus expansion) to be expelled from the follicle along with the oocyte.

Gap junctions connect all cells in the follicle and have a critical role in follicle development and function[7]. Gap junctions transmit nutrients taken up by the granulosa cells to the oocyte[8]. Furthermore, they transmit the LH signal throughout the follicle. The LH receptors are present only on the outer mural granulosa cells[9]. LH binding causes a reduction of cGMP in these cells, which in turn lowers the cGMP levels in other granulosa cells and in the oocyte by diffusing through the gap junctions[10]. Elevated cGMP levels in the oocyte maintain it arrested in meiotic prophase, and the reduction of cGMP caused by LH reinitiates meiosis in preparation for fertilization[11]. A parallel pathway involving EGF also lowers cGMP[12].

The gap junctions between cumulus cells and the oocyte are present on remarkable structures called transzonal projections[13,14] (TZPs). These are thin cytoplasmic projections that originate from the cumulus cells and traverse the 3–5 micron-thick extracellular matrix of the oocyte (zona pellucida). They contact the oocyte surface at

Department of Cell Biology, UConn Health, Farmington, CT, USA. Correspondence and requests for materials should be addressed to M.T. (email: terasaki@uchc.edu)

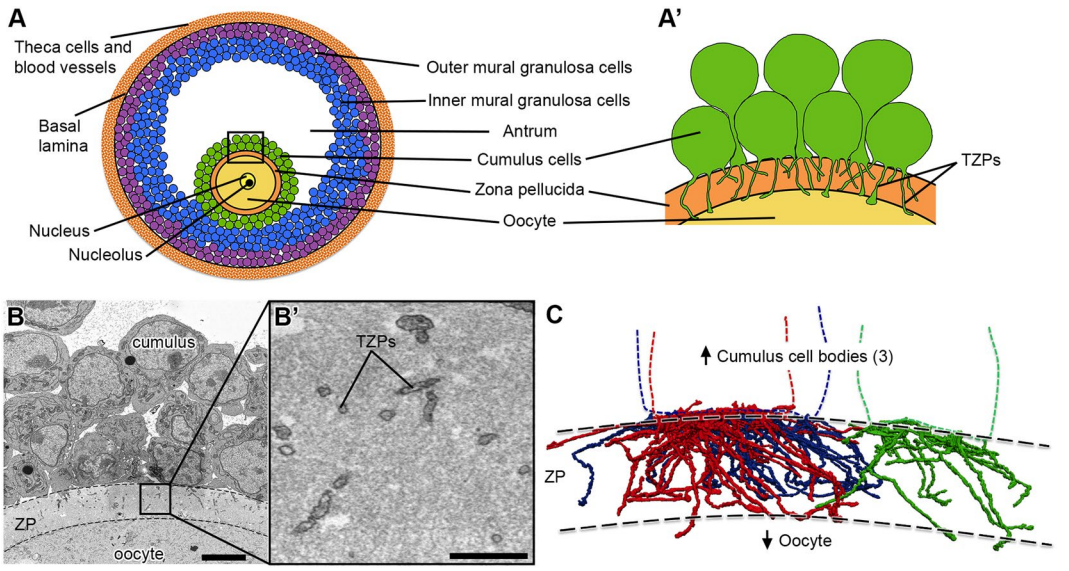

Figure 1. Cumulus cells send numerous projections through the zona pellucida. (**A**) Schematic of a mouse antral follicle. Black square represents area magnified in (A'). (A') Schematic of several cumulus cells that send transzonal projections (TZPs) through the zona pellucida to connect to the oocyte. Cumulus cell bodies can be adjacent to or displaced from the zona pellucida. **(B)** SEM image of a cross-section through cumulus cells, zona pellucida (ZP, outlined by dashed lines), and oocyte of an antral follicle. Video 1 shows 202 serial sections of this area and highlights a cumulus cell with all of its projections. Scale bar, 5 μm. (B') High-magnification of a region in the zona pellucida showing several TZPs in cross-section imaged by SEM. Scale bar, 1 μm. **(C)** Reconstruction of every TZP sent by three neighboring cumulus cells, each shown in a different color. TZPs were segmented from 405 serial electron micrographs, encompassing a volume of 22.5 × 6.7 × 18.2 μm (x, y, z). ZP, zona pellucida.

adherens junctions[15] and gap junctions[16]. Because TZPs provide the site of gap junctional communication and possibly of other interactions between the oocyte and cumulus cells, they are crucial structural elements of the follicle. However, due to their density and complexity, the three-dimensional organization of oocyte components, TZPs, and their junctions is poorly understood.

Automation and new computer capabilities have improved serial section electron microscopy so that it is much more feasible to produce large, three-dimensional fields of view at high resolution[17]. We used the ATUM (automated tape-collecting ultramicrotome) method with scanning electron microscopy[18] (SEM) to examine entire cells and their relationships to neighboring cells in mouse antral ovarian follicles. The images provide new information on follicle structure, particularly the inter-relationships of the TZPs and the oocyte cell surface. They also reveal the presence of cytoplasmic projections among granulosa cells within the follicle. As in other tissues and systems, these projections may be essential for cell communication during normal development and function[19–21].

Results

Cumulus cells extend connected and free-ended transzonal projections (TZPs). The observations to be described below were obtained from antral follicles from prepubertal mice without exogenous hormonal stimulation. At this stage, the oocyte is surrounded by a several micron-thick extracellular matrix, the zona pellucida. Cumulus cells on the other side of the zona pellucida contact the oocyte by sending cytoplasmic projections through the zona pellucida (TZPs) (Fig. 1A).

To visualize TZPs in three dimensions, we collected ~600 serial sections of 40–45 nm thickness (total depth 27 μm) and imaged volumes of ~43 × 43 μm (x, y) at a 3.5–5 nm per pixel resolution. The imaged volumes were centered to contain the zona pellucida, oocyte surface, and cumulus cell bodies (Fig. 1B). We were able to trace every TZP sent by individual cells (Video 1 and Fig. 1C), and record their interactions with other TZPs and with the oocyte surface (described below). As can be seen in video 2, TZPs arise from cumulus cells located at varying distances from the oocyte.

We found that the majority of TZPs do not reach the surface of the oocyte (Fig. 2A,C,D). On average, each cumulus cell had 31 ± 5 (n = 8) TZPs that do not reach the surface of the oocyte, and 9 ± 2 (n = 8) TZPs that reach the oocyte and make a junction with it (Fig. 2B–D) (data shown as mean ± standard error of the mean, unless specified otherwise). We will refer to these as free-ended and connected TZPs, respectively.

We measured the lengths of connected and free-ended TZPs in serial electron micrographs. The lengths of connected TZPs had a bell curve-type distribution with an average length of 7.9 ± 1.9 μm (n = 70) (mean ± standard deviation). Free-ended TZPs had a different kind of distribution, in which the number of projections decreased with length (Fig. 2E). The average length of free-ended TZPs was 2.9 ± 2.3 μm (n = 248).

Connected TZPs were significantly longer than the average thickness of the zona pellucida, which was 4.1 ± 0.3 μm (n = 3). The thickness of the zona pellucida was measured between the cumulus cell boundary and

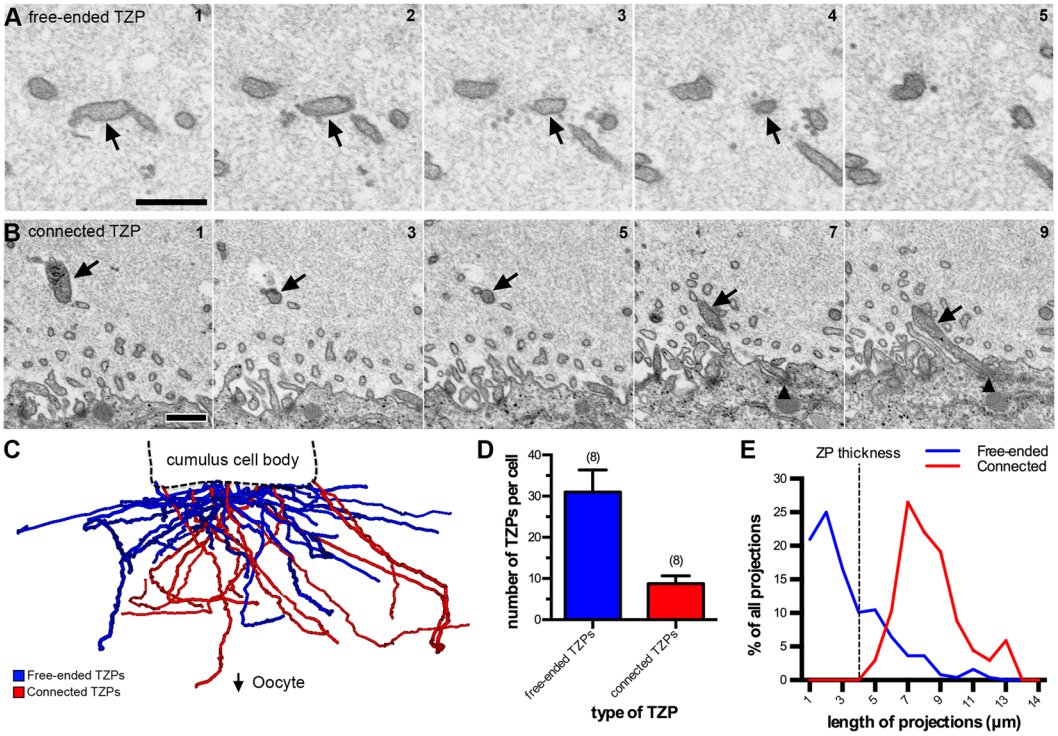

Figure 2. TZPs can be free-ended or connect to the oocyte. **(A)** Serial section SEM images of a free-ended TZP. The TZP (arrow) ends on section 4 without making contact with the oocyte or another TZP. Scale bar, 500 nm. **(B)** A series of SEM images showing every other section of a TZP that connects to the oocyte. Black triangles indicate the TZP-oocyte site of contact. Scale bar, 500 nm. **(C)** Treelines representing every TZP sent by one cumulus cell. Free-ended TZPs are shown in blue, and connected TZPs are shown in red. **(D)** Average number of TZPs per cumulus cell. TZP types were divided into free-ended (blue) and connected (red). 8 cumulus cells from 2 different follicles were analyzed. Total number of projections was 316. Average is shown as mean ± standard error of the mean. **(E)** Histogram of the length of free-ended (blue) and connected (red) TZPs from the data in D. An example of a remarkably long connected TZP can be seen in Video 3.

the oocyte surface at five locations in sections containing the widest diameter of the oocyte. Connected TZPs often extended along the surface of the oocyte making long junctions with it, thereby increasing their average length. Unexpectedly, some connected TZPs looped back to the zona pellucida after making a long junction with the oocyte surface (Video 3). Additionally, many free-ended TZPs were longer than the thickness of the zona pellucida (Fig. 2E), but these did not reach the oocyte surface because they traveled obliquely through the zona pellucida (Fig. 2C).

Connected TZPs were slightly thicker than free-ended TZPs (75 ± 2 nm (n = 28), and 68 ± 2 nm (n = 30), respectively), and organelles were more often seen in connected TZPs rather than free-ended TZPs. During our analysis, we encountered two cumulus cells in the process of mitosis in two of the follicles analyzed. One cell was in prophase and one in prometaphase. Interestingly, both mitotic cumulus cells had free-ended and connected TZPs (Supplementary Fig. 1), suggesting that cumulus cells maintain their connection with the oocyte during mitosis.

TZPs often contact each other and make gap junctions. Our data revealed novel characteristics of TZPs throughout the zona pellucida. For instance, we found that ~12% of the TZPs analyzed branched into one or more projections (Supplementary Fig. 2, and see Supplementary Fig. 3B for an additional example). Our data also revealed numerous examples of side-to-side and end-to-end contacts between TZPs (Video 4 and Supplementary Fig. 3A). Video 4 shows three examples of TZP contact sites, all found within just 21 sections (a thickness of ~1 µm), providing an example of how common these interactions are within the zona pellucida. Individual contacts like these would be difficult to resolve by light microscopy. TZP-TZP contacts were small, spanning through 1–4 40 nm sections. Most occurred in the upper half of the zona pellucida, closer to the cumulus cells than to the oocyte. We traced interacting TZPs back to their cell of origin to determine if they were derived from different cells (Supplementary Fig. 3B). From 82 TZP-TZP contacts analyzed, 78% were between TZPs from different cells and 22% were between TZPs from the same cell. The presence of same cell TZP-TZP contacts suggests that TZPs form contacts indiscriminately, in other words, two TZPs about to make a contact are not restricted whether they are derived from the same cell or from two different cells.

Gap junctions within the zona pellucida have previously been observed by immunofluorescence[22]. However, due to the limited resolution of SEM (~3 nm for these studies), it was not possible to identify small gap junctions

in our data. To investigate if the TZP-TZP contacts consisted of gap junctions, we collected sections from the same follicles that had been previously analyzed, and used transmission electron microscopy (TEM) to image the zona pellucidae. We found that most, but not all, contacts in the upper half of the zona pellucida were gap junctions (Supplementary Fig. 3C). Supporting the idea that TZPs can form gap junctions at their endings, we found that some TZPs (18 of 325) ended in an invaginated annular junction within a cumulus cell body (Supplementary Fig. 4). Based on our previous immunogold studies[23], these are likely to be invaginated gap junctions.

Connected TZPs and oocyte microvilli make contacts with each other. As described previously[13,24], TZPs end in junctions at the oocyte surface that contain adherens junctions, as identified by an electron-dense deposit[25] (Fig. 3A,B). We reconstructed 12 of these junctions and found that they range from 0.39 μm to 3.59 μm in length, and that most lie along the oocyte surface (Fig. 3C), while a few form invaginations into the oocyte cytoplasm.

Mammalian oocytes have a dense network of microvilli on their surface[26]. In our analysis, oocyte microvilli were generally uniformly distributed along the oocyte surface, and were 1.06 ± 0.09 μm ($n = 45$) long. Interestingly, we often noticed areas in the zona pellucida where microvilli appeared "clumped" (Fig. 3D). Serial section analysis revealed that these clumped areas consisted of one or two TZPs connected to the oocyte, which were closely associated with 3–6 oocyte microvilli (Fig. 3E and Video 5). Video 5 shows an example of a connected TZP that is almost continuously coupled with a long microvillus and then becomes surrounded by 5–6 short microvilli as it gets close to the oocyte surface. In some cases, microvilli were seen alongside the TZP for a distance of up to 6 μm (Fig. 3F). Although most TZPs that reached the oocyte surface were contacted by microvilli in this manner, some were not. Only one example of a microvillus contacting a free-ended TZP was seen.

To test whether TZP-microvilli contacts were gap junctions, we inspected thin sections by TEM as described in the previous section. The oocyte cytoplasm and microvilli can usually be distinguished from TZPs by a difference in electron density (see example in Video 3) or by the presence of precipitate that often forms in the oocyte cytoplasm and microvilli, but not on TZPs (see example in Video 5). This allowed us to identify possible TZP-microvilli contacts in the TEM images. In contrast to contacts seen in the upper half of zona pellucida, these did not appear to be gap junctions (data not shown).

Cytoplasmic projections are also found outside of the zona pellucida (non-TZPs). During our analysis of TZPs, we found that many cumulus cells had some projections directed away from the oocyte toward other cells, and that mural granulosa cells had similar projections. The number and directionality of the cytoplasmic projections had a striking dependence on cell location within the follicle. Projections not found in the zona pellucida will be referred to as non-TZP cytoplasmic projections.

Cumulus cells were identified as any cell that was connected to the oocyte by means of TZPs. As described before, these cells differed based on whether the cell body was located adjacent to the zona pellucida or displaced away from it (Fig. 4A,B). Cumulus cells that were directly adjacent to the zona pellucida extended most projections toward the oocyte as TZPs, and only a few away from it (Fig. 4C). These cells had an average of 51 ± 4 TZPs and 10 ± 3 non-TZP cytoplasmic projections ($n = 5$) (connected and free-ended TZPs were pooled together for these studies). Displaced cumulus cells, which were located 1–2 cell diameters away from the oocyte, had a decreased number of TZPs, and an increased number of non-TZP cytoplasmic projections. These were generally oriented toward other cells and sometimes invaginated into neighboring cell bodies (Fig. 4D and Video 1). Video 1 highlights one of these cells and every cytoplasmic projection derived from it, including TZPs. These cumulus cells had 22 ± 9 TZPs and 27 ± 3 non-TZP cytoplasmic projections ($n = 3$) (see Fig. 7A). In summary, cumulus cells that are further displaced from the oocyte have fewer TZPs and more non-TZP cytoplasmic projections compared to cumulus cells adjacent to the oocyte (see Video 2).

To analyze the projections of mural granulosa cells, we imaged volumes of ~$71 \times 71 \times 27$ μm (x, y, z) at a resolution of 5–6 nm per pixel, centered on mural granulosa cells of the follicles that were previously used to study TZPs. Cells chosen for analysis were selected if they were centrally located within the field-of-view and the cell body was completely within the volume.

Inner mural granulosa cells, which are not connected to the oocyte or to the basal lamina (Fig. 5A), had an average of 23 ± 2 projections per cell ($n = 14$). These projections were oriented in many directions with no consistent bias (Fig. 5B,C and Videos 6 and 7). Some of these projections were remarkably long (up to 13.7 μm) and frequently invaginated into neighboring cells. Video 6 shows several examples of such invaginations; in particular, one cell (colored in blue) showed 7 projections, all of which invaginated into its neighboring cell (located to its upper right). We have not detected fused membranes between the invaginated projections and the cells into which they invaginate (See video 10 for an example of an invaginated projection).

Outer mural granulosa cells were identified as those that had a visible connection with the basal lamina (Fig. 6A). Many outer mural granulosa cells had their cell body located 2–3 cell layers away from the basal lamina, but connected to it through a thick long cytoplasmic process[27] (Fig. 6B,C). Numerous thin cytoplasmic projections, similar to those found in the other cell groups, were seen originating from these elongated cells (Fig. 6C and Video 8), with an average of 28 ± 5 projections per cell ($n = 4$). Strikingly, outer mural granulosa cells that were located directly adjacent to the basal lamina (Fig. 6A,D and Video 8) had a significant reduction in the number of projections, having 7 ± 1 ($n = 3$) per cell. In summary, mural granulosa cells that are not connected to the oocyte or to the basal lamina have numerous projections that are oriented randomly, while cells that are connected to the basal lamina differ based on the location of their cell body: cells that are further displaced from the basal lamina have a larger number of projections compared to cells directly adjacent to the basal lamina (Video 9 and Fig. 7A).

We then characterized the endings of non-TZP cytoplasmic projections from cumulus, inner mural, and outer mural granulosa cells (analysis of 427 projections from 20 different cells). Most projections (38%) ended on

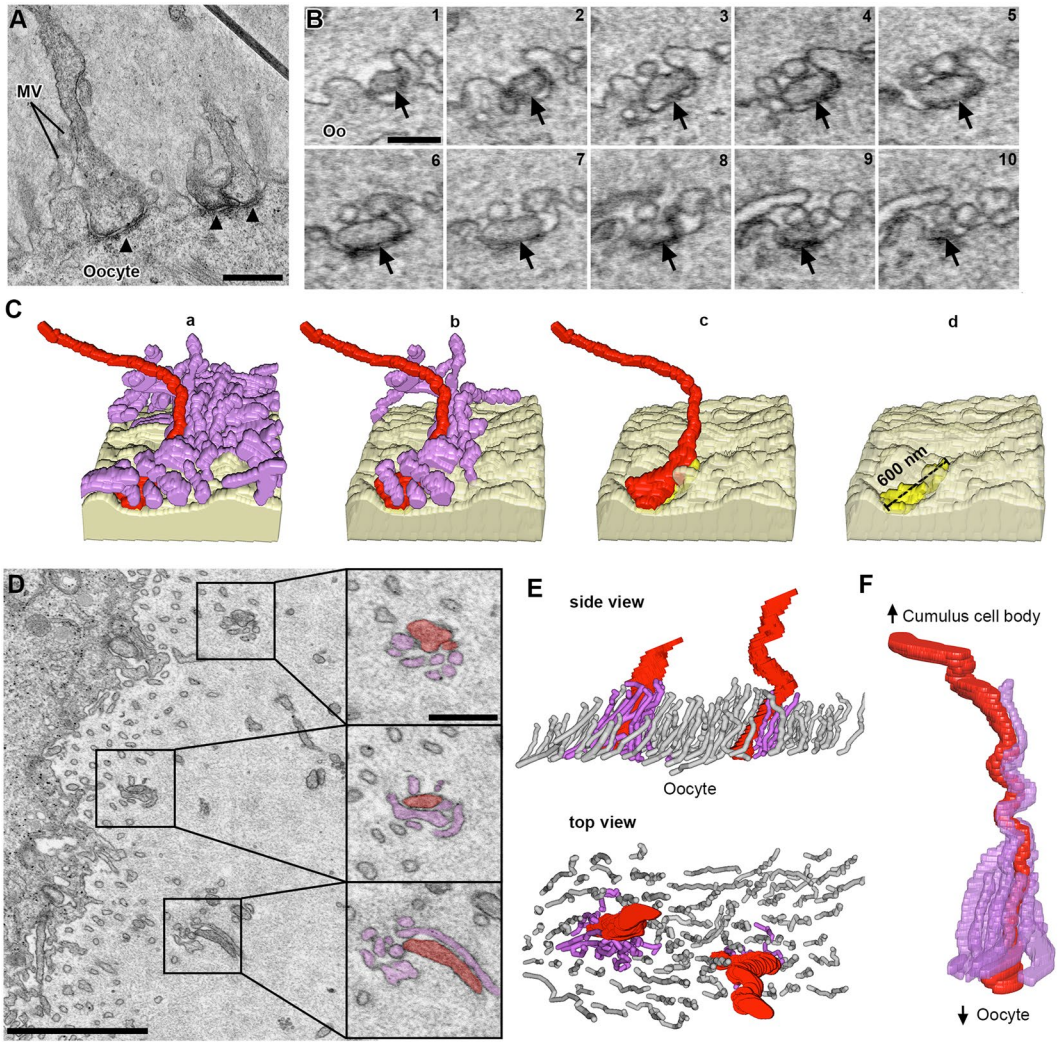

Figure 3. Contacts between TZPs and oocyte components. (**A**) TEM image of TZPs that make adherens junctions with the oocyte surface. Adherens junctions are identified by an electron-dense region at the site of TZP-oocyte contact (black triangles). Mv, oocyte microvilli. Scale bar 500 nm. **(B)** Serial section SEM images of a TZP (black arrow) that makes an adherens junction with the oocyte surface. Oo, oocyte. Scale bar, 300 nm. **(C)** Reconstruction of an adherens junction made by the TZP shown in B. Reconstruction is $2.0 \times 1.1 \times 1.7$ μm (x, y, z), spanning through 38 serial sections (each, 45 nm-thick). Light yellow: oocyte surface. Purple: oocyte microvilli. Red: TZP. Bright yellow: adherens junction. (a) TZP and all oocyte microvilli in the volume. (b) Unattached microvilli have been removed from the reconstruction to show only those that make a contact with the TZP. (c) All microvilli have been removed from the reconstruction. (d) TZP has been removed from the reconstruction to show the adherens junction on the oocyte surface. **(D)** SEM image of an area of the zona pellucida in which TZPs and microvilli appear clumped (squares). High-magnification subpanels show the TZP in red and oocyte microvilli in purple (confirmed by serial sections). Scale bars, 2 μm on low magnification, and 500 nm on high magnification subpanels. Video 5 shows this in serial sections (reconstructed in **F**). (**E**) Side and top views of a reconstruction of an area in the zona pellucida that is $3.4 \times 1.8 \times 2.8$ μm (x, y, z), spanning through 63 serial sections (each, 45 nm-thick), showing two areas where TZPs (red) are seen clumped with microvilli from the oocyte (purple). Non-interacting microvilli are shown in gray. **(F)** Reconstruction of a single TZP (red), and oocyte microvilli that tightly contact it (purple). The reconstruction is $2.9 \times 1.2 \times 2.7$ μm (x, y, z), spanning through 61 serial sections (each, 45 nm-thick). This reconstruction was segmented from the data seen in Video 5.

the surface of a neighboring cell. Other common ending types were inside an invagination in a neighboring cell (24%) (Video 10), or as a free end in the extracellular space (26%). Less common endings seen were as an end-to-end contact with a projection from a different cell (7%), as an invaginated annular junction (5%), or as a small linear gap junction (<1%). Examples of all these endings can be seen in videos 1, 6, and 8.

Common features of projections throughout the follicle. Free-ended TZPs and the cytoplasmic projections of granulosa cells showed a similar overall appearance; both were usually devoid of organelles, and their lengths were strikingly similar. As with free-ended TZPs, we found that the number of non-TZP cytoplasmic

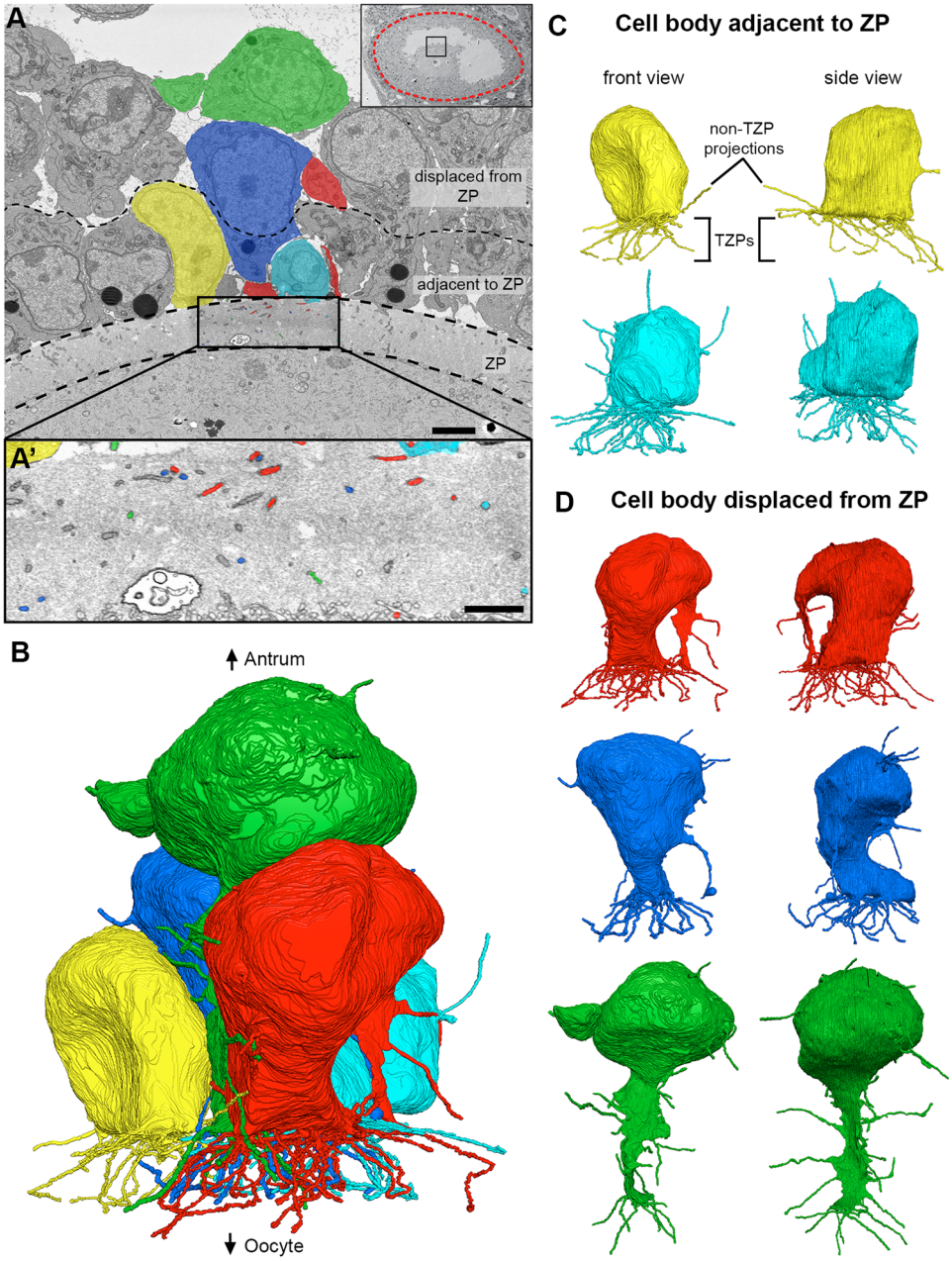

Figure 4. Directionality of cumulus cell projections. **(A)** SEM image showing multiple cumulus cell bodies, zona pellucida, and part of the oocyte in cross-section. Five cells (colored) were chosen for reconstruction. Scale bar, 5 μm. Video 1 shows 202 serial sections of this area and highlights the green cell and all of its projections. (A') High-magnification SEM image of the zona pellucida showing TZPs in cross-section. The colored TZPs originated from the cumulus cells chosen for reconstruction in A. Scale bar, 2 μm. **(B)** Reconstruction of 5 cumulus cell bodies from (**A**) and every cytoplasmic projection derived from them. Reconstruction is 28.4 × 24.6 × 18.2 μm (x, y, z), encompassing 405 serial sections (each, 45 nm-thick). A rotating view of this reconstruction can be seen in Video 2. **(C,D)** Front and side views of reconstructed cumulus cells found directly adjacent to the zona pellucida (**C**), or displaced by 1–2 cell diameters (**D**).

projections from the cumulus, inner mural, and outer mural cells decreased with length (Fig. 7B). The first, second, and third quartiles for free-ended TZPs were 1.1, 2.2, and 4.1 μm, respectively. In other words, 25% of the projections were shorter than 1.1 μm, the median (50%) was 2.2 μm, and 25% of the projections were longer than 4.1 μm. The shortest and longest lengths were 0.2 μm and 11.4 μm. For all other non-TZP projections, the first, second, and third quartiles were 1.1, 2.5, and 4.4 μm, respectively, and the shortest and longest lengths were 0.2 μm and 13.7 μm. Figure 7C shows a detailed summary of these findings separated by area within the follicle. The length distribution and thickness of these projections, which was 76 ± 2 nm (n = 67), did not change based on their location within the follicle.

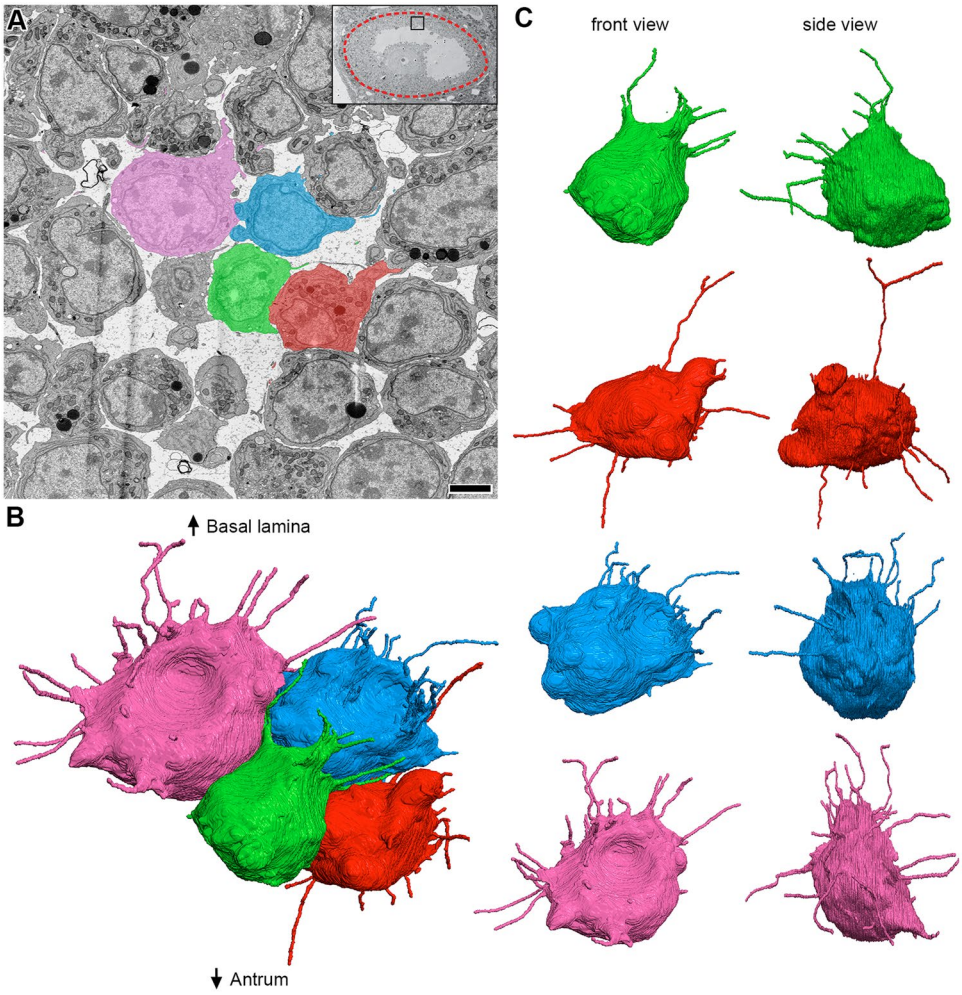

Figure 5. Inner mural granulosa cells send projections in many directions. **(A)** SEM image showing multiple inner mural granulosa cell bodies in cross-section. Four cells (colored) were chosen for reconstruction. Scale bar, 5 μm. Video 6 shows 240 serial sections of these cells and their projections. **(B)** Reconstruction of 4 inner mural granulosa cell bodies from (**A**) and every cytoplasmic projection derived from them. Reconstruction is 21.2 × 16.4 × 20.8 μm (x, y, z), encompassing 462 serial sections (each, 45 nm-thick). A rotating view of this reconstruction can be seen in video 7. **(C)** Front and side views of individual inner mural granulosa cell reconstructions from (**B**).

The striking similarity between the lengths of free-ended TZPs and non-TZP cytoplasmic projections from every cell group suggested to us that all granulosa cells are programmed to seek out the oocyte by extending cytoplasmic projections. If so, some of these projections should be longer than the thickness of the zona pellucida. Consistent with this idea, we found that at least a quarter of the projections from every somatic cell within the follicle were longer than the thickness of the zona pellucida, which was 4.1 ± 0.3 μm (n = 3) (as mentioned above) (Fig. 7B,C). Our findings suggest that every somatic cell in the follicle is able to probe a distance that is longer than the thickness of the zona pellucida around their cell body by extending cytoplasmic projections. These projections could allow cells to contact the oocyte if the cell body is located at an appropriate distance (Fig. 8).

Discussion

In this study, we examined mouse antral ovarian follicles by serial section electron microscopy. Using the ATUM method[18], we imaged volumes large enough to examine whole cells at high resolution, along with all of their cytoplasmic projections to determine how they contact other cells in the densely organized regions of the ovarian follicle.

TZP connections to the oocyte. Previous studies have shown that TZPs contact the oocyte at an adherens junction in a depression in the oocyte surface[24]. Small gap junctions have also been observed in the vicinity of the oocyte by freeze fracture and thin section TEM[28], and by immunofluorescence[22], but these studies did not provide enough three-dimensional information to determine to what degree gap junctions are present at the oocyte surface or on projections from the oocyte.

Our serial section data shows that the TZP lies in a depression in the oocyte surface without much widening (Fig. 3C), and can make long linear adherens junctions with the oocyte surface (Video 3).

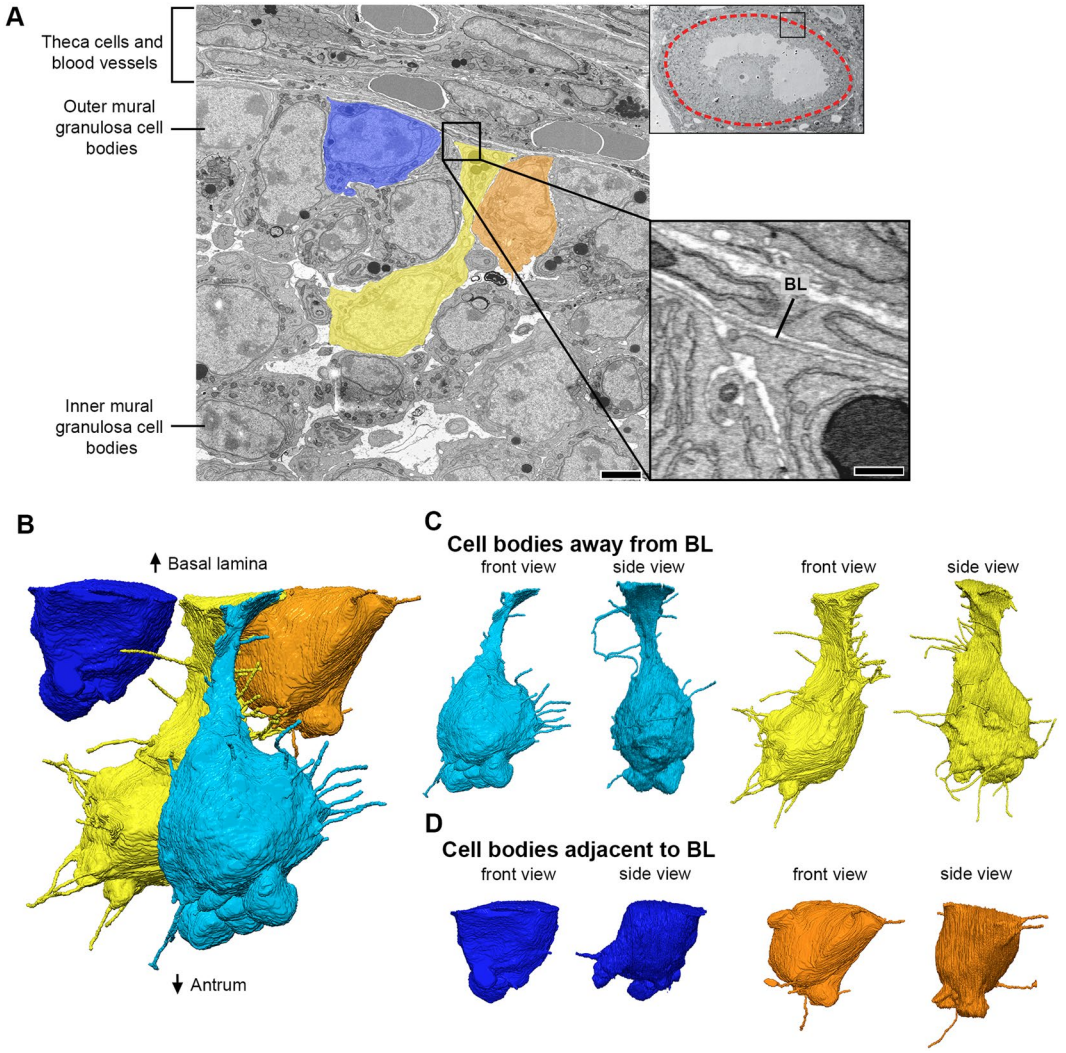

Figure 6. Outer mural granulosa cells send projections in many directions. **(A)** SEM image showing a region of inner and outer mural granulosa cells, the basal lamina, and theca cells and blood vessels found outside of the follicle. Four outer mural granulosa cells were chosen for reconstruction (three colored; one cell was not in the plane of the section). Scale bar, 5 μm. Video 8 shows 267 serial sections of this area. High-magnification insert shows parts of the cell bodies from outer mural granulosa cells on the bottom half and cell processes from theca or endothelial cells on the upper half. The basal lamina (BL) separates these cell types. Scale bar, 500 nm. **(B)** Reconstruction of 4 outer mural granulosa cell bodies and every cytoplasmic projection derived from them. Reconstruction is 16.4 × 14.7 × 22.4 μm (x, y, z), encompassing 497 serial sections (each, 45 nm-thick). A rotating view of this reconstruction can be seen in video 9. **(C,D)** Front and side views of reconstructed outer mural cells from (**B**), which were located 1–2 cell diameters away from the basal lamina (**C**) or directly adjacent to it (**D**).

We found that most TZPs that reach the oocyte surface are contacted by several oocyte microvilli on their shaft (Fig. 3D–F and Video 5). This previously undetected association is significant because there are several critical interactions between the oocyte and cumulus cells and one or more of these interactions could occur at these contact sites. We initially considered whether these were the sites of gap junctions between cumulus cells and the oocyte. We tentatively conclude that the microvilli/TZP contact sites are not gap junctions because we did not find them in this region of the zona pellucida by TEM. An interaction that may be occurring at the microvilli/TZP contact sites is discussed below.

Free-ended TZPs and dynamics. Although TZPs have been known for many years, their dynamics have not yet been characterized. A recent study has focused on this issue using a reconstituted system[29]. When cumulus cells that have been stripped from their innate oocyte are reaggregated with a donor oocyte, they make new TZPs, which form junctions with the oocyte. This clearly demonstrates that TZPs are dynamic structures.

Our serial section data is consistent with dynamic TZPs *in-situ*. We show for the first time that most TZPs in the zona pellucida are free-ended (Fig. 2). Free-ended TZPs have a wide distribution of lengths and are oriented in many directions. We found that TZPs often make close contacts with each other, some of which were found

Region within follicle	Projection type	Number of projections per cell	Number of projections counted
Outer mural adjacent to BL	Non-TZPs	7 ± 1	20
Outer mural displaced from BL	Non-TZPs	28 ± 5	111
Inner mural	Non-TZPs	23 ± 2	320
Cumulus displaced from ZP	Non-TZPs	27 ± 3	82
	Free-ended TZPs	16 ± 7	49
	Connected TZPs	5 ± 2	16
Cumulus adjacent to ZP	Non-TZPs	10 ± 3	51
	Free-ended TZPs	40 ± 4	199
	Connected TZPs	11 ± 2	54

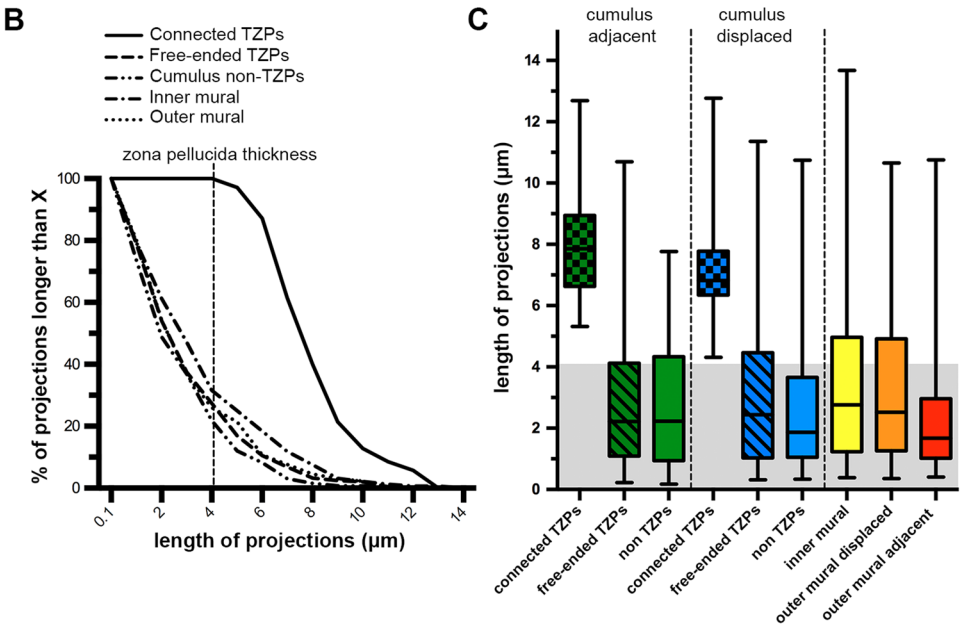

Figure 7. Summary of cytoplasmic projections in somatic cells of antral ovarian follicles. (**A**) Summary table describing the number of projections per cell in each region of the ovarian follicle. Outer mural adjacent to BL refers to cells found directly adjacent to the basal lamina (n = 3). Outer mural displaced from BL refers to cells found two-to-three cell diameters away from the basal lamina but that still connect to it through a thick cytoplasmic process (n = 4). Inner mural refers to cells not connected to the oocyte or to the basal lamina (n = 14). Cumulus displaced from ZP refers to cells found two-to-three cell diameters away from the zona pellucida but that still connect to the oocyte through TZPs (n = 3). Cumulus adjacent to ZP refers to cells found directly adjacent to the zona pellucida (n = 5). Numbers are shown as mean ± standard error of the mean. To the left of the table are representative reconstructions of one cell from each of the cell groups in the table. Follicle insert is colored to represent the different cell groups. **(B)** Distribution of the length of projections from each group. All cumulus cells, regardless of the position of their cell body, were pooled together for the groups free-ended TZPs, connected TZPs, and cumulus non-TZPs. Outer mural granulosa cells were also pooled together. **(C)** Length of projections from every cell group represented as quartiles. Lower and upper edges of the box

represent the first and third quartiles, respectively (25th and 75th percentiles). The line in the middle of the box represents the median (50th percentile). The lower and upper limits of the "whiskers" represent the minimum and maximum values, respectively. Cell groups are divided as described in (**A**). Gray-shaded region represents the thickness of the zona pellucida (~4.1 μm). Note that ~25% of all of the projections from each cell type are longer than the width of the zona pellucida (suggesting they could contact the oocyte if the cell body is at an appropriate distance).

to be gap junctions by TEM (Supplementary Fig. 3 and Video 4). Our observations are consistent with persistent growth and perhaps retraction of TZPs in intact follicles at a stage when the cumulus cells are already connected to the oocyte by TZPs. All TZPs contain actin but only a small minority contain microtubules[29]. We suggest that the free-ended TZPs contain only actin and that microtubules grow into them if they connect to the oocyte.

One question is whether the TZP dynamics is induced or constitutive. In their recent study, El-Hayek *et al.*[29] present evidence that oocyte-derived factors induce the formation of TZPs. When the oocyte is removed from a granulosa-oocyte complex (GOC), the mRNA levels for general components of filopodia (*Damm1*, *Fscn1*, and *Myo10*) are drastically reduced in the remaining granulosa cells. Additionally, when soluble GDF9 (a BMP-like family paracrine factor produced by the oocyte) was added to the GOCs medium, the mRNA levels of filopodia components were restored (there is uncertainty however regarding the physiological dose for GDF9). When GDF9 production was blocked by siRNA injection into oocytes of intact GOCs, filopodia mRNA levels were reduced in granulosa cells and the number of TZPs counted was 30% lower than their controls. The authors conclude that GDF9, possibly with other oocyte-secreted factors, induces cumulus cells to extend filopodia into the zona pellucia towards the oocyte. We present an idea below that the dynamics of TZPs is largely constitutive.

Cytoplasmic projections/filopodia in the follicle. Our serial section data allowed us for the first time to detect and characterize cytoplasmic projections in parts of the follicle that are densely populated with cells. We found that cumulus cells have some projections directed away from the oocyte (Fig. 4 and Video 2), and that mural granulosa cells have numerous projections extending in all directions (Figs. 5 and 6, and Videos 6 and 9). There is a striking similarity in the length distributions of these projections and the free-ended TZPs (Fig. 7). We did not show that these projections contain filopodia markers, but on the basis of their similarity to TZPs, which do have filopodial markers[29], it seems likely that these projections are filopodia.

Possible filopodial functions. Filopodia are frequently seen in cultured cells and are often dynamic when observed by time-lapse imaging. They have also been commonly observed *in-situ* such as in the sea urchin and Xenopus embryo blastocoel[30,31]. There is evidence that filopodia sense environmental cues that guide migration of pathfinding neurons and of vascular endothelial tip cells forming a new capillary[32,33]. Upon contact with axons, dendritic filopodia were observed to become dendritic spine synapses[34].

In the ovarian follicle, filopodia could be involved in transducing paracrine or hormonal signals. These signaling molecules are usually thought to act by diffusion but there is recent evidence that paracrine factors can act by contact with specialized filopodia termed "cytonemes"[35]. Evidence for signaling by contact has been found in tissues where paracrine signaling is known to occur[19]. Receptors and ligands have been localized to filopodia[36,37], and paracrine signaling is reduced or eliminated by eliminating the filopodia[38].

There is evidence for paracrine signaling by contact in the Drosophila male germline stem cell niche. In this system, Decapentaplegic (Dpp), a Drosophila BMP, is secreted by hub cells to maintain adjacent cells as germline stem cells[39]. When a germline stem cell divides, the daughter cell, which becomes displaced away from the hub cell (source of Dpp) begins to differentiate. Later work showed that the germline stem cells extend microtubule-based projections (MT-nanotubes), which invaginate into hub cells. Dpp and its receptor Thickveins (Tkv) were localized to these invaginated compartments[20]. Thus, the Dpp/Tkv interaction occurs where two cells make a close contact.

We attempt here to provide an explanation for our observations of filopodia in granulosa cells and the TZPs in cumulus cells. In the follicle, it is thought that the inner mural granulosa cell is the default state and that GDF9 induces the cumulus cell-specific phenotype. Cultured granulosa cells from dissociated follicles are induced to synthesize cumulus cell markers by addition of soluble GDF9[40] and a partial knockdown of GDF9 causes diminished expression of cumulus cell markers[41].

It is assumed that GDF9 diffuses from the oocyte across the zona pellucida and induces adjacent cells to become cumulus cells. We propose instead that the GDF9 interactions occur when a filopodia contacts the oocyte. In this idea, granulosa cells use filopodia to search whether they are close to the oocyte. If they contact the oocyte, they become a cumulus cell, and the contacting filopodia convert into a connected TZP. Conversely, if a granulosa cell is in contact with the basal lamina, it becomes an outer mural granulosa cell (Fig. 8).

Our proposal accounts for the presence of filopodia throughout the follicle as well as their similar length distributions, in which ~25% are long enough to traverse the zona pellucida (Fig. 7C). The main prediction is that receptors for GDF9 are present on the filopodia. In particular, these receptors should be present at sites of contact of oocyte and TZPs, for instance, at the microvilli/TZP contact sites. Receptors for GDF9 have been localized but at a resolution too low to address this issue[42]. New methods for immunolabeling serial sections may help to test this idea[23].

In summary, new methods for serial section electron microscopy enabled us to examine whole cells and their relationship to other cells with ultrastructural resolution. Our study shows that this kind of structural information may be useful in understanding the interactions that occur during development and function of a complex tissue structure. Knowledge of other tissue structures is likely to benefit from similar serial section analysis.

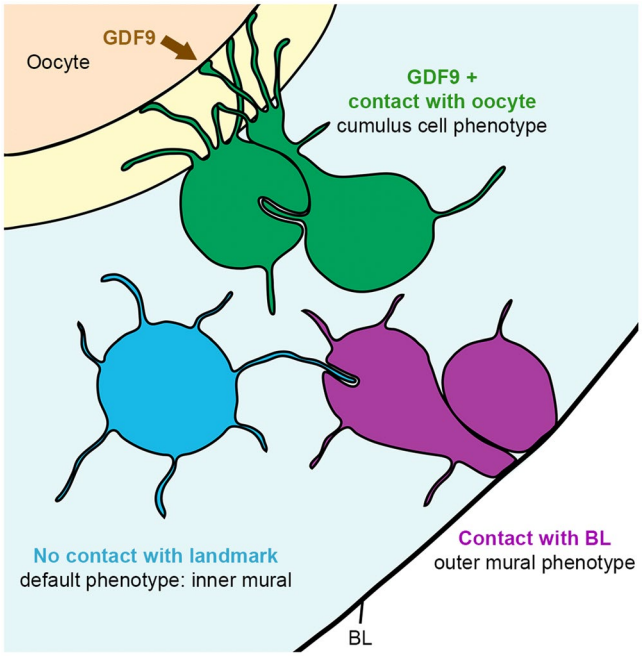

Figure 8. Proposed model. Differentiation of somatic cells in the ovarian follicle is dependent on contact with the oocyte or with the basal lamina. Here, a granulosa cell becomes a cumulus cell (green) if it contacts the oocyte through TZPs and receives the GDF9 signal from the oocyte. If a granulosa cell makes contact with the basal lamina, it becomes an outer mural granulosa cell (purple). Conversely, if a granulosa cell does not make contact with the oocyte or with the basal lamina, it remains as an inner mural granulosa cell (blue), the default phenotype.

Materials and Methods

Animals. Ovaries were obtained from prepubertal 24-day-old C57BL/6J mice (Jackson Laboratories, Bar Harbor, ME). The mice were not injected with hormones prior to euthanasia. All procedures were approved by the animal care committee at UConn Health. All methods and procedures were performed in accordance with the relevant guidelines and regulations.

Tissue processing for electron microscopy. After dissection from the animal, ovaries were cleaned and split into 3–4 pieces with forceps. Special attention was used to attempt to preserve follicle integrity. The pieces were rinsed in 1X PBS once, and then fixed in a Karnovsky's fixative (2.5% glutaraldehyde/2% paraformaldehyde) in 0.1 M cacodylate buffer for 3–4 hours at room temperature. Ovaries were then rinsed several times in 0.1 M cacodylate buffer and stored overnight at 4 °C.

Ovaries were post-fixed with 4% OsO_4 in 3.2% potassium ferricyanide in 0.1 M cacodylate buffer for 1 hour at room temperature. They were then thoroughly rinsed with distilled water, treated with 1% aqueous uranyl acetate overnight at 4 °C, and then treated with 0.066% lead aspartate for 30 minutes at 60 °C. The samples were then rinsed thoroughly with distilled water, dehydrated in graded ethanol solutions, embedded in epoxy resin (Poly/bed 812 Embedding Media, Polysciences, Warrington, PA), and polymerized in a 60 °C oven for 48 hours.

Sectioning, imaging, and analysis. Serial sections were cut from the polymerized epon blocks with a diamond knife (Ultra 45°, Diatome, Hatfield, PA) at a thickness of 40–45 nm. For each sample, 400–600 serial sections were collected on tape using an automated tape-collecting ultramicrotome[18]. The tape with sections was laid on silicon wafers (University Wafer, Boston, MA), and then coated with carbon.

The sections were mapped and imaged as described previously[43] using a field-emission scanning electron microscope (Zeiss Sigma FE-SEM) in backscatter mode (8 keV), at a resolution of 3.5–6 nm/pixel (12,000 × 12,000 pixels), and the Atlas-4 Imaging software (Fibics, Ottawa, Ontario, Canada) in conjunction with custom scripts. Some sections were additionally imaged with a Verios 460 L field-emission scanning electron microscope (FEI, Raleigh, NC). These were taken by the backscatter detector (5 keV) using immersion mode, at a resolution of 3–10 nm/pixel.

For TEM imaging, blocks that had already been cut for SEM serial sections were re-trimmed into a ~1 mm × 1 mm face, and 4–6 60 nm serial sections were collected as ribbons on formvar-coated slot grids. Sections were additionally post-stained with 3% aqueous uranyl acetate for 5 minutes, and dried at room temperature. Grids were imaged with a Hitachi H-7650 transmission electron microscope (Hitachi, Tarrytown, NY).

FIJI Image J was used for the image analysis. The alignment was done using the Linear Stack Alignment with SIFT plugin. The segmentations were done in the TrackEM2 module[44] using area lists, and the measurements

of cytoplasmic projections were done in the same module using treelines. The reconstructions were rendered in Adobe Photoshop CS6-Extended (Adobe, San Jose, CA).

Data Availability

All the data analyzed in this manuscript is available upon request to the authors.

References

1. Hawkins, S. M. & Matzuk, M. M. Menstrual cycle: basic biology. *Ann N Y Acad Sci* **1135**, 10–18 (2008).
2. Hirshfield, A. N. Development of follicles in the mammalian ovary. *Int. Rev. Cytol.* **124**, 43–101 (1991).
3. Edson, M. A., Nagaraja, A. K. & Matzuk, M. M. The mammalian ovary from genesis to revelation. *Endocr. Rev.* **30**, 624–712 (2009).
4. Richards, J. S. & Pangas, S. A. The ovary: basic biology and clinical implications. *J. Clin. Invest.* **120**, 963–972 (2010).
5. Dong, J. *et al*. Growth differentiation factor-9 is required during early ovarian folliculogenesis. *Nature* **383**, 531–535 (1996).
6. Knobil, E. On the control of gonadotropin secretion in the rhesus monkey. *Recent Prog. Horm. Res.* **30**, 1–46 (1974).
7. Simon, A. M., Goodenough, D. A., Li, E. & Paul, D. L. Female infertility in mice lacking connexin 37. *Nature; London* **385**, 525–9 (1997).
8. Sugiura, K., Pendola, F. L. & Eppig, J. J. Oocyte control of metabolic cooperativity between oocytes and companion granulosa cells: energy metabolism. *Dev. Biol.* **279**, 20–30 (2005).
9. Bortolussi, M., Marini, G. & Reolon, M. L. A histochemical study of the binding of 125I-HCG to the rat ovary throughout the estrous cycle. *Cell Tissue Res.* **197**, 213–226 (1979).
10. Shuhaibar, L. C. *et al*. Intercellular signaling via cyclic GMP diffusion through gap junctions restarts meiosis in mouse ovarian follicles. *Proc Natl Acad Sci USA* **112**, 5527–5532 (2015).
11. Norris, R. P. *et al*. Cyclic GMP from the surrounding somatic cells regulates cyclic AMP and meiosis in the mouse oocyte. *Development* **136**, 1869–1878 (2009).
12. Liu, X., Xie, F., Zamah, A. M., Cao, B. & Conti, M. Multiple pathways mediate luteinizing hormone regulation of cGMP signaling in the mouse ovarian follicle. *Biol. Reprod.* **91**, 9 (2014).
13. Li, R. & Albertini, D. F. The road to maturation: somatic cell interaction and self-organization of the mammalian oocyte. *Nature Reviews. Molecular Cell Biology; London* **14**, 141–52 (2013).
14. Clarke, H. J. Regulation of germ cell development by intercellular signaling in the mammalian ovarian follicle. *WIREs Dev Biol* **7** (2018).
15. Mora, J. M. *et al*. Characterization and significance of adhesion and junction-related proteins in mouse ovarian follicles. *Biol Reprod* **86** (2012).
16. Gilula, N. B., Epstein, M. L. & Beers, W. H. Cell-to-cell communication and ovulation. A study of the cumulus-oocyte complex. *The Journal of Cell Biology* **78**, 58–75 (1978).
17. Denk, W. & Horstmann, H. Serial block-face scanning electron microscopy to reconstruct three-dimensional tissue nanostructure. *PLoS Biol* **2** (2004).
18. Kasthuri, N. *et al*. Saturated reconstruction of a volume of neocortex. *Cell* **162**, 648–661 (2015).
19. Ramírez-Weber, F. A. & Kornberg, T. B. Cytonemes: cellular processes that project to the principal signaling center in Drosophila imaginal discs. *Cell* **97**, 599–607 (1999).
20. Inaba, M., Buszczak, M. & Yamashita, Y. M. Nanotubes mediate niche-stem cell signaling in the Drosophila testis. *Nature* **523**, 329–332 (2015).
21. Heimsath, E. G., Yim, Y.-I., Mustapha, M., Hammer, J. A. & Cheney, R. E. Myosin-X knockout is semi-lethal and demonstrates that myosin-X functions in neural tube closure, pigmentation, hyaloid vasculature regression, and filopodia formation. *Sci Rep* **7** (2017).
22. Simon, A. M., Chen, H. & Jackson, C. L. Cx37 and Cx43 localize to zona pellucida in mouse ovarian follicles. *Cell Communication & Adhesion* **13**, 61–77 (2006).
23. Norris, R. P., Baena, V. & Terasaki, M. Localization of phosphorylated connexin 43 using serial section immunogold electron microscopy. *J. Cell. Sci.* **130**, 1333–1340 (2017).
24. Motta, P. M., Makabe, S., Naguro, T. & Correr, S. Oocyte follicle cells association during development of human ovarian follicle. a study by high resolution scanning and transmission electron microscopy. *Archives of Histology and Cytology* **57**, 369–394 (1994).
25. Niessen, C. M. & Gottardi, C. J. Molecular components of the adherens junction. *Biochimica et Biophysica Acta (BBA) - Biomembranes* **1778**, 562–571 (2008).
26. Runge, K. E. *et al*. Oocyte CD9 is enriched on the microvillar membrane and required for normal microvillar shape and distribution. *Developmental Biology* **304**, 317–325 (2007).
27. Lipner, H. & Cross, N. L. Morphology of the membrana granulosa of the ovarian follicle. *Endocrinology* **82**, 638–641 (1968).
28. Anderson, E. & Albertini, D. F. Gap junctions between the oocyte and companion follicle cells in the mammalian ovary. *The Journal of Cell Biology* **71**, 680–686 (1976).
29. El-Hayek, S., Yang, Q., Abbassi, L., FitzHarris, G. & Clarke, H. J. Mammalian oocytes locally remodel follicular architecture to provide the foundation for germline-soma communication. *Curr. Biol.* **28**, 1124–1131.e3 (2018).
30. Miller, J., Fraser, S. E. & McClay, D. Dynamics of thin filopodia during sea urchin gastrulation. *Development* **121**, 2501–2511 (1995).
31. Danilchik, M., Williams, M. & Brown, E. Blastocoel-spanning filopodia in cleavage-stage Xenopus laevis: Potential roles in morphogen distribution and detection. *Dev. Biol.* **382**, 70–81 (2013).
32. Bentley, D. & Toroian-Raymond, A. Disoriented pathfinding by pioneer neurone growth cones deprived of filopodia by cytochalasin treatment. *Nature* **323**, 323712a0 (1986).
33. Fantin, A. *et al*. NRP1 regulates cdc42 activation to promote filopodia formation in endothelial tip cells. *Cell Rep* **11**, 1577–1590 (2015).
34. Ziv, N. E. & Smith, S. J. Evidence for a role of dendritic filopodia in synaptogenesis and spine formation. *Neuron* **17**, 91–102 (1996).
35. Kornberg, T. B. Distributing signaling proteins in space and time: the province of cytonemes. *Curr. Opin. Genet. Dev.* **45**, 22–27 (2017).
36. Sanders, T. A., Llagostera, E. & Barna, M. Specialized filopodia direct long-range transport of SHH during vertebrate tissue patterning. *Nature* **497**, 628–632 (2013).
37. González-Méndez, L., Seijo-Barandiarán, I. & Guerrero, I. Cytoneme-mediated cell-cell contacts for Hedgehog reception. *Elife* **6** (2017).
38. Roy, S., Huang, H., Liu, S. & Kornberg, T. B. Cytoneme-mediated contact-dependent transport of the Drosophila Decapentaplegic signaling protein. *Science* **343**, 1244624 (2014).
39. Kawase, E., Wong, M. D., Ding, B. C. & Xie, T. Gbb/Bmp signaling is essential for maintaining germline stem cells and for repressing bam transcription in the Drosophila testis. *Development* **131**, 1365–1375 (2004).
40. Elvin, J. A., Clark, A. T., Wang, P., Wolfman, N. M. & Matzuk, M. M. Paracrine actions of growth differentiation factor-9 in the mammalian ovary. *Mol Endocrinol* **13**, 1035–1048 (1999).
41. Su, Y.-Q. *et al*. Synergistic roles of BMP15 and GDF9 in the development and function of the oocyte-cumulus cell complex in mice: genetic evidence for an oocyte-granulosa cell regulatory loop. *Dev. Biol.* **276**, 64–73 (2004).

42. Sun, R. Z. *et al*. Expression of GDF-9, BMP-15 and their receptors in mammalian ovary follicles. *J. Mol. Histol.* **41**, 325–332 (2010).
43. Terasaki, M. *et al*. Stacked endoplasmic reticulum sheets are connected by helicoidal membrane motifs. *Cell* **154**, 285–296 (2013).
44. Cardona, A. *et al*. TrakEM2 software for neural circuit reconstruction. *Plos One* **7**, e38011 (2012).

Acknowledgements
We thank Arthur Hand and Maya Yankova for providing training and suggestions on processing and sectioning samples for EM, Richard Schalek and Jeff Lichtman for advice and continuous support on serial section EM, Ninna Shuhaibar for helping with segmentations, and Rindy Jaffe, Rachael Norris, and Mayu Inaba for thoughtful discussions and critical review of the manuscript. This work was supported by a grant from the Connecticut Science Fund.

Author Contributions
M.T. and V.B. conceived the project. V.B. performed all experiments and data analysis. V.B. and M.T. wrote the manuscript and approved the final version.

Additional Information
Supplementary information accompanies this paper at https://doi.org/10.1038/s41598-018-37766-2.

Competing Interests: The authors declare no competing interests.

Publisher's note: Springer Nature remains neutral with regard to jurisdictional claims in published maps and institutional affiliations.

Chapter 4

Cellular heterogeneity of the LH receptor and its significance for cyclic GMP signaling in mouse preovulatory follicles

Baena, V., Owen, C.M., Uliasz, T.F., Lowther, K.M., Yee, S.-P., Terasaki, M., Egbert, J., Jaffe, L.A., 2020. Cellular heterogeneity of the LH receptor and its significance for cyclic GMP signaling in mouse preovulatory follicles. Endocrinology (in press).
bioRxiv 2020.02.06.937995. https://doi.org/10.1101/2020.02.06.937995

Contributions: V.B. did most of the experiments involving immunofluorescence and immunogold, data analysis for such experiments, and made 4 of the figures in the manuscript. The writing was split between all authors. V.B. helped in the initial conceptualization of the project.

Abstract

Meiotic arrest and resumption in mammalian oocytes are regulated by two opposing signaling proteins in the cells of the surrounding follicle: the guanylyl cyclase NPR2, and the luteinizing hormone receptor (LHR). NPR2 maintains a meiosis-inhibitory level of cyclic GMP (cGMP) until LHR signaling causes dephosphorylation of NPR2, reducing NPR2 activity, lowering cGMP to a level that releases meiotic arrest. However, the signaling pathway between LHR activation and NPR2 dephosphorylation remains incompletely understood, due in part to imprecise information about the cellular localization of these two proteins. To investigate their localization, we generated mouse lines in which HA epitope tags were added to the endogenous LHR and NPR2 proteins, and used immunofluorescence and immunogold microscopy to localize these proteins with high resolution. The results showed that the LHR protein is absent from the cumulus cells and inner mural granulosa cells, and is present in only 13-48% of the outer mural granulosa cells. In contrast, NPR2 is present throughout the follicle, and is more concentrated in the cumulus cells. Less than 20% of the NPR2 is in the same cells that express the LHR. These results suggest that to account for the LH-induced inactivation of NPR2, LHR-expressing cells send a signal that inactivates NPR2 in neighboring cells that do not express the LHR. An inhibitor of gap junction permeability attenuates the LH-induced cGMP decrease in the outer mural granulosa cells, consistent with this mechanism contributing to how NPR2 is inactivated in cells that do not express the LHR.

Introduction

In mammalian preovulatory follicles, meiotic arrest is maintained by cyclic GMP (cGMP) that diffuses into the oocyte through gap junctions (1-3). The cGMP is generated in the granulosa

cells of the follicle by the guanylyl cyclase natriuretic peptide receptor 2 (NPR2, also called guanylyl cyclase B) (4,5). cGMP then passes through the multilayer tissue to the oocyte by way of gap junctions formed by connexin 43 and connexin 37 (6-8). Regulation of meiotic arrest by cGMP generated by NPR2 appears to be conserved among mammals (1) including humans (9).

Mammalian oocytes resume meiosis in response to luteinizing hormone that activates a G-protein-coupled receptor (the luteinizing hormone / chorionic gonadotropin receptor, LHCGR, referred to here as LHR, since mice do not produce chorionic gonadotropin). LHR activation initiates signals that cause cGMP in the granulosa cells to decrease (1,3). The decrease in cGMP to a meiosis-permissive level requires the dephosphorylation and inactivation of NPR2 (10-12). Phosphorylation and activation of the PDE5 cGMP phosphodiesterase, and other unknown mechanisms, also contribute to the LH-induced cGMP decrease (13). Due to diffusion through gap junctions, cGMP then decreases in the oocyte (6,7,14).

While the necessity of NPR2 inactivation for LH-induced meiotic resumption is established (12), the signaling pathway between the LHR and NPR2 dephosphorylation remains incompletely understood, due in part to imprecise information about the localization of these two proteins. In particular, it is unknown whether the approximately 50% decrease in NPR2 activity that occurs in response to LH signaling (10,11) could result from inactivation of NPR2 solely in cells that express the LHR, or whether NPR2 in other cells must also be inactivated.

In previous studies, the localization of the LHR and NPR2 has been investigated by binding of radiolabeled mRNA probes and receptor ligands. These studies indicated that the LHR is located in the outer mural granulosa cell region of preovulatory follicles and in the theca and interstitial cells surrounding the follicle (15-20). mRNA encoding NPR2 is located in all regions of the granulosa compartment, but not in the oocyte (4,21). NPR2 mRNA is more concentrated in the

cumulus cell region (the granulosa cells directly surrounding the oocyte) and in the region of the mural granulosa closest to the antral space. However, these previous studies involved autoradiographic imaging and did not provide cellular level resolution, due to the scattering of the radiation emitted by the ~7-20 μm thick histological sections, as well as the thickness of the overlying silver emulsion. In addition, mRNA localization does not provide direct information about protein levels. Antibodies that allow definitive immunolocalization of LHR and NPR2 within the follicle have not been developed, likely due to the difficulties of generating antibodies against G-protein coupled receptors and other transmembrane proteins (22), as well as the low expression levels of the LHR and NPR2.

To overcome this problem, we generated mice with a 9-amino acid hemagglutinin (HA) tag added to the extracellular N-termini of the endogenous LHR and NPR2 proteins. Because highly specific antibodies that recognize the HA peptide are available, this strategy has been used effectively to immunolocalize endogenous membrane proteins with low expression levels (23, 24). Using immunofluorescence and confocal microscopy, as well as immunogold and serial section electron microscopy, we investigated the localization of the LHR and NPR2 in preovulatory follicles, with much higher resolution than possible with previous methods. The distinct cellular localizations of these proteins indicate that LH-induced inactivation of NPR2 requires intercellular communication

Materials and Methods

Mice

CRISPR/Cas9 genome editing was used to generate two mouse lines in which a 9-amino acid HA epitope tag (YPYDVPDYA) was added to the extracellular N-termini of the endogenous

LHR and NPR2 proteins; these modified proteins and mouse lines are referred to here as HA-LHR and HA-NPR2. The positions where the HA sequences were inserted (Fig. 1A,B) were the same as previously used to tag the LHR (25) and NPR2 (26,27) in cell lines.

Single guide RNAs (sgRNA) with sequences specific to the *Lhcgr* and *Npr2* genes, and single stranded DNA (ssDNA) donors for *Lhcgr* and *Npr2*, were obtained from Integrated DNA Technologies (Table 1). Cas9 protein was purchased from MilliporeSigma. Cas9 protein (50 ng/µl) and sgRNA (25 ng/µl) were incubated for 10 min at room temperature in injection buffer (10 mM Tris, pH 7.5, 0.1mM EDTA) and then mixed with ssDNA donor (40 ng/µl).

The Cas9/sgRNA ribonucleoprotein (RNP) complex and ssDNA donor mixture was microinjected into the pronuclei of C57BL/6J one-cell embryos. Injected embryos were transferred into CD1 foster females for subsequent development. Founder animals were initially identified by PCR using primer pairs (LHR E1F and LHR E1R, Table 1) to amplify fragments of 232 bp and 260 bp specific for *Lhcgr* and HA-tagged *Lhcgr*, respectively, and primer pairs (Npr2F E1F and Npr2F E1R, Table 1) to amplify fragments of 270 bp and 307 bp specific for *Npr2* and HA-tagged *Npr2*. Founder animals were confirmed by PCR followed by sequencing of the amplicon using the primer pairs as described above. Founders were then bred with wildtype C57BL/6J mice to expand the line, and the mice were maintained on a C57BL/6J background.

Table 1. DNA sequences for generation and genotyping of HA-LHR and HA-NPR2 mice.

Type of sequence	Name	Sequence
sgRNA	*Lhcgr*	5'- CAG CGC GAC CCT GAC AAC TC
	Npr2	5'- AGC GTC AGG TTC CGT GCC CC
ssDNA donor	*Lhcgr*	5'- CAG GCT GGC GGG CCA TGG GGC GGC GGG TCC CGG CTC TGA GAC AGC TGC TGG TGC TGG CAA TGC TGG TGC TGA AGC AGT CAC AGC TGC ACT CTT ACC CAT ACG ATG TTC CAG ATT ACG CTC CAG AAC TCT CAG GGT CGC GCT GCC CTG AGC CCT GCG ACT GCG CGC CGG ATG GTG CCC TGC GCT G
	Npr2	5'- GTG GGT CAG CTG CTC TAT CCC CAT GGC ACT GCC ATC CCT GCT GCT GGT GGT GGC AGC CCT GGC AGG TGG GGT GCG TCC TCC GGG GGC ATA CCC ATA CGA TGT TCC AGA TTA CGC TGG CGC TGC CCG GAA CCT GAC GCT GGC GGT GGT GCT GCC AGA ACA CAA CCT GAG CTA TGC CTG
Primer	LHR E1F	5'- CTG GCC TAG CCA CCG GAG CTC
	LHR E1R	5'- CTG GGG CGC CCT GTA CTC ACA G
	Npr2F E1F	5'- CCT GGC CCT CTT CCC CAG GCT C
	Npr2F E1R	5'- GTG CCT CCA CAG CCA GTG CCA C

The HA-LHR and HA-NPR2 mouse lines were maintained by breeding of homozygotes, and all studies were performed using homozygous mice and wildtype controls. Fertility data were obtained by counting the cumulative number of pups produced over 4 months by each homozygous breeding pair, and by wild-type breeding pairs maintained in parallel.

An additional mouse line, expressing a sensor for cGMP (cGi500; 28), was provided by Robert Feil (University of Tübingen), and was maintained on a C57BL/6J background. Imaging studies using the cGi500 mice were performed using heterozygotes.

Mice were housed in a room with a 14 hour light/10 hour dark cycle (lights on at 0200 h, off at 1600 h). All experiments were conducted as approved by the University of Connecticut Health Center animal care committee.

Ovaries, ovarian follicles, and gonadotropins

Except as indicated, ovaries were obtained by injecting 22-24 day old immature mice intraperitoneally with equine chorionic gonadotropin (eCG, 5 I.U.; National Hormone and Peptide Program, AFPSuperOv) to stimulate follicle growth to the preovulatory stage. 44 hours later, ovaries were dissected. To prepare samples for western blots, follicles ~470-540 μm diameter were manually dissected from eCG-injected mice.

To obtain ovaries from adult mice on the day of proestrus, the stage of the estrous cycle was visually assessed by observation of the vaginal opening (29). Ovaries from mice that appeared to be at proestrus were collected at 1030 h to 1200 h, since serum LH levels begin to rise approximately one hour before the mouse room lights are turned off (30), and the lights in our mouse room were turned off at 1600 h. In this way, we obtained ovaries close to the time of the LH surge but avoided the possibility that the surge had already begun. The proestrous staging was confirmed by the presence of preovulatory follicles in ovary sections.

To test the effect of FSH on LHR protein expression, to determine the time course of nuclear envelope breakdown in response to LH, and to measure LHR mRNA by quantitative RT-PCR, follicles (~320-400 μm diameter) were isolated from 23-26 day old mice that had not been injected with eCG. The isolated follicles were cultured for 24 hours with 1 nM FSH to stimulate LHR expression (6,31). Where indicated, the follicles were then incubated with 10 nM or 100 nM LH. Highly purified ovine FSH and LH were obtained from the National Hormone and Peptide Program (AFP7558C and LH-26, respectively). Nuclear envelope breakdown was scored by observation of intact follicles cultured on organotypic membranes (Millipore, Cork IR) such that the prophase arrested nucleus (germinal vesicle) could be seen within the follicle-enclosed oocyte (12).

Western blots

Samples were prepared for SDS-PAGE by sonicating follicles in sample buffer with protease and phosphatase inhibitors (6). For all blots, 20 μg of protein was loaded per lane. The protein content of preovulatory follicles from eCG-injected mice is ~6 μg (Pierce BCA protein assay kit, 23225, Thermo Fisher Scientific). The protein content of follicles (~320-400 μm diameter) from mice that were not injected with eCG, and which were treated with FSH in vitro, is ~3.5 μg (6). Antibodies and stock concentrations are listed in Table 2. The primary antibody against the HA tag (32) was used at a dilution of 1:1000. The secondary antibody (33) was used at a dilution of 1:20,000. Blots were developed with a WesternBright Sirius Chemiluminescent Detection kit (Advansta, K-12043).

Table 2. Antibodies

Name	**Source**	**Stock concentration**
rabbit monoclonal antibody against HA tag; RRID: AB_1549585	Cell Signaling Technology, 3724, lot 9	67 μg/ml
goat anti-rabbit IgG (H+L), HRP conjugate; RRID: AB_10719218	Advansta, R-05072-500	1 mg/ml
goat anti-rabbit IgG 488-Alexa Fluor secondary antibody; RRID: AB_2576217	Thermo Fisher Scientific, Molecular Probes, A-11034	2 mg/ml
goat anti-rabbit IgG Alexa Fluor 488 - FluoroNanogold secondary antibody; RRID: AB_2819209	Nanoprobes, 7203	80 μg/ml

Quantitative RT-PCR

Total RNA was purified from isolated follicles that had been cultured for 24 hours with FSH as described above. RNA was isolated using the RNeasy Micro kit (Qiagen) and reverse transcribed using the SuperScript III kit (Invitrogen) with random primers according to manufacturer's instructions. Forward and reverse primers (Table 3) were validated by performing a standard curve with cDNA to determine the linear range of each set of primers. Quantitative RT-PCR was performed using the iTaq SYBR Green Supermix (Bio-Rad) and a CFX Connect Detection System (Bio-Rad). Assays were performed in duplicate. The cycle threshold method was used to calculate relative expression levels after normalization to TATA binding protein *(Tbp)* levels

Immunofluorescence labeling of ovary sections

Ovaries were fixed in 4% paraformaldehyde (a 1:1 mixture of 8% paraformaldehyde, Electron Microscopy Sciences (EMS) 157-8, and PBS) for 4 hours at room temperature, then rinsed 3 times in PBS (5 minutes each). The fixed ovaries were transferred to 15% sucrose at 4^{o}C until they sank, transferred to 30% sucrose at 4^{o}C until they sank, then embedded in OCT medium (EMS 62550-01) and frozen in a slurry of dry ice and ethanol. Ten or 20 µm thick cryostat sections were collected on slides and rinsed 3 times with PBS. Sections were blocked with 5% normal goat serum and 1% BSA in PBS, then labeled with the HA-tag antibody (32) listed in Table 2 (1:500 dilution in the blocking solution) for 1 hour at room temperature. The sections were washed with PBS several times, labeled with a goat anti-rabbit 488-Alexa Fluor secondary antibody (34) (see Table 2, 1:500 dilution) for 1 hour at room temperature, then washed several times in PBS. Some sections were additionally labeled with 4′,6-diamidino-2-phenylindole

(DAPI, Sigma D9542, 0.5 µg/ml in PBS, for 15 min at room temperature, followed by 5 x 3 min washes in PBS) to label nuclei. Labeled sections were mounted with Shandon Immu-Mount (Thermo Fisher Scientific 9990402) and a #1 coverslip.

Table 3. Primers for RT-PCR quantitation of mRNA encoding LHR

Primer	Sequence
LHRF	5'- ACC TGC TAT ACA TTG AAC CCG
LHRR	5'- GAT CTT CGA AAC ATC TGG GAG G
LHR2F	5'- GGC CTC GCC CGA CTA TCT CTC
LHR2R	5'- CGA AAC ATC TGG GAG GGT CCG G
TBPF	5'- TGC TGT TGG TGA TTG TTG GT
TBPR	5'- CTG GCT TGT GTG GGA AAG AT
LHRF	5'- ACC TGC TAT ACA TTG AAC CCG

RNAscope labeling of ovary sections

RNAscope was performed using a RNAscope Fluorescent Multiplex Reagent kit (Advanced Cell Diagnostics, 320850) and a probe designed for *Lhcgr* (Advanced Cell Diagnostics, 408171). Ovaries from eCG-injected mice were obtained as described above and frozen in OCT without fixation. RNAscope was performed according to the kit protocol. Briefly, 10 µm thick cryosections were fixed in 4% paraformaldehyde for 15 minutes at 4°C, then dehydrated in 50%, 70%, 100%, and 100% ethanol for 5 minutes each. Slides were dried, treated with Protease IV for 30 minutes at 40°C, then washed twice with PBS. The probe was applied to the slide for 2 hours in a humidified chamber at 40°C followed by the 4 amplification steps using amplification reagent B (orange fluorophore). Slides were washed, treated with DAPI, and mounted with Shandon Immu-Mount.

Confocal microscopy and analysis

Ovary sections were imaged with a confocal microscope (Pascal or LSM800, Carl Zeiss Microscopy) and images were saved as 12-bit or 16-bit files. For analysis of protein localization, the outer and inner regions of the mural granulosa layer were defined as follows: The width of the mural granulosa layer was measured from the basal lamina to the antrum at 8 radial points in the follicle, and the halfway point was marked. The points were connected to mark the boundary between the inner and outer mural cells.

To determine the proportion of outer mural granulosa cells that expressed the LHR, 10 μm sections that had been co-stained with DAPI were used to count cells with the Cell Counter Tool in Fiji (35). DAPI-stained nuclei that were surrounded by HA labeling were counted as LHR-positive cells. DAPI-stained nuclei without HA labeling were counted as LHR-negative cells. Cell counts were made from a series of 10 optical sections taken at 1 μm intervals and having an approximate optical section thickness of ~1.5 μm. A similar method was used to determine the fraction of LHR-expressing cells in the layer of cells with cell bodies directly adjacent to the basal lamina.

To determine the relative expression levels of HA-NPR2 in each region of the follicle, z-stacks of confocal images were collected from 20 μm thick sections located at the level of the oocyte. Intensity measurements were made from the central optical section, using Image J. Background intensities for each region were determined by performing similar measurements using wildtype follicles. The average background fluorescence intensity was subtracted from the intensities measured from HA-NPR2 follicles. Background-subtracted intensity values for each region of each HA-NPR2 follicle were normalized to the intensity of the cumulus cells.

Immunogold labeling of vibratome slices of ovary

Ovaries were fixed in 4% paraformaldehyde (prepared as described above for immunofluorescence) overnight at 4^{o}C, then rinsed 3 times in PBS (5 minutes each) and embedded in 4% low gelling temperature agarose in PBS (Sigma-Aldrich A0701). 55 μm slices of the ovaries were cut with a vibratome (Leica VT 1000 S) and were collected and further processed in glass depression wells. After a few washes with PBS, the slices were permeabilized with Triton X-100 (Thermo Fisher Scientific, 28314) in PBS for 20 minutes with gentle shaking. 0.1% Triton X-100 was used to obtain optimal preservation for thin sectioning, and 0.3% Triton X-100 was used to achieve higher antigen labeling for thick sectioning.

All subsequent steps were carried out with gentle shaking at room temperature unless specified otherwise. Slices were rinsed once with PBS, treated with 5% normal goat serum, 1% BSA, and 0.1% Triton X-100 in PBS for 30 minutes to block non-specific binding, then labeled with the HA-tag antibody (32) listed in Table 2. The antibody was used at a 1:100 dilution (for thin sectioning) or 1:300 (for thick sectioning), in the blocking solution overnight. Slices were then washed with PBS 5 times for 5 minutes each and then treated with the blocking solution for 30 minutes. After blocking, slices were incubated in a secondary antibody conjugated to Alexa Fluor 488 and nanogold (36) (see Table 2), at a dilution of 1:100 (for thin sectioning) or 1:200 (for thick sectioning). The secondary antibody was diluted in the blocking solution but without Triton X-100, and was applied for 4 hours in the dark. Slices were then washed with PBS 5 times for 5 minutes each, placed in a drop of PBS on a glass slide, and the fluorescence was checked using an epifluorescence microscope.

Slices were then fixed with 1% glutaraldehyde diluted in PBS from an 8% aqueous solution

(EMS 16020) for 10 minutes, followed by 3 PBS washes for 3 minutes each, then 5 washes with 0.1 M Tris buffer for 3 minutes each. The nanogold was enhanced with a gold enhancement kit (GoldEnhance EM Plus, Nanoprobes 2114) for 9 minutes following the manufacturer's instructions. The enhancement was stopped by washing the slices with 0.1 M Tris buffer 5 times for 2 minutes each, followed by 5 washes with PBS for 2 minutes each. The slices were then transferred to capped glass vials and postfixed with 1% osmium tetroxide diluted in PBS from a 4% aqueous solution (EMS 19170) for 30 minutes on a rotator. The slices were washed with 5 rinses of Milli-Q water for 2 minutes each, then placed in 1% uranyl acetate in water (EMS 22400) and stored at 4^{o}C overnight. The next day, they were washed with 5 rinses of Milli-Q water for 2 minutes each.

The slices were dehydrated in sequential ethanol solutions, infiltrated with Epon resin (Embed-812 kit, EMS 14121), and flat-embedded in the same resin between two pieces of ACLAR embedding film with a 50 μm thickness (EMS 50426) using 2 pieces of Parafilm as spacers between them and a glass slide on top to provide weight to flatten the slices. The resin was polymerized in a 60^{o}C oven for at least 20 hours, and the embedded slices were then attached to blank Epon blocks using superglue.

Sectioning and imaging for electron microscopy, and analysis of images

Trimming, sectioning, imaging, and image alignment were done as previously described (37,38) with the following modifications: For thin sectioning of the samples that were treated to enhance the preservation of structures, serial sections were cut at a thickness of 65 nm. For thick sectioning of the samples that were treated to enhance antigen labeling, the serial sections were cut at 500 nm.

Reconstructions were made using the TrakEM2 module (39) from FIJI by manually segmenting cell outlines or the basal lamina on the serial sections using arealists. The surface areas of cell contacts with the basal lamina were estimated from the Upper Bound smoothened measurement of the arealists.

Live confocal imaging of isolated follicles to measure cGMP levels

Measurements of cGMP were made using mice expressing the cGi500 Förster resonance energy transfer (FRET) sensor (28,40). Methods were as previously described (13,14), except that LH was used at a concentration of 10 nM instead of 300 nM. Carbenoxolone (CBX) was obtained from MilliporeSigma (C4790).

Fluorescence recovery after photobleaching

Measurements were performed and analyzed as previously described (14).

Statistics

All analyses were conducted using Prism 6 (GraphPad Software, La Jolla, CA). Details are given in the figure legends.

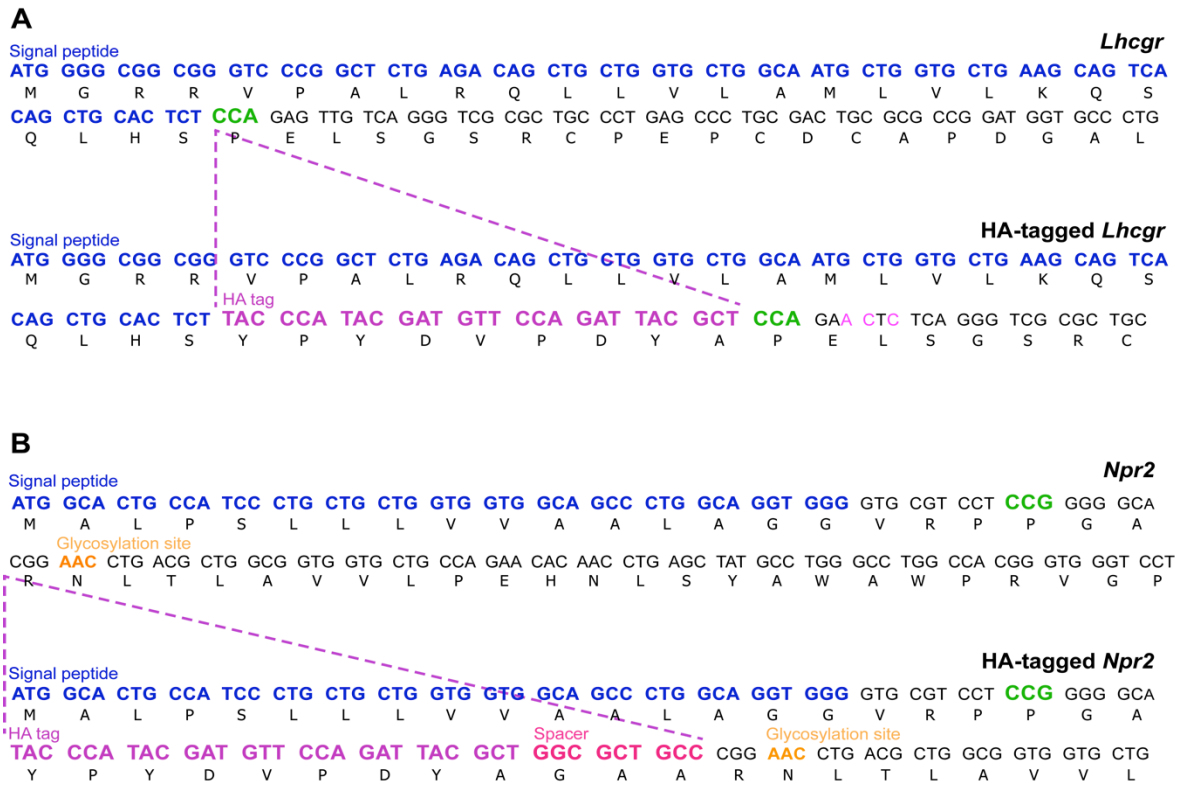

Figure 1. Generation of HA-LHR and HA-NPR2 mouse lines. (A) CRISPR-mediated gene editing was used to insert an HA tag (shown in purple) together with three silent point mutations (shown in pink) in the N-terminus of the *Lhcgr* coding sequence. The point mutations were located adjacent to the PAM site (shown in green) to eliminate re-cleavage of the HA-tagged *Lhcgr* allele. (B) An HA tag followed by a 3 amino acid spacer (shown in pink) was inserted into the *Npr2* coding sequence right after alanine 22 in the N-terminus. The spacer was used to separate the HA tag from an NPR2 glycosylation site (shown in orange). Signal peptides are shown in blue, and coding sequences in black.

Results

Validation of mice with HA-tagged LHR and NPR2

To determine whether mice in which an HA epitope tag was added to the N-terminus of the endogenous LHR produced a protein of the expected size and with the expected developmental profile, proteins from isolated preovulatory follicles, obtained from eCG-stimulated mice, were examined by western blotting. As predicted from the HA-LHR sequence, an HA-positive band was seen at ~80 M_r (Fig. 2A). Some lower molecular weight bands were also present, presumably representing breakdown products or splice variants. The ~80 M_r and lower

molecular weight bands were absent in follicles from wildtype mice, although one non-specific band at ~116 M_r was seen in both HA-LHR and wildtype follicles (Fig. 2A,B). Further confirming the appropriate expression of the HA-LHR protein, the ~80 M_r and lower molecular weight HA-positive bands were absent in follicles that had not been exposed to follicle-stimulating hormone (FSH), a hormone that stimulates expression of the LHR (15,16,41) (Fig. 2B).

Follicles from mice in which an HA epitope tag was added to the N-terminus of the endogenous NPR2 also showed expression of a protein of the appropriate molecular weight, at ~120 and ~130 M_r (Fig. 2C), as expected based on its known glycosylation (11). As with the HA-LHR mice, a non-specific band was present at ~116 M_r. Ideally, different epitope tags would have been used for the two lines, to allow colocalization of the two proteins. We also made mice expressing NPR2 with a FLAG tag (DYKDDDDK; 42) or a PA tag (GVAMPGAEDDVV; 43) in the same position as described for the HA tag. However, in contrast to the HA-tagged mice described here, follicles from mice with FLAG-tagged or PA-tagged NPR2 did not show specific labeling with western blots and immunofluorescence. Thus, of the three tags that we compared, only HA was useful with the antibodies that we tested, probably due to low expression levels of NPR2.

HA-LHR and HA-NPR2 homozygous breeding pairs produced approximately the same number of pups as wildtype mice, indicating no obvious defect in their fertility (Fig. 2D). To further test whether these mice showed normal ovarian function, we examined the response of isolated follicles to LH. Oocytes within HA-LHR- and HA-NPR2-expressing follicles resumed meiosis, as indicated by nuclear envelope breakdown (Fig. 2E). For HA-LHR-expressing follicles, the response to 100 nM LH showed kinetics similar to wildtype, but the response to 10

nM LH was slightly slower than in wildtype and occurred in only about 75% of the follicles. This slight attenuation could potentially be due to an effect of the HA tag on the level of LHR mRNA, or on the binding affinity of the receptor. Quantitative PCR analysis indicated that the amount of LHR-encoding mRNA in follicles from HA-LHR-expressing mice was ~40% of that from wildtype mice (Fig. 2F). However, these differences were not sufficient to be obviously detrimental to fertility.

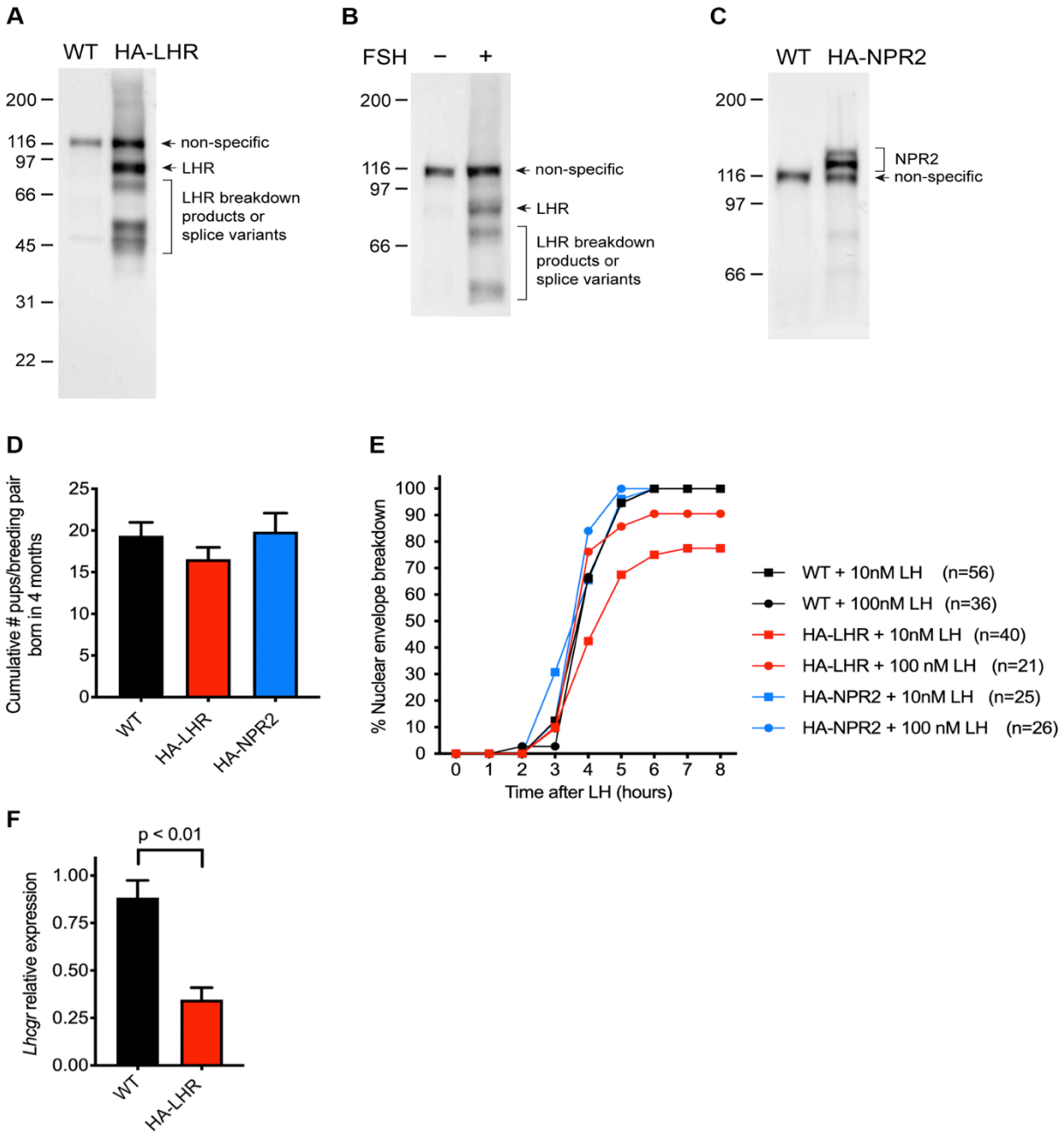

Figure 2. Validation of the size, expression, and biological activity of the HA-LHR and HA-NPR2 proteins in the genetically modified mice. (A-C) Western blots of preovulatory follicles, probed with an HA tag antibody. (A) Follicles from HA-LHR and wildtype (WT) mice. (B) Follicles from HA-LHR mice, with and without a 24 hour incubation of the follicles with FSH. (C) Follicles from HA-NPR2 and WT mice. (D) No obvious defect in fertility of HA-LHR and HA-NPR2 mice, as judged by the number of pups produced in 4 months by homozygous breeding pairs, compared with wild-type pairs (mean ± SEM; 9 pairs for WT, 14 pairs for HA-LHR, and 8 pairs for HA-NPR2). Data were analyzed by one-way ANOVA with the Holm-Sidak correction for multiple comparisons. No differences in the cumulative number of pups per breeding pair were observed ($p > 0.05$). (E) Time course of nuclear envelope breakdown in response to 10 or 100 nM LH, comparing HA-LHR, HA-NPR2, and WT follicles. Nuclear envelope breakdown was scored by observation of live follicles (6). The results were obtained from 5 independent experiments, 3 of which included parallel tests of HA-LHR and wildtype follicles incubated with 10 nM LH. n

values indicate the total number of follicles tested for each condition. (F) Relative expression of *Lhcgr* mRNA in pools of 4-15 follicles cultured for 24 hours with FSH from WT and HA-LHR mice (n = 5 mice for each genotype). Total RNA was isolated and reverse transcribed, and levels of *Lhcgr* were measured using qRT-PCR with primers LHRF and LHRR (Table 3) and normalized to levels of *Tbp*. Data are reported as mean fold change ± SEM and were analyzed by an unpaired t test. Similar results were obtained by analysis of the same samples using a different pair of primers, LHR2F and LHR2R in Table 3.

Localization of the LHR in a subset of the outer mural granulosa cells

To investigate the localization of the LHR, we examined frozen sections of formaldehyde-fixed ovaries from HA-LHR-expressing mice; sections were labeled with an HA-tag antibody (32). Confirming previous mRNA and ligand binding studies (15-20), the LHR was localized in the outer layers of mural granulosa cells of preovulatory follicles, but not in the inner mural cells, cumulus cells, or oocyte (Fig. 3A,C). HA-antibody labeling was not seen in the mural granulosa cells of wildtype follicles (Fig. 3B,D), or in the granulosa cells of follicles that had not grown to the preovulatory stage (Fig. 3A). In ovaries of HA-LHR-expressing mice, a variable degree of HA-antibody labeling was also detected in some of the theca and interstitial cells that surround the follicle (see examples in figures 3 and 4).

Many of the LHR-expressing mural granulosa cells were flask-shaped, with long projections extending to the basal lamina from cell bodies several layers deep (Fig. 3E), comprising a pseudostratified epithelium (37,44). Most of the LHR protein was located at the cell surface, although some appeared to be intracellular. Strikingly, only some of the cells in the outer half of the mural granulosa cell region of preovulatory follicles expressed the LHR (Fig. 3E and other examples in figures 3-5). Some areas of the outer mural region showed intense labeling, while others showed none. On a cellular level, some cells were labeled, while some adjacent cells were not.

To quantify the fraction of cells in the outer half of the mural granulosa region that expressed the LHR, we labeled cell nuclei with DAPI and counted the total number of cells in a 10 μm

thick equatorial section of an HA-LHR follicle (see Materials and Methods, Fig. 4A,B, and video 1). We also counted the number of these cells that expressed the LHR from images like that shown in Fig. 4B and video 1. In 13 preovulatory follicles from four mice injected 44 hours previously with the FSH receptor agonist eCG, LHR expression was seen in less than half of the outer mural granulosa cells, with percentages ranging from 13% to 48% (Fig. 4C). Similar results were obtained from mice injected with eCG 24, 36, 40 or 48 hours previously, although less labeling was seen at 12 hours after eCG injection and no labeling was seen in ovaries from mice without eCG injection (Fig. 4C). Analysis of the subpopulation of mural cells whose cell bodies are in direct contact with the basal lamina also showed that only 9-53% of these cells expressed the LHR (Fig. 4D)

The results described above were obtained using ovaries from immature (24-26 day old) mice. Although eggs obtained from such mice are capable of normal development (45), we also examined LHR expression in ovaries from adult mice on the day of proestrus. In these ovaries as well, only 16 to 46% of the outer mural granulosa cells expressed the LHR (Fig. 4C,E).

To test whether the HA tag might be causing the heterogenous expression pattern, we examined the localization of mRNA encoding the LHR in wildtype follicles. As seen for the LHR protein in HA-LHR follicles, the LHR mRNA in wildtype follicles was not uniformly expressed within the outer mural granulosa region (Fig. 4F).

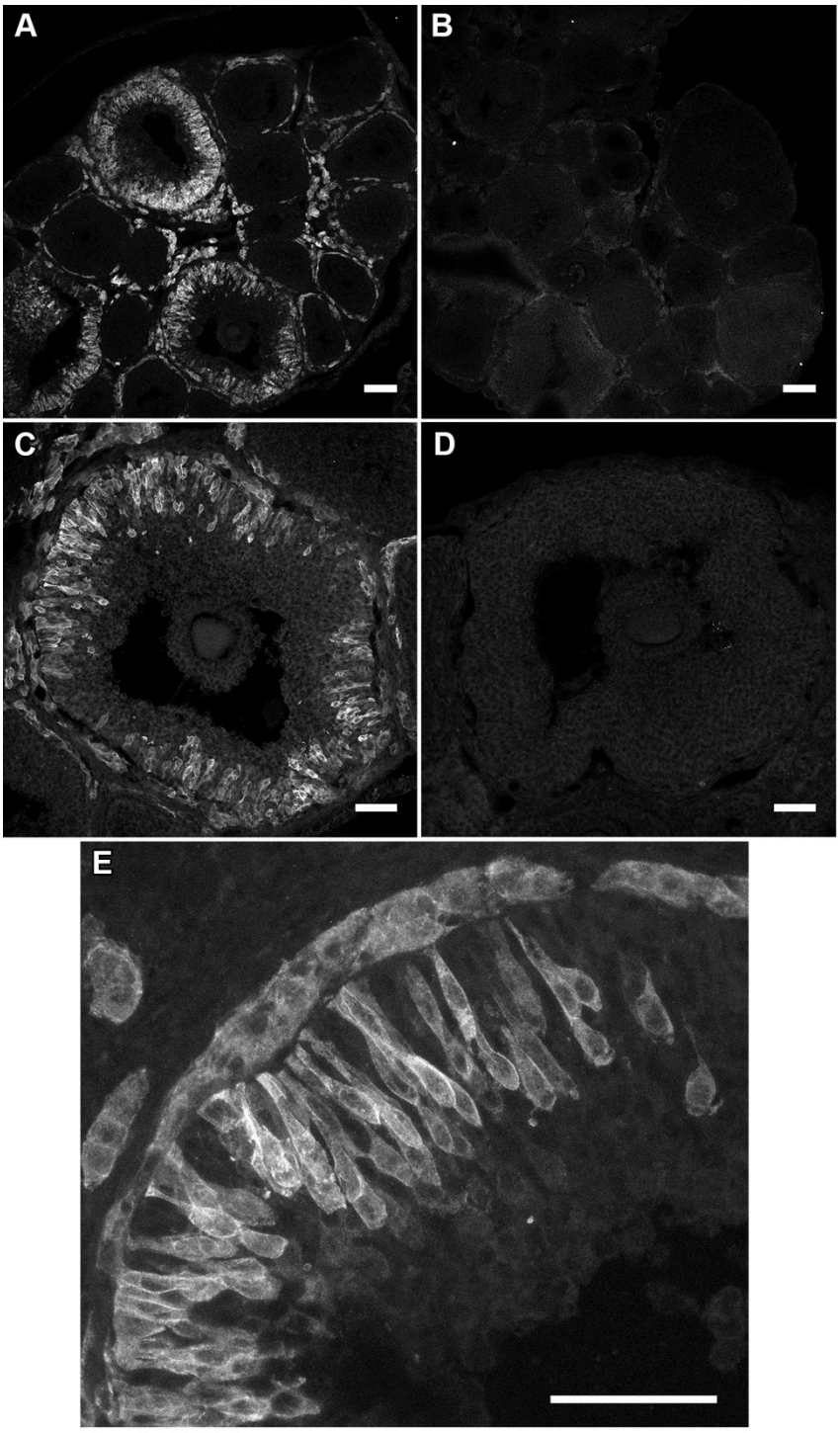

Figure 3. Cellular heterogeneity of the LHR in preovulatory follicles. Ovaries were collected from immature HA-LHR (A,C,E) or wildtype (B,D) mice that were injected 44 hours previously with eCG. All sections were labeled with an HA tag antibody. HA-LHR and wildtype sections were labeled and imaged using identical conditions. A and B show single optical sections. C-E show maximum projections of 11 optical sections imaged at 1 μm intervals. Scale bars indicate 100 μm for A and B, 50 μm for C-E.

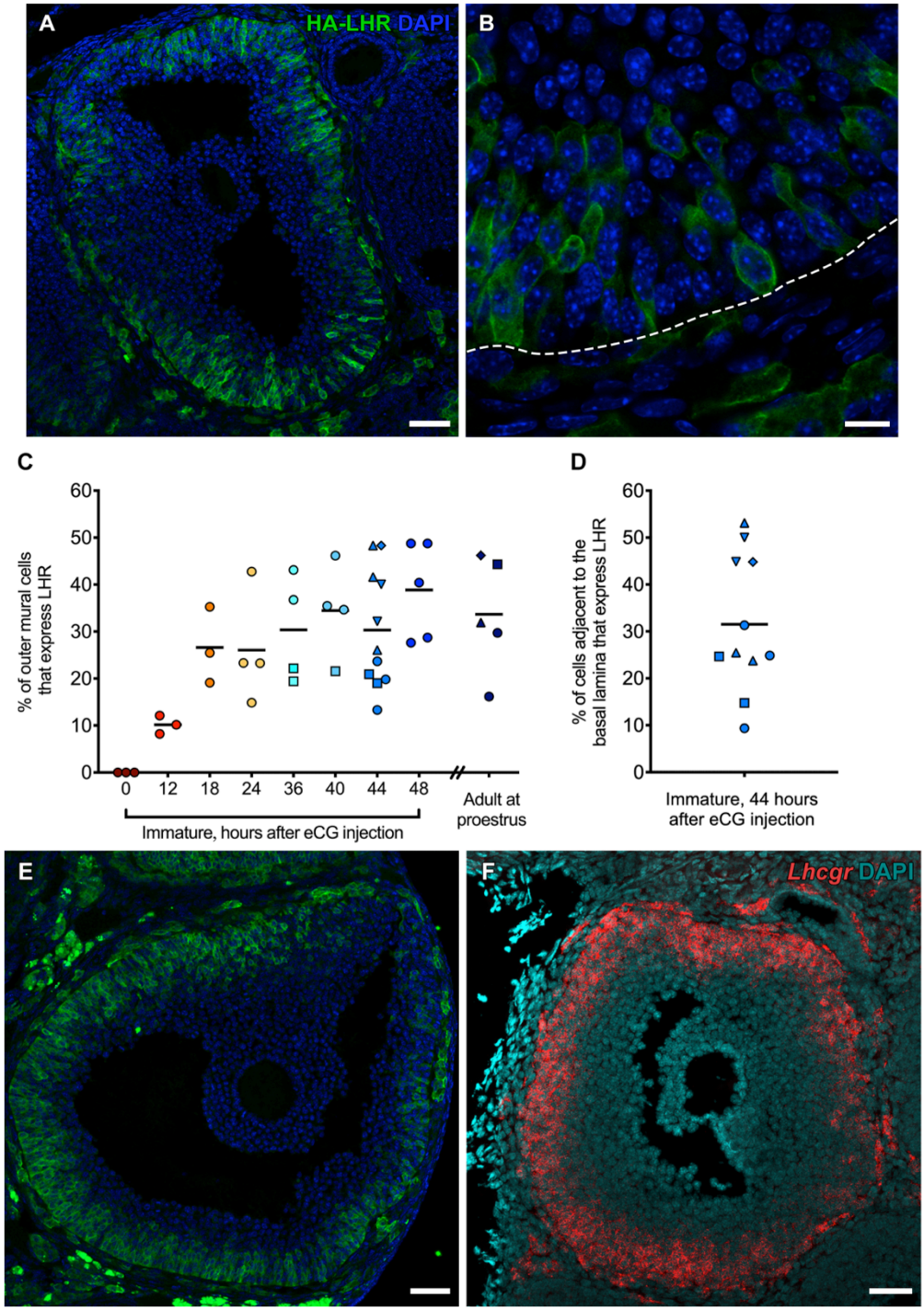

Figure 4. Quantitation of the fraction of outer mural granulosa cells that express the LHR, in immature mice after eCG injection and in adult mice at proestrus. (A) Preovulatory follicle from an ovary of an immature HA-LHR mouse that was injected 44 hours previously with eCG. HA-LHR in green, DAPI-labeled nuclei in blue. Maximum projection of 10 confocal images taken at 1 µm intervals. (B) High magnification image of a single section from a region of the follicle in A. The dotted line indicates the basal lamina. Video 1 shows the stack of confocal images through the 10 µm physical section. (C) Percentage of outer mural granulosa cells that express the LHR in immature mice at various times after injection of eCG, and in adult mice at proestrus. For each time point, different symbols

indicate different mice, and the horizontal bar indicates the mean value. (D) Percentage of cells with cell bodies directly adjacent to the basal lamina that express the LHR, in immature mice at 44 hours after injection of eCG. (E) Preovulatory follicle in the ovary of an adult mouse at proestrus. Maximum projection of 10 confocal images taken at 1 μm intervals. (F) Localization of the mRNA encoding the LHR in a preovulatory follicle from an ovary of an immature wildtype mouse that was injected 44 hours previously with eCG. mRNA in red, DAPI-labeled nuclei in blue. Representative of results from 11 follicles from 3 mice. Scale bars indicate 50 μm for A, E, and F; 10 μm for B.

Localization of LHR by immunogold labeling and serial section electron microscopy

To compare the morphology of LHR-expressing and non-expressing cells, and to investigate their intercellular contacts, we used immunogold labeling and serial section electron microscopy to reconstruct the shapes of both cell types. 55 μm thick vibratome slices of formaldehyde-fixed ovaries were permeabilized with Triton X-100, and the HA epitope was labeled with nanogold prior to embedding and sectioning. The gold label appeared black as viewed with transmitted light, and the labeling pattern confirmed that the LHR protein is distributed in a subset of the outer mural granulosa cells of preovulatory follicles, and in some cells outside of the basal lamina (Fig. 5A).

500 nm sections of these slices showed gold particles bound to some of the outer mural granulosa cells as well as to some of the cells in the theca interna, theca externa, and stroma layers (Fig. 5B). Multiple cell types with functions that are only partly known are present within these layers (46).

Analysis of 225 serial sections, each 65 nm thick, allowed precise definition of all of the LHR-expressing and non-LHR-expressing cells in a 15 μm thick volume (Fig. 5C-E, video 2). The thin section images showed that the LHR protein was most concentrated in the plasma membrane, but some was in the nuclear envelope and cytoplasm (Fig. 5C, video 2). Tracing of individual cells through multiple serial sections showed that almost all of the LHR-expressing cells contacted the basal lamina, either at the cell body or by way of a long projection (Fig.

5C,D). The rare LHR-expressing cells that did not appear to contact the basal lamina were located near the middle of the granulosa layer. Non-LHR-expressing cells had similar shapes and also sent projections to the basal lamina, making similar contact sites (Fig. 5D-F). Thus, basal lamina contact is not sufficient for LHR expression. There was no obvious relationship between proximity to blood capillaries near the basal lamina (see Fig. 5B) and expression of the LHR in adjacent granulosa cells.

Serial section reconstruction also identified gap junctions (Fig. 6 and video 3) and fine cellular processes (Fig. 5D) connecting HA-LHR-expressing and non-expressing mural granulosa cells. As will be described below, these gap junctions function in signaling between the LH receptor and the NPR2 guanylyl cyclase in adjacent cells.

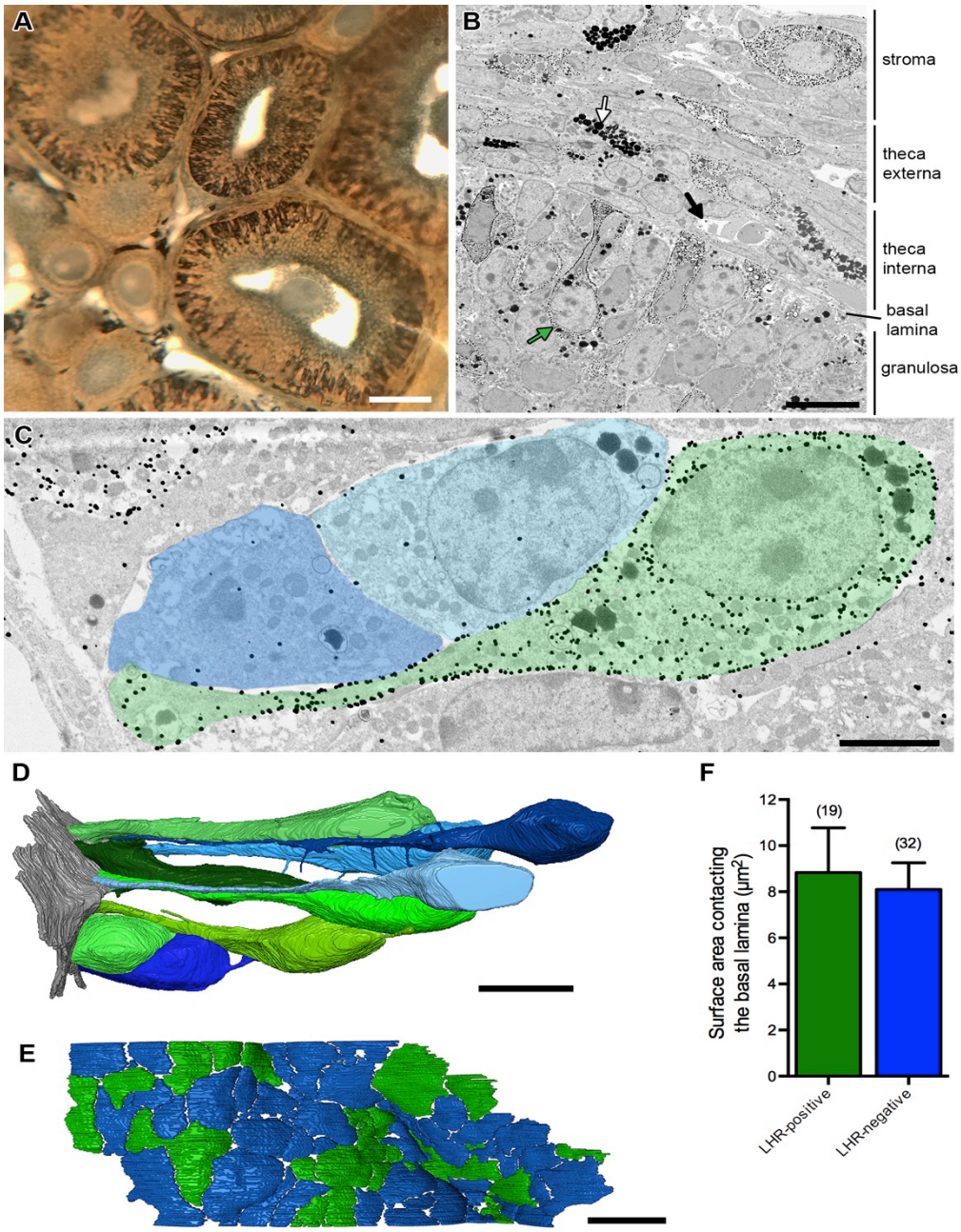

Figure 5. Electron microscopic imaging of the shapes and basal lamina contacts of mural granulosa cells that do or do not express the LHR. (A) Light microscope view of a 55 μm thick vibratome slice of an ovary from an immature HA-LHR mouse that was injected 44 hours previously with eCG. The slice was permeabilized with 0.1% Triton X100, labeled with an HA tag antibody and immunogold, and flat-embedded in Epon resin. The black staining is the enhanced gold (LHR label). The diffuse gray staining around the antrum and in the oocyte is background labeling. (B) A 500 nm section of the vibratome slice, imaged by scanning electron microscopy. The small black dots indicate gold-labeling of the LHR (green arrow). The large black dots indicate lipid drops (white arrow) and do not indicate gold labeling. The black arrow points to a blood vessel adjacent to the basal lamina. (C) A 65 nm section from a series of 225 sections. LHR-expressing cells (green) were identified by the presence of gold labeling in the plasma membrane, nuclear envelope, and cytoplasm, throughout several serial sections. Two non-LHR-expressing cells, identified by the lack of gold labeling, are shown in blue. Basal lamina contact sites are visible on the left side of the

figure. (D) Reconstruction of 9 cells traced from serial sections, with LHR-expressing cells shown in shades of green and non-LHR-expressing cells shown in shades of blue. The basal lamina surface is shown in gray on the left. Video 3 shows this reconstruction from multiple angles. (E) Reconstruction showing contact sites with the basal lamina for 71 cells. Contacts with LHR-expressing cells are shown in green and contacts with non-LHR-expressing cells are shown in blue. F) Average surface area of the contact site made by LHR-expressing cells and non LHR-expressing cells with the basal lamina. Bars show mean ± SEM. Means were compared using an unpaired t-test; $p > 0.05$. Numbers indicate the number of cell contacts measured for each group. Scale bars indicate 100 µm for A, 10 µm for B, 3 µm for C, 10 µm for D, and 5 µm for E.

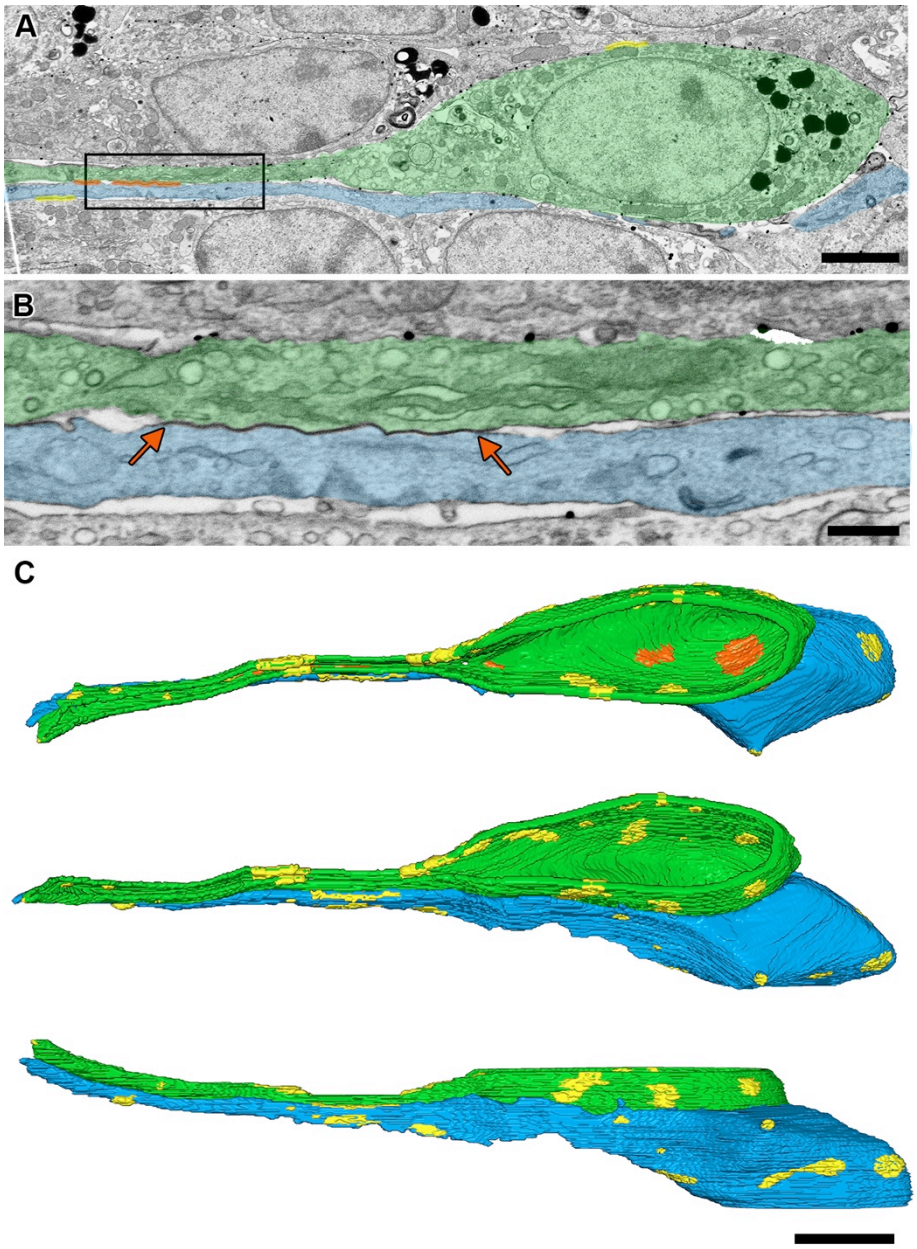

Figure 6. Gap junctions between LHR-expressing and non-LHR-expressing cells. (A) Gap junction contacts of an LHR-expressing cell (green) and a non-LHR-expressing cell (blue) are highlighted in orange. Yellow indicates gap junctions with other cells. The box in A indicates the area enlarged in B. (B) A gap junction (orange arrows)

between the 2 cells highlighted in A. (C) Reconstruction of the 2 cells in A, showing 3 angles of view from video 4. Color coding of gap junctions as for A. Scale bars indicate 3 μm for A, 500 nm for B, and 5 μm for C.

Localization of NPR2 throughout the granulosa cell compartment, with a higher concentration in the cumulus region

To investigate the distribution of NPR2 protein in the follicle, we examined frozen sections of formaldehyde-fixed ovaries from HA-NPR2-expressing mice by labelling sections with an HA-tag antibody (32). Consistent with previous reports of NPR2 mRNA localization (4,21), NPR2 protein was present throughout the granulosa region of the follicle, absent in the oocyte, and most concentrated in the cumulus cells (Fig. 7A; compare with the wildtype follicle in Fig. 7B). Within the outer mural region, all cells contained NPR2 protein, in approximately equal amounts; the heterogeneity seen for the LHR was not evident (Fig. 7C; compare with the wildtype follicle in Fig. 7D). Within the inner mural region, the cells closest to the antrum contained more NPR2 (Fig. 7A,C), again consistent with previous reports of mRNA distribution (4,21).

Measurements of HA-NPR2 fluorescence intensity indicated that the average concentration of NPR2 in the outer mural region is about 30% of that in the cumulus cells (Fig. 7E). On average, the concentration of NPR2 in the inner mural region is about 50% of that in the cumulus cells (Fig. 7E). We then estimated the volume of each of the three regions, by counting the number of cell nuclei in each region of an equatorial section, and assuming that the volumes of individual cells in each region were similar. This procedure yielded the graph shown in Fig. 7F. Multiplying the values in Fig. 7E by those in Fig. 7F yielded the graph shown in Fig. 7G, which indicates that about 40% of the total NPR2 is in the outer mural cells, about 44% in the inner mural cells, and about 16% in the cumulus cells.

Determination of the percentage of the total NPR2 that is in LHR-expressing cells

Based on the data from Fig. 7G showing that about 40% of the total NPR2 protein is in the outer mural cells, and the data from Fig. 4C showing that the percentage of outer mural cells that express the LHR is about 13-48%, we concluded that only about 5-19% of the total follicle NPR2 protein is in cells that also express the LHR (40% x 13-48%). Ideally different epitope tags would have been used for the LHR and NPR2, allowing localization of the 2 proteins in the same individual cells. However, as discussed above, only the HA epitope tag provided specific labeling.

This calculation of the percentage of the total NPR2 protein that is in LHR-expressing cells relies on our findings that essentially all of the LHR is in the outer mural cells (Figs 3,4), and that the NPR2 concentration is similar in all of the outer mural cells (Fig. 7C). Assuming that NPR2 in all of these cells is equally active, our findings indicate that to explain how LH signaling decreases NPR2 activity in the follicle to 50% of the basal level (10,11), signaling by the LHR would need to inactivate NPR2 not only in cells that co-express the LHR, but also in neighboring cells that do not express the LHR.

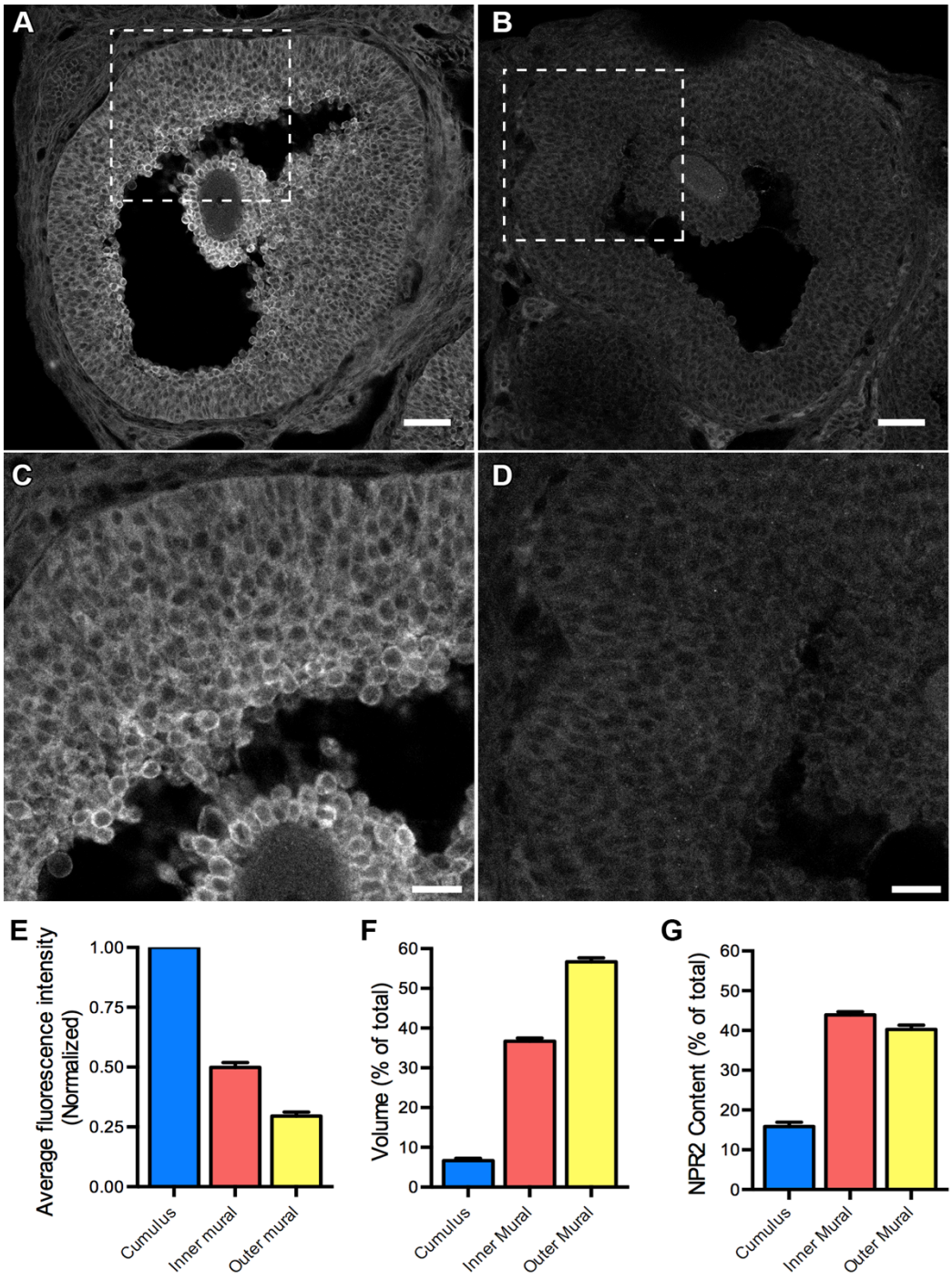

Figure 7. NPR2 distribution in preovulatory follicles. (A-D) Preovulatory follicles in ovaries from HA-NPR2 (A,C) or wildtype (B,D) mice. All sections were labeled with an HA tag antibody. HA-NPR2 and wildtype sections were labeled and imaged using identical conditions. Single optical sections are shown. Scale bars indicate 50 µm for A and B, 20 µm for C and D. (E) Average fluorescence intensities for each region of HA-NPR2 follicles, after subtraction of background determined from measurements of wildtype follicles. Values are normalized to cumulus intensity. Data are from 33 follicles from 5 HA-NPR2 mice, and 22 follicles from 4 wildtype mice. (F) Relative volumes of cumulus, inner mural, and outer mural regions, determined by counting the number of cells in each region in equatorial sections. Cell counts were used to estimate the relative volumes of the three regions, assuming

volumes are proportional to the number of cells. Data are from 10 follicles from 4 mice. (G) Percentage of total NPR2 content in cumulus, inner mural, and outer mural. Values were determined by multiplying numbers from E and F and are expressed as a percentage of the total NPR2 content. Graphs show mean ± SEM.

Attenuation of the LH-induced cGMP decrease in the mural granulosa cells by an inhibitor of gap junction permeability

One of the possible mechanisms that could convey the NPR2-inactivating signal from a cell expressing the LHR to a non-LHR expressing neighbor cell is diffusion of a small molecule through gap junctions. To investigate this possibility, we used mice expressing an optical cGMP sensor (cGi500) to measure the LH-induced cGMP decrease in the outer mural granulosa cells of isolated follicles, and incubated the follicles with CBX to decrease gap junction permeability.

In the presence of CBX, the LH-induced cGMP decrease in the outer mural cells was partially attenuated (Fig. 8A,B). CBX has been previously shown to effectively inhibit connexin 37 junctions between the oocyte and cumulus cells (6). Tests of gap junction permeability, using fluorescence recovery after photobleaching (FRAP), confirmed that under the conditions used, CBX completely blocked diffusion of a fluorescent tracer (Alexa 488) through the connexin 43 junctions between the mural granulosa cells (Fig. 8C,D). These findings indicate that gap junctions are a mediator of the LH-induced cGMP decrease in the outer mural granulosa cells, consistent with this mechanism contributing to inactivation of NPR2 in cells other than those expressing the LHR.

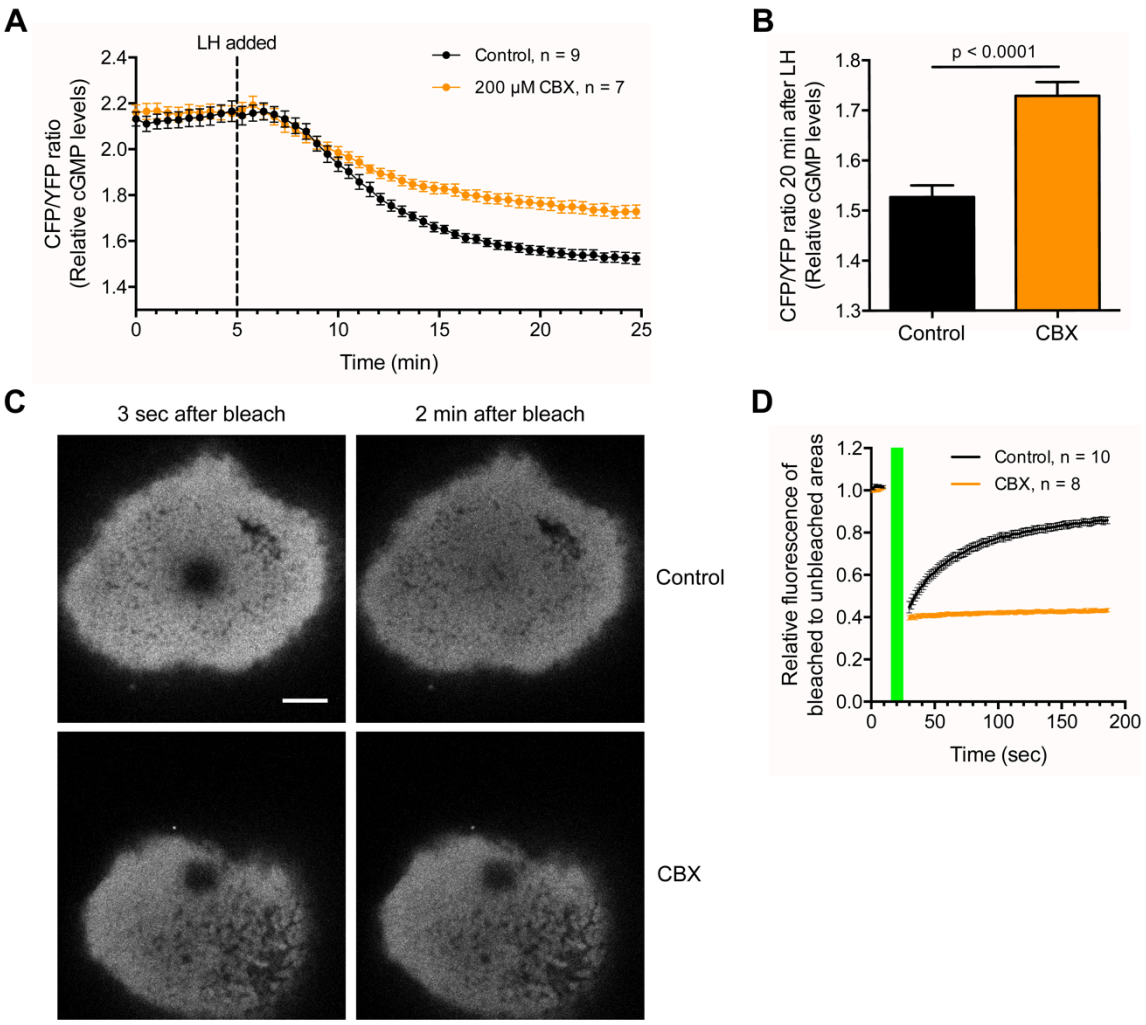

Figure 8. Attenuation of the LH-induced cGMP decrease in the outer mural granulosa cells by inhibition of gap junctions. (A) Follicles expressing the cGi500 FRET sensor for cGMP were preincubated for 2 hours with or without 200 µM CBX and then imaged every 30 seconds by confocal microscopy, before and after addition of 10 nM LH. A decrease in cGi500 CFP/YFP emission ratio indicates a decrease in cGMP. The graph shows CFP/YFP ratios as a function of time after LH perfusion, mean ± SEM for the indicated number of follicles. (B) CFP/YFP ratios, mean ± SEM, at 20 min after perfusion of 10 nM LH, with or without CBX preincubation (data from A). The bars indicate the average of the final 5 scans of the recordings shown in A. Data were analyzed by an unpaired t-test. (C) CBX effectively blocks gap junction communication, as tested by FRAP in the outer mural granulosa cells of follicles preincubated for 2 hours with or without 200 µM CBX. Alexa-488 was injected into the oocyte within the follicle and was allowed to diffuse through gap junctions into the outer granulosa cells for at least 2 hours prior to CBX treatment (14). Images show a field of outer mural granulosa cells 20 µm deep into the follicle. Images on the left were collected as quickly as possible (~3 sec) after photobleaching; images on the right were obtained 2 min after photobleaching from a series of 100 scans taken every 1.6 sec after the end of photobleaching. Scale bar indicates 50 µm. (D) Quantitation of FRAP in control follicles and follicles preincubated for 2 hours with 200 µM CBX. To correct for absolute differences in fluorescence intensity and mild photobleaching during image collection, the fluorescence of the photobleached area was normalized to a non-bleached region of similar initial intensity. The green bar represents the period of photobleaching, with a series of 6 scans collected every 1.6 sec before bleaching and a series of 100 scans collected every 1.6 sec after bleaching. Data points indicate the mean ± SEM for 10 control and 8 CBX FRAP trials using 2 control and 2 CBX-treated follicles.

Discussion

Immunofluorescence localization of cellular proteins that are expressed at low levels requires the availability of highly specific antibodies, as well as a control sample lacking the antigen. For studies of endogenous proteins in tissues, these requirements can be met by use of mice in which the protein of interest is replaced with an epitope-tagged protein for which specific antibodies to the tag are available (23,24). Wildtype mice lacking the tag provide a negative control. Here we produced mice in which the LHR and the NPR2 guanylyl cyclase were replaced with HA-tagged proteins.

Using these mice, we quantified LHR and NPR2 protein localization in ovarian follicles. Our results are consistent with mRNA and ligand binding localization seen in previous studies, but provide cellular vs tissue level resolution. The results showed that only some of the outer mural granulosa cells express the LHR. Images in previous studies also suggest heterogeneity in LHR distribution in different regions of the outer mural granulosa cells (15-20), but the resolution of these earlier methods was insufficient to detect cellular heterogeneity. By quantifying the distribution of the LHR and NPR2 in different regions of the follicle, we determined that the cells that express the LHR contain less than 20% of the total NPR2 in the follicle.

Our results raise the question of how LHR signaling in a subset of the granulosa cells that contains less than 20% of the total NPR2 protein can account for the measured decrease in NPR2 activity to a level of ~50% of that before LH application (10,11). Our findings support a role for intercellular diffusion of a small molecule through gap junctions in conveying the NPR2-inactivating signal to mural granulosa and cumulus cells that do not express the LH receptor. Other mechanisms may contribute as well, including the release of epidermal growth factor receptor (EGFR) ligands that diffuse extracellularly within the follicle (1,47). Inhibiting EGFR

kinase activity attenuates the LH-induced cGMP decrease to varying degrees with different experimental conditions (1,47), but measurements with the cGi500 FRET sensor showed that preventing EGFR activation has little or no effect on the initial LH-induced decrease in cGMP (14).

A candidate for the small molecule that is generated by LH signaling and diffuses through gap junctions to inactivate NPR2 in adjacent cells is cAMP. A role for cAMP is supported by evidence that elevating cAMP with forskolin mimics the LH-induced cGMP decrease in the follicle (14). Furthermore, LH signaling, via the cAMP-activated protein kinase A, phosphorylates and activates a regulatory subunit of the PPP2 phosphatase in rat granulosa cells (48), and PPP family phosphatase activity is required for NPR2 dephosphorylation in response to LH (11). Our finding that CBX attenuates the LH-induced cGMP decrease in the outer mural granulosa cells is consistent with this model.

Our findings, as well as previous studies of the localization of the LHR and NPR2 (see Introduction) also raise the question of what factors determine the localized expression of these proteins within the tissue. Both stimulatory and inhibitory factors have been identified. One essential factor that stimulates LHR expression is FSH (15,16,41; see Fig. 2C). Although FSH receptors are present throughout the mural and cumulus granulosa cells (18), FSH delivery to the follicle from blood vessels outside of the follicles results in a gradient of FSH within the follicle, with more FSH near the basal lamina (16). This gradient of FSH could contribute to the observed gradient of LHR expression. It is unknown whether FSH receptor expression in the granulosa cells might be heterogeneous on a cellular level. If so, this could contribute to the heterogeneity of LHR expression.

Contact with the extracellular matrix of the basal lamina (41,49) is another factor that stimulates LHR expression. Our findings indicate that this contact is not sufficient for LHR expression. Androgens that are produced by surrounding theca cells also stimulate LHR expression (50,51), and this may be an additional factor that influences the localization of the LHR.

In contrast to these positive factors, oocyte-secreted proteins of the TGF-beta superfamily, growth differentiation factor 9 and bone morphogenetic protein 15, inhibit LHR expression (41,52). These same oocyte-secreted proteins that inhibit LHR expression stimulate NPR2 expression (4), supporting the concept that oocyte-secreted proteins are a cause of higher NPR2 expression and lower LHR expression in granulosa cells nearer to the oocyte. Long cellular processes that extend from the outer granulosa cells (37) could potentially sense a concentration gradient of TGF-beta proteins across the mural granulosa cell layer. In future studies, it will be of interest to investigate the spatial distribution of this gradient.

In future studies of the function of the LHR and NPR2 in ovarian granulosa cells, the HA-tagged LHR and NPR2 mice described here should be useful for determining whether the localization of these proteins changes in response to LH signaling. Previous studies of cultured cells exogenously expressing the LHR indicated that LH binding results in internalization of the receptor, thus prolonging and diversifying the hormonal signal (53,54). However, imaging of LH-induced internalization of the LHR in intact ovaries has not been accomplished. The ability to directly visualize LHR and NPR2 proteins in the ovarian follicle may also facilitate investigation of regulatory factors that determine their localized expression.

In addition to its function in the granulosa cells, the LHR regulates steroid production by ovarian cells outside of the follicle itself (theca/interstitial cells) (55) and by testicular Leydig

cells (56). The LHR is also expressed in the corpus luteum, although its contribution to stimulating progesterone production to support pregnancy in mice is not clearly understood (57). Outside of the ovary, the LHR is expressed in the uterus and oviduct (58), although LHR expression in these tissues is not required for reproduction (59). Outside of the reproductive system, recent evidence indicates that the LHR functions in hematopoietic stem cells (60). Likewise the NPR2 guanylyl cyclase functions in the skeletal, cardiovascular, and nervous systems (61), but its localization is not well characterized. As we have found for ovarian granulosa cells, more precise knowledge of LHR and NPR2 localization obtained using mice with HA-tagged versions of these proteins may contribute to understanding of their function in cell signaling in diverse physiological systems.

Acknowledgments

We thank Deborah Kaback for her help in generating and maintaining the genetically modified mice, and Robert Feil for providing the cyclic GMP sensor mice. We also thank Luisa Lestz, Leia Shuhaibar, and Giulia Vigone for their assistance with experiments, and Daniel Bernard, Raj Duggavathi, John Eppig, Aylin Hanyaloglu, Ilpo Huhtaniemi, Eric Levine, Olga Morozova, Bruce Murphy, Rachael Norris, Lincoln Potter, JoAnne Richards, Adolfo Rivera-Müller, Alexander Sorkin, and Stephen Yeung for advice and helpful discussions.

References

1. Jaffe LA, Egbert JR. Regulation of mammalian oocyte meiosis by intercellular communication within the ovarian follicle. *Ann Rev Physiol.* 2017;**79**(1):237-260.
2. Clarke HJ. Regulation of germ cell development by intercellular signaling in the mammalian ovarian follicle. *Wiley Interdiscip Rev Dev Biol.* 2018;**7**(1).
3. Richards JS, Ascoli M. Endocrine, paracrine, and autocrine signaling pathways that regulate ovulation. *Trends Endocrin Metab.* 2018;**29**(5):313-325.

4. Zhang, M, Su Y-Q, Sugiura K, Xia G, Eppig JJ. Granulosa cell ligand NPPC and its receptor NPR2 maintain meiotic arrest in mouse oocytes. *Science.* 2010;**330**(6002):366-369.
5. Geister KA, Brinkmeier ML, Hsieh M, Faust SM, Karolyi IJ, Perosky JE, Kozloff KM, Conti M, Camper SA. A novel loss-of-function mutation in *Npr2* clarifies primary role in female reproduction and reveals a potential therapy for acromesomelic dysplasia, Maroteaux type. *Human Molecular Genetics*. 2013;**22**(2):345-357.
6. Norris RP, Freudzon M, Mehlmann LM, Cowan AE, Simon AM, Paul DL, Lampe PD, Jaffe LA. Luteinizing hormone causes MAP kinase-dependent phosphorylation and closure of connexin 43 gap junctions in mouse ovarian follicles: one of two paths to meiotic resumption. *Development.* 2008;**135**(19):3229-3238.
7. Norris RP, Ratzan WJ, Freudzon M, Mehlmann LM, Krall J, Movsesian MA, Wang H, Ke H, Nikolaev VO, Jaffe LA. Cyclic GMP from the surrounding somatic cells regulates cyclic AMP and meiosis in the mouse oocyte. *Development.* 2009;**136**(11):1869-1878.
8. Richard S, Baltz JM. Prophase I arrest of mouse oocytes mediated by natriuretic peptide precursor C requires GJA1 (connexin-43) and GJA4 (connexin-37) gap junctions in the antral follicle and cumulus-oocyte complex. *Biol Reprod.* 2014;**90**(6):137.
9. Sánchez F, Lolicato F, Romero S, De Vos M, Van Ranst H, Verheyen G, Anckaert E, Smitz JEJ. An improved IVM method for cumulus-oocyte complexes from small follicles in polycystic ovary syndrome patients enhances oocyte competence and embryo yield. *Hum Reprod.* 2017;**32**(10):2056-2068.
10. Robinson JW, Zhang M, Shuhaibar LC, Norris RP, Geerts A, Wunder F, Eppig JJ, Potter LR, Jaffe LA. Luteinizing hormone reduces the activity of the NPR2 guanylyl cyclase in mouse ovarian follicles, contributing to the cyclic GMP decrease that promotes resumption of meiosis in oocytes. *Dev Biol.* 2012;**366**(2):308-316.
11. Egbert JR, Shuhaibar LC, Edmund AB, Van Helden DA, Robinson JW, Uliasz TF, Baena V, Geerts, A, Wunder, F, Potter LR, Jaffe LA. Dephosphorylation and inactivation of the NPR2 guanylyl cyclase in the granulosa cells contributes to the LH-induced cGMP decrease that causes resumption of meiosis in rat oocytes. *Development*. 2014;**141**(18):3594-3604.
12. Shuhaibar LC, Egbert JR, Edmund AB, Uliasz TF, Dickey DM, Yee SP, Potter LR, Jaffe LA. Dephosphorylation of juxtamembrane serines and threonines of the NPR2 guanylyl cyclase is required for rapid resumption of oocyte meiosis in response to luteinizing hormone. *Develop Biol.* 2016;**409**(1):194-201.
13. Egbert JR, Yee SP, Jaffe LA. Luteinizing hormone signaling phosphorylates and activates the cyclic GMP phosphodiesterase PDE5 in mouse ovarian follicles, contributing an additional component to the hormonally induced decrease in cyclic GMP that reinitiates meiosis. *Develop Biol.* 2018;**435**(1):6-14.
14. Shuhaibar LC, Egbert JR, Norris RP, Lampe PD, Nikolaev VO, Thunemann M, Wen L, Feil R, Jaffe LA. Intercellular signaling via cyclic GMP diffusion through gap junctions in the mouse ovarian follicle. *Proc Natl Acad Sci USA*. 2015;**112**(17):5527-5532.
15. Zeleznik AJ, Midgley AR, Reichert LE. Granulosa cell maturation in the rat: increased binding of human chorionic gonadotropin following treatment with follicle-stimulating hormone. *Endocrinology.* 1974;**95**(3):818-825.
16. Richards JS, Ireland JJ, Rao MC, Bernath GA, Midgley AR, Reichert LE. Ovarian follicular development in the rat: hormone receptor regulation by estradiol, follicle stimulating hormone and luteinizing hormone. *Endocrinology*. 1976;**99**(6):1562-1570.
17. Bortolussi M, Marini G, Dal Lago A. Autoradiographic study of the distribution of LH(HCG) receptors in the ovary of untreated and gonadotrophin-primed immature rats. *Cell Tissue Res.* 1977;**183**(3):329-342.
18. Camp TA, Rahal JO, Mayo KE. Cellular localization and hormonal regulation of follicle-stimulating hormone and luteinizing hormone receptor messenger RNAs in the rat ovary. *Mol Endocrinol*. 1991;**5**(10):1405-1417.
19. Peng X-R, Hsueh AJW, LaPolt PS, Bjersing L, Ny T. Localization of luteinizing hormone receptor messenger ribonucleic acid expression in ovarian follicle cell types during follicle development and ovulation. *Endocrinology.* 1991;**129**(6):3200-3207.
20. Eppig JJ, Wigglesworth K, Pendola F. The mammalian oocyte orchestrates the rate of ovarian follicular development. *Proc Natl Acad Sci USA*. 2002;**99**(5):2890-2894.
21. Zhang M, Su Y-Q, Sugiura K, Wigglesworth K, Xia G, Eppig JJ. Estradiol promotes and maintains cumulus cell

expression of natriuretic peptide receptor 2 (NPR2) and meiotic arrest in mouse oocytes in vitro. *Endocrinology*. 2011;**152**(11):4377-4385.
22. Jo M, Jung ST. Engineering therapeutic antibodies targeting G-protein-coupled receptors. *Experimental Molecular Medicine*. 2016;**48**:e207.
23. Lu R, Li Y, Zhang Y, Chen Y, Shields AD, Winder DG, Angelotti T, Jiao K, Limbird LE, Zhou Y, Wang Q. Epitope-tagged receptor knock-in mice reveal that differential desensitization of a_2-adrenergic responses is because of ligand-selective internalization. *J Biol Chem.* 2009;**284**(19):13233-13243.
24. Rao A, Richards TL, Simmons D, Zahniser NR, Sorkin A. Epitope-tagged dopamine transporter knock-in mice reveal rapid endocytic trafficking and filopodia targeting of the transporter in dopaminergic axons. *FASEB J.* 2012;**26**(5):1921-1933.
25. Rivero-Müller A, Chou YY, Ji I, Lajic S, Hanyaloglu AC, Jonas K, Rahman N, Ji TH, Huhtaniemi I. Rescue of defective G protein–coupled receptor function in vivo by intermolecular cooperation. *Proc Natl Acad Sci USA*. 2010;**107**(5):2319–2324.
26. Hachiya R, Ohashi Y, Kamei Y, Suganami T, Mochizuki H, Mitsui N, Saitoh M, Sakuragi M, Nishimura G, Ohashi H, Hasegawa T, Ogawa Y. Intact kinase homology domain of natriuretic peptide receptor-B Is essential for skeletal development. *J Clin Endocrin Metab.* 2007;**92**(10):4009-4014.
27. Dickey DM, Edmund AB, Otto NM, Chaffee TS, Robinson JW, Potter LR. Catalytically active guanylyl cyclase B requires endoplasmic reticulum-mediated glycosylation, and mutations that inhibit this process cause dwarfism. *J Biol Chem.* 2016;**291**(21):11385-11393.
28. Thunemann M, Wen L, Hillenbrand M, Vachaviolos A, Feil S, Ott T, Han X, Fukumura D, Jain R, Russwurm M, de Wit C, Feil, R. Transgenic mice for cGMP imaging. *Circ Res.* 2013;**113**(4):365-371.
29. Bingel AS, Schwartz NB. Pituitary LH content and reproductive tract changes during the mouse oestrous cycle. *J Reprod Fert.* 1969;**19**(2):215-222.
30. Czieselsky K, Prescott M, Porteous R, Campos P, Clarkson J, Steyn FJ, Campbell RE, Herbison AE. Pulse and surge profiles of luteinizing hormone secretion in the mouse. *Endocrinology.* 2016;**157**(12):4794-4802.
31. Vigone G, Shuhaibar LC, Egbert JR, Uliasz TF, Movsesian MA, Jaffe LA. Multiple cAMP phosphodiesterases act together to prevent premature oocyte meiosis and ovulation. *Endocrinology.* 2018;**159**(5):2142-2152.
32. RRID: AB_1549585, https://antibodyregistry.org/search.php?q=AB_1549585
33. RRID: AB_10719218, https://antibodyregistry.org/search.php?q=AB_10719218
34. RRID: AB_2576217, https://antibodyregistry.org/search.php?q=AB_2576217
35. Schindelin J, Arganda-Carreras I, Frise E, Longair M, Pietzsch T, Preibisch S, Rueden C, Saalfeld S, Schmid B, Tinevez JY, White DJ, Hartenstein V, Eliceiri K, Tomancak P, Cardona A. Fiji: an open-source platform for biological-image analysis. *Nat Methods.* 2012;**9**(7):676-682.
36. RRID: AB_2819209, https://antibodyregistry.org/search.php?q=AB_2819209
37. Baena V, Terasaki M. Three-dimensional organization of transzonal projections and other cytoplasmic extensions in the mouse ovarian follicle. *Sci Rep.* 2019;**9**:1262.
38. Baena V, Schalek RL, Lichtman JW, Terasaki M. Serial-section electron microscopy using automated tape-collecting ultramicrotome (ATUM). *Meth Cell Biol.* 2019;**152**: 41-67.
39. Cardona A, Saalfeld S, Schindelin J, Arganda-Carreras I, Preibisch S, Longair M, Tomancak P, Hartenstein V, Douglas RJ. TrakEM2 software for neural circuit reconstruction. *PLOS ONE.* 2012;**7**:e38011.
40. Russwurm M, Mullershausen F, Friebe A, Jäger R, Russwurm C, Koesling D. Design of fluorescence resonance energy transfer (FRET)-based cGMP indicators: a systematic approach. *Biochem J.* 2007;**407**(1):69-77.
41. Eppig JJ, Wigglesworth K, Pendola F, Hirao Y. Murine oocytes suppress expression of luteinizing hormone receptor messenger ribonucleic acid by granulosa cells. *Biol Reprod*. 1997;**56**(4):976-984.
42. Einhauer A, Jungbauer A. The FLAG^{TM} peptide, a versatile fusion tag for the purification of recombinant proteins. *J Biochem Biophys Meth.* 2001;**49**(1-3):455-465.
43. Fujii Y, Kaneko M, Neyazaki M, Nogi T, Kato Y, Takagi J. PA tag: A versatile protein tagging system using a super high affinity antibody against a dodecapeptide derived from human podoplanin. *Protein Expression and Purification.* 2014;**95**:240–247.

44. Lipner H, Cross NL. Morphology of the membrana granulosa of the ovarian follicle. *Endocrinology*. 1968;**82**(3):638-641.
45. Schroeder AC, Eppig JJ. The developmental capacity of mouse oocytes that matured spontaneously *in vitro* is normal. *Develop Biol.* 1984;**102**(2):493-497.
46. Richards JS, Ren YA, Candelaria N, Adams JE, Rajovic A. Ovarian follicular theca cell recruitment, differentiation, and impact on fertility: 2017 update. *Endocrine Reviews*. 2018;**39**(1):1-20.
47. Liu X, Xie F, Zamah AM, Cao B, Conti M. Multiple pathways mediate luteinizing hormone regulation of cGMP signaling in the mouse ovarian follicle. *Biol Reprod.* 2014;**91**(1):9,1-11.
48. Flynn MP, Maizels ET, Karlsson AB, McAvoy T, Ahn JH, Nairn AC, Hunzicker-Dunn M. Luteinizing hormone receptor activation in ovarian granulosa cells promotes protein kinase A-dependent dephosphorylation of microtubule-associated protein 2D. *Mol Endocrinol.* 2008;**22**(7):1695-1710.
49. Furman A, Rotmensch S, Kohen F, Mashiach S, Amsterdam A. Regulation of rat granulosa cell differentiation by extracellular matrix produced by bovine corneal endothelial cells. *Endocrinol*ogy. 1986;**118**(5):1878-1885.
50. Kawai T, Richards JS, Shimada M. The cell type-specific expression of *Lhcgr* in mouse ovarian cells: evidence for a DNA-demethylation-dependent mechanism. *Endocrinology*. 2018;**159**(5):2062-2074.
51. Candelaria NR, Padmanabhan A, Stossi F, Ljungberg MC, Shelly KE, Pew BK, Solis M, Rossano AM. McAllister JM, Wu S, Richards JS. VCAM1 is induced in ovarian theca and stromal cells in a mouse model of androgen excess. *Endocrinology*. 2019;**160**(6);1377-1393.
52. Sugiura K, Su Y-Q, Diaz F, Pangas SA, Sharma S, Wigglesworth K, O'Brien MJ, Matzuk MM, Shimasaki S, Eppig JJ. Oocyte-derived BMP15 and FGFs cooperate to promote glycolysis in cumulus cells. *Development*. 2007;**134**(14):2593-2603.
53. Jean-Alphonse F, Bowersox S, Chen S, Beard G, Puthenveedu MA, Hanyaloglu AC. Spatially restricted G protein-coupled receptor activity via divergent endocytic compartments. *J Biol Chem.* 2014;**289**(7):3960-3977.
54. Lyga S, Volpe S, Werthmann RC, Götz K, Sungkaworn T, Lohse MJ, Calebiro D. Persistent cAMP signaling by internalized LH receptors in ovarian follicles. *Endocrinology*. 2016;**157**(4):1613-1621.
55. Palaniappan M, Menon KMJ. Luteinizing hormone/human chorionic gonadotropin-mediated activation of mTORC1 signaling is required for androgen synthesis by theca-interstitial cells. *Mol Endocrinol.* 2012;**26**(10):1732-1742.
56. Evaul K, Hammes SR. Cross-talk between G protein-coupled and epidermal growth factor receptors regulates gonadotropin-mediated steroidogenesis in Leydig cells. *J Biol Chem.* 2008;**283**(41):27525-27533.
57. Bachelot A, Beaufaron J, Servel N, Kedzia C, Monget P, Kelly PA, Gibori G, Binart N. Prolactin independent rescue of mouse corpus luteum life span: identification of prolactin and luteinizing hormone target genes. *Am J Physiol Endocrinol Metab*. 2009;**297**(3):E676-E684.
58. Zheng M, Shi H, Segaloff, DL, Van Voorhis BJ. Expression and localization of luteinizing hormone receptor in the female mouse reproductive tract. *Biol Reprod.* 2001;**64**(1):179-187.
59. Pakarainen T, Zhang F-P, Poutanen M, Huhtaniemi I. Fertility in luteinizing hormone receptor-knockout mice after wild-type ovary transplantation demonstrates redundancy of extragonadal luteinizing hormone action. *J Clin Invest.* 2005;**115**(7):1862-1868.
60. Peng YJ, Yu H, Hao X, Dong W, Yin X, Lin M, Zheng J, Zhou BO. Luteinizing hormone signaling restricts hematopoietic stem cell expansion during puberty. *EMBO J.* 2018;**37**(17):e98984.
61. Kuhn M. Molecular physiology of membrane guanylyl cyclase receptors. *Physiol Rev*. 2016;**96**(2):751-804.

Chapter 5

Discussion and future studies

I. Extending our knowledge for the functions of TZPs

In chapter 3, we analyzed the organization of TZPs in large antral follicles. Using serial section electron microscopy, we tracked and reconstructed every projection from the cumulus cells and the oocyte in a 43 µm x 43 µm x 27 µm volume (Baena and Terasaki, 2019). We studied these projections in detail and found that most TZPs do not contact the oocyte surface and that these often branch and make gap junctions with each other. Furthermore, the TZPs that connect to the oocyte are usually contacted on their shaft by oocyte microvilli. Though TZPs have been studied since the 1900s (Hadek, 1965), this study was the first to show their detailed structure, abundance, and the contacts they make with each other and with the oocyte in-vivo.

Below, I outline 3 ideas for addressing some questions about the structure and function of TZPs that remain to be investigated:

Cumulus cell differentiation might be contact-induced

A highly unexpected result from our study is that oocyte microvilli have long contact sites with connected TZPs (Fig. 5.1). With this coupling, the surface area by which cumulus cells and the oocyte contact each other is increased, which could enhance the bi-directional exchange of molecules that occurs between the two cells. For example, gap junctions could form on these sites, increasing the direct communication between the two cells. If gap junctions are present on these sites, they should be observable by serial section electron microscopy using sections cut thinner than were cut in this study, or by electron tomography.

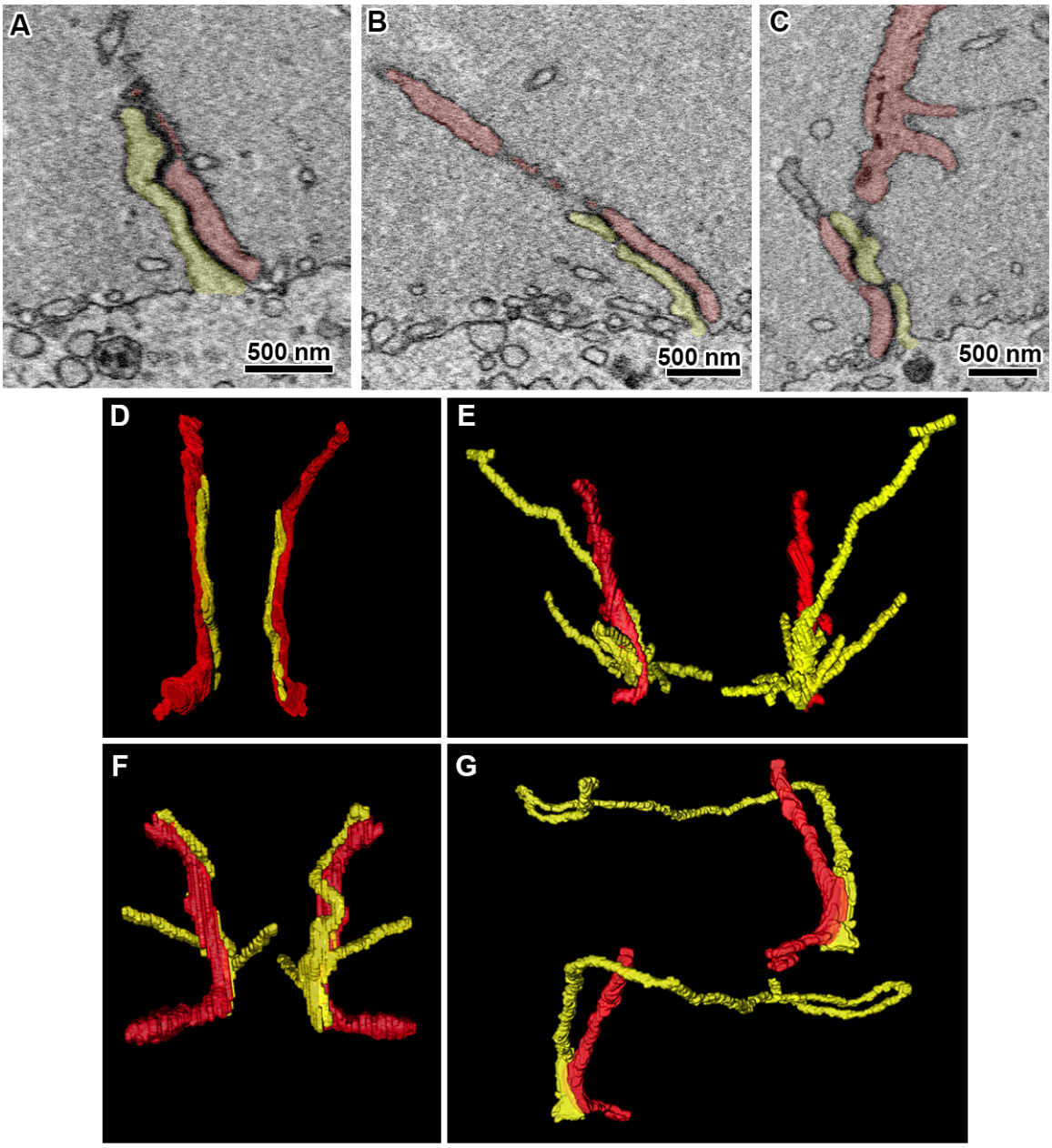

Figure 5.1. Oocyte microvilli closely associate with TZPs. (A-C) Electron micrographs showing examples of the contact sites between TZPs (red) and microvilli (yellow). **(D-G)** Reconstructions of the microvilli-TZP contacts segmented from serial section electron micrographs. Each panel shows one example viewed from two different angles. The oocyte is at the bottom (not shown), the oocyte microvilli are reconstructed in yellow, the cumulus cell body is at the top (not shown), and the TZPs are reconstructed in red.

Another possible function for these sites is that they provide the location for contact-induced signaling to take place, as is seen in the Drosophila male germ cell niche in the testes (Inaba et al., 2015). This study found that the germline stem cells send cytoplasmic protrusions,

called microtubule-based nanotubes (MT-nanotubes) that invaginate into the hub cells. Hub cells provide the growth factor decapentaplegic (DPP), which is known to maintain stem cells as stem cells. The ligand and receptor for this signaling event were localized to the microenvironment of the MT-nanotubes invaginations. If a stem cell divides asymmetrically and one of its daughter cells is dislodged from the hub, or if the protrusions are experimentally abolished from the stem cells, the cells no longer receive the DPP signal and they continue to differentiate down their lineage.

The mammalian follicle resembles the Drosophila male germ cell niche in that oocyte-secreted factors from the transforming growth factor-beta (TGF-β) family such as growth differentiation factor-9 (GDF-9) and bone morphogenic protein-15 (BMP-15) stimulate granulosa cells to take on the cumulus cell phenotype (Eppig et al., 1997; Peng et al., 2013; Yan et al., 2001) and thus undergo cumulus expansion after LH. If unstimulated by oocyte-secreted factors, cumulus cells revert back to their default phenotype of mural granulosa cells. GDF-9 and BMP-15 are thought to freely diffuse outwards from the oocyte and only reach the few cell layers that immediately surround it, confining the cumulus cell phenotype to the cells directly adjacent to the oocyte. In this model, the net diffusion of these molecules must be very short as to not cause cumulus cell differentiation in the granulosa cells lining the antrum. We propose, instead, that it could be controlled by limiting the signaling event to locations where two membranes contact each other. Contact-mediated signaling has been well characterized in Drosophila, and the chick limb bud (Kornberg, 2017; Sanders et al., 2013). In these systems, specialized signaling filopodia termed “cytonemes” participate in the sensing and secreting of morphogens, which ultimately determine the fate of the cell receiving them.

With our results and the recent progress in understanding the Drosophila male germ cell system, we proposed that cumulus cells take-up the GDF-9 and/or BMP-15 signal at the site where the TZPs contact the oocyte. This could take place around the sites of the gap and adherens junctions at the oocyte surface, but also at the sites where the oocyte microvilli elongate along the TZPs. Biologically, this system would be favorable over diffusion as it ensures that only cells that are physically connected to the oocyte, and therefore can ovulate alongside it, are induced to become cumulus cells.

Additional support for this theory comes from observations made in mice deficient for these proteins. GDF-9 homozygous knockout mice show ovaries with follicles arrested at the primary stage, suggesting that GDF-9 is required for the progression of follicle development to the secondary stage (Dong et al., 1996). In contrast to GDF-9, BMP-15 homozygous mutants can develop normally but are subfertile. Interestingly, these ovaries showed occasional follicles with denuded oocytes that had few cumulus cells surrounding them (Fig. 5.2A-B) (Yan et al., 2001). Some follicles in these ovaries failed to show cumulus expansion after treatment with human chorionic gonadotropin hormone (hCG, an analog of LH), and trapped oocytes were sometimes seen in corpora lutea. Additionally, in contrast to wildtype mice, cumulus cells were attached to eggs collected from oviducts of BMP-15 mutants after super-ovulation treatment (Fig. 5.2C-D). Taken together, these results suggest that BMP-15 is required for cumulus cell differentiation and ovulation. The fact that oocytes were found without companion cumulus cells supports our idea that cumulus cells must touch the oocyte in order to acquire their phenotype. There was no mention in this study of whether TZPs were observed in the few cumulus cells that were seen attached to the denuded oocytes within the abnormal follicles. It would be of interest to analyze

these follicles by electron microscopy and determine if TZPs are present in the abnormal follicles.

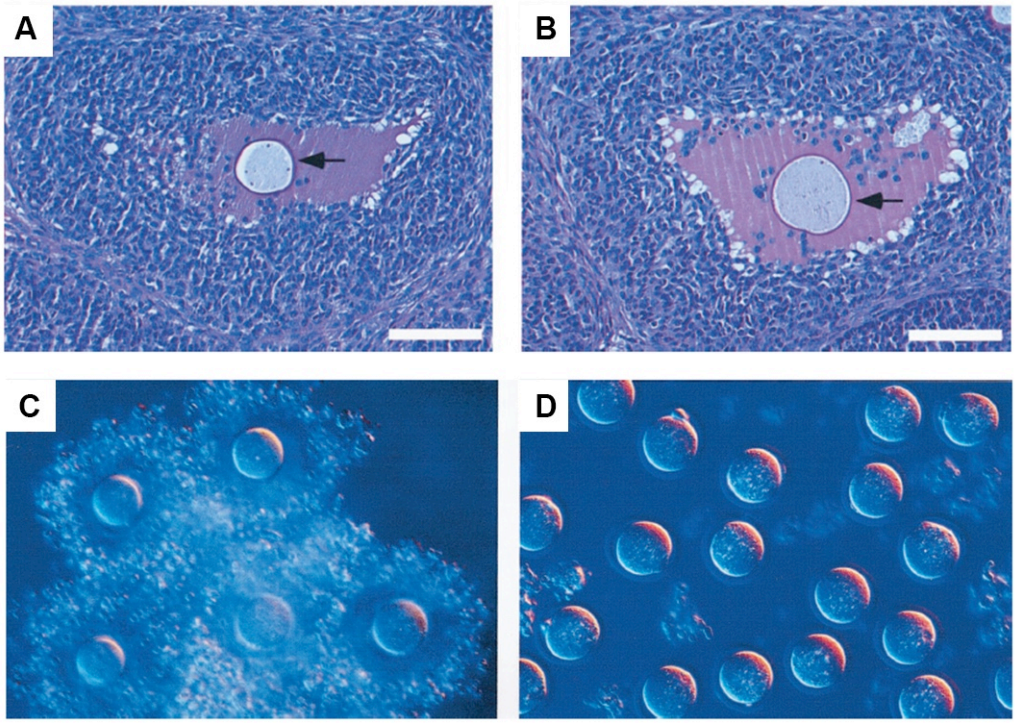

Figure 5.2. Cumulus cells do not adhere to the oocyte in some follicles in BMP15 deficient ovaries. (A-B) Follicles from BMP15+/- (A) and BMP15-/- (B) ovaries showing trapped oocytes lacking cumulus cells after super-ovulation treatment. **(C-D)** Eggs isolated from oviducts of GDF9 +/- (C) and BMP15-/- GDF9 +/- (D) mutant mice after ovulation. Eggs from the BMP15 deficient mice had loosely attached cumulus cells that easily fell off the oocytes. Scale bars: 100 μm. Adapted from Yan et al., 2001.

To further investigate the possibility of contact-mediated differentiation, it would be interesting to localize the receptors for the GDF-9/BMP-15 signal at high resolution in normally functioning follicles. The receptors for this signal in granulosa cells have been found to be the type 1 kinase receptor ALK4/5/7, the type 2 receptor BMPR2, and a co-receptor ALK6, all of which act together to induce the activation of downstream SMAD2/3 pathways (Peng et al., 2013; Vitt et al., 2002). We are currently beginning these experiments. The BMPR2 gene was coupled to an HA epitope tag, as we did for LHR and NPR2 in chapter 4 of this dissertation.

Using commercially available HA antibodies, we have been able to localize BMPR2 in the follicle by immunofluorescence (Fig. 5.3), and are now attempting to localize it by immunogold. If the signal is seen localized to the TZP-oocyte/TZP-microvilli junction, it would be an encouraging sign to continue pursuing the idea that cumulus cell differentiation is contact-mediated. The type 1 receptor should also be labeled in similar ways using a different epitope tag to allow for co-localization of the two receptors. A good candidate for this approach is to use the peroxidase APEX2 tag. This tag can be coupled to the gene of interest and when expressed in tissue, it catalyzes the formation of precipitates in the presence of 3,3'-diaminobenzidine (DAB) and hydrogen peroxide (Martell et al., 2017; Lam et al., 2015), which is visible by light and electron microscopy.

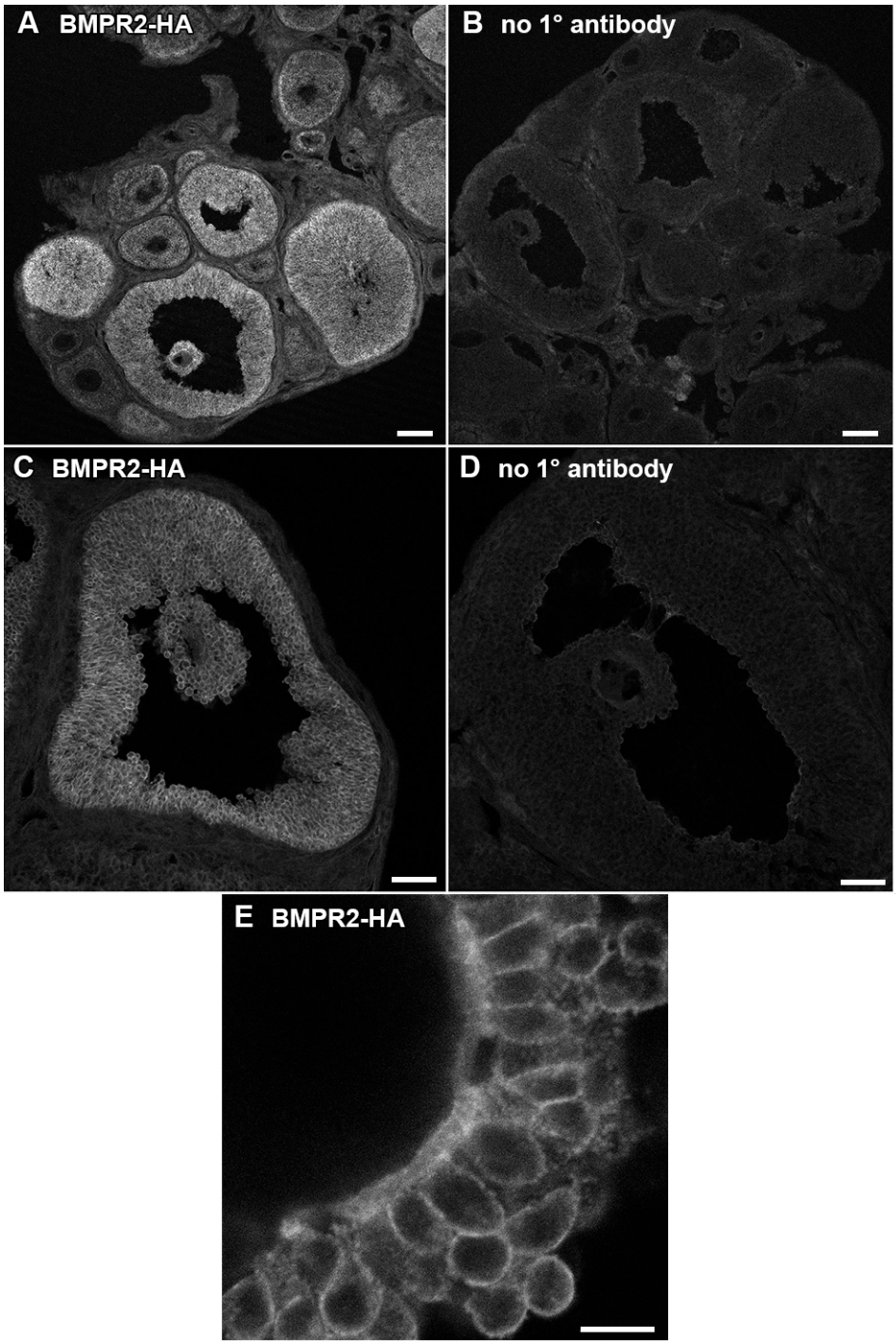

Figure 5.3. Immunofluorescence of HA-tagged BMPR2 in preovulatory follicles. (A, C, E) The BMPR2-HA was labeled using a primary antibody against HA (as described in Chapter 4). **(B, D)** The primary antibody incubation was omitted to determine background fluorescence. Ovaries were acquired from 26 day-old mice injected with pregnant mare serum gonadotropin hormone (PMSG, an FSH analog) 48 hours before euthanasia. The BMPR2-HA is seen in all the mural granulosa and cumulus cells (E) at equal levels within follicles. The levels of BMPR2 are higher in larger follicles. Scale bars: (A, B) 100 μm, (C, D) 50 μm, (E) 10 μm.

Study the direct transport of large cargo between TZPs and the oocyte

It has been suggested that the junction between TZPs and the oocyte may function as a "gametic synapse" (Macaulay et al., 2014), not only allowing the passage of small molecules through gap junctions but also the transfer of large cargo such as mRNA in vesicles (Fig. 5.4). These mRNAs may be required for the reinitiation of transcription during early embryonic development and is thus a key subject to study. This idea can be further investigated by studying TZPs with high-resolution three-dimensional electron microscopy but with a crucial variation in the way in which the follicle is preserved before processing for electron microscopy (as compared to our studies in chapter 3): in order to identify vesicle transport, the follicle should be frozen by high-pressure freezing and further processed for heavy metal staining and dehydration under controlled temperatures (known as freeze substitution) (McDonald, 1999). In addition to preserving morphology better, the high-pressure freezing is much faster than chemical fixation and is required to capture synaptic events (Dahl and Staehelin, 1989; Kellenberger et al, 1992).

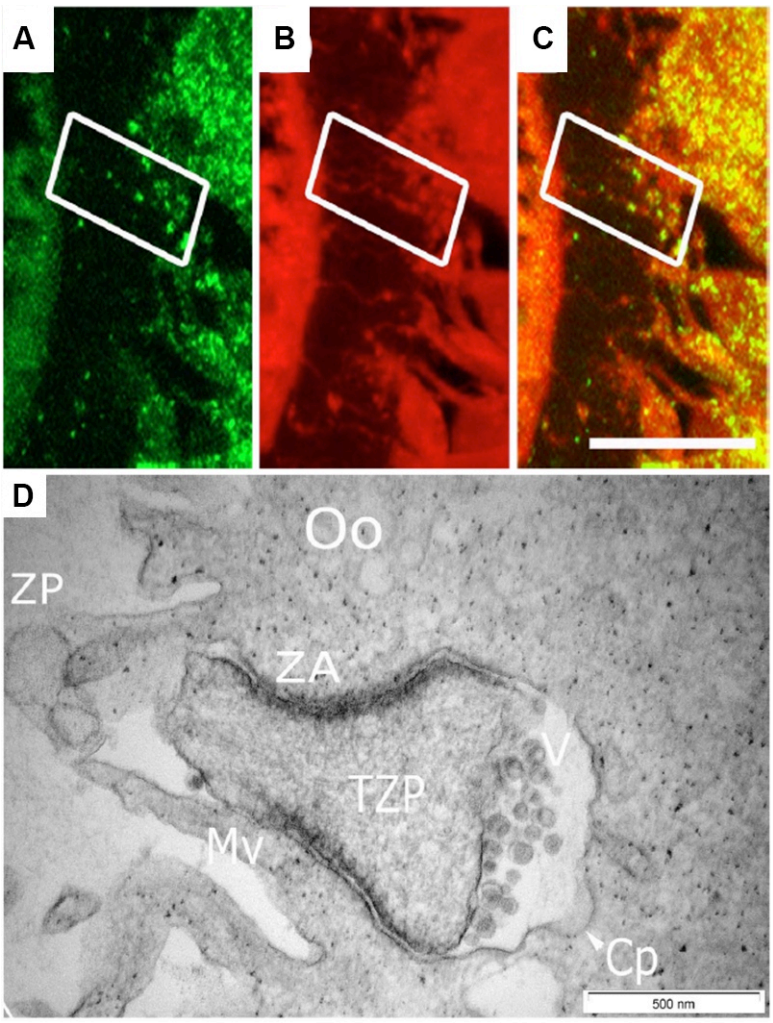

Figure 5.4. TZPs transfer RNA from cumulus cells to the oocyte. (A) Immunofluorescence labeling of poly-A-binding protein, confirming the presence of mRNA in TZPs. **(B)** Membranes of TZPs labeled with FM 4-64. **(C)** Overlay of A and B. **(D)** Electron micrograph showing the end of a TZP. Vesicles are seen on the space between the TZP and the oocyte. These vesicles are suggested to carry the mRNA across the two cell types. ZP, zona pellucida. Oo, oocyte. ZA, zonula adherens-like junction. TZP, transzonal projection. Mv, oocyte microvilli. Cp, coated pit. Scale bars: (A-C) 20 µm, (D) 500 nm. Adapted from Macaulay et al., 2014.

Current methods for high-pressure freezing can achieve optimal freezing for ~200 µm in thickness (McDonald, 1999). This would not preserve TZPs, cumulus cells, and the oocyte in antral or preovulatory follicles properly, as these structures are buried in the center of the ~400 µm diameter follicle. However, different approaches can be taken to overcome this challenge. Small follicles (up to 200 µm in diameter) can be dissected from the ovary and then frozen. Follicles of ~200 µm in diameter are typically at the preantral stage of folliculogenesis and are

expected to have numerous TZPs (Griffin et al., 2006; El-Hayek et al., 2018). A time course of TZP and zona pellucida development can be acquired if follicles of progressively smaller size are frozen in this way. For follicles larger than 200 μm, such as antral and preovulatory, the cumulus-oocyte complex can be micro-dissected with fine needles before freezing, a technique commonly done in the Jaffe and Terasaki laboratories.

Functions for two types of TZPs

Our studies showed that there are two types of TZPs, those connected to the oocyte (~22% of total) and those that are free-ended (~78% of total). Other studies have also identified two types of TZPs by the main component of their cytoskeleton being either actin or tubulin, as seen by fluorescence microscopy (El-Hayek et al., 2018) (Fig. 1.3A-B). Our data shows that connected TZPs are on average longer, thicker, and more likely to have cytoplasmic components such as organelles inside them, leading us to suggest that connected TZPs are tubulin-based while free-ended TZPs are actin-based. Though we were not able to identify microtubules in our datasets, it should be possible to label microtubules with immunogold methods such as the one described in chapter 4. This would allow for the merging of valuable information acquired from fluorescence/molecular studies with that acquired from structural electron microscopy studies, providing a great leap forward in our understanding of these important structures.

II. Investigating the heterogeneity of LHR expression

In Chapter 4, we described and quantified the expression of LHR and NPR2 by creating mice in which the endogenous LHR and the NPR2 proteins were replaced with HA-tagged versions (Baena et al., 2020). Using antibodies against HA, we localized these proteins within whole ovaries at cellular resolution (Fig. 5.5). Our results showed that LHR is expressed in a subset of outer mural granulosa cells whereas NPR2 is present throughout all the granulosa cells. Quantitation of these results indicated that less than 20% of the NPR2 is present in the cells that also express LHR, meaning that only 20% of NPR2 would be directly inactivated by LHR signaling. This is discussed in detail in chapter 4. Below, I discuss a different question that arises from this study.

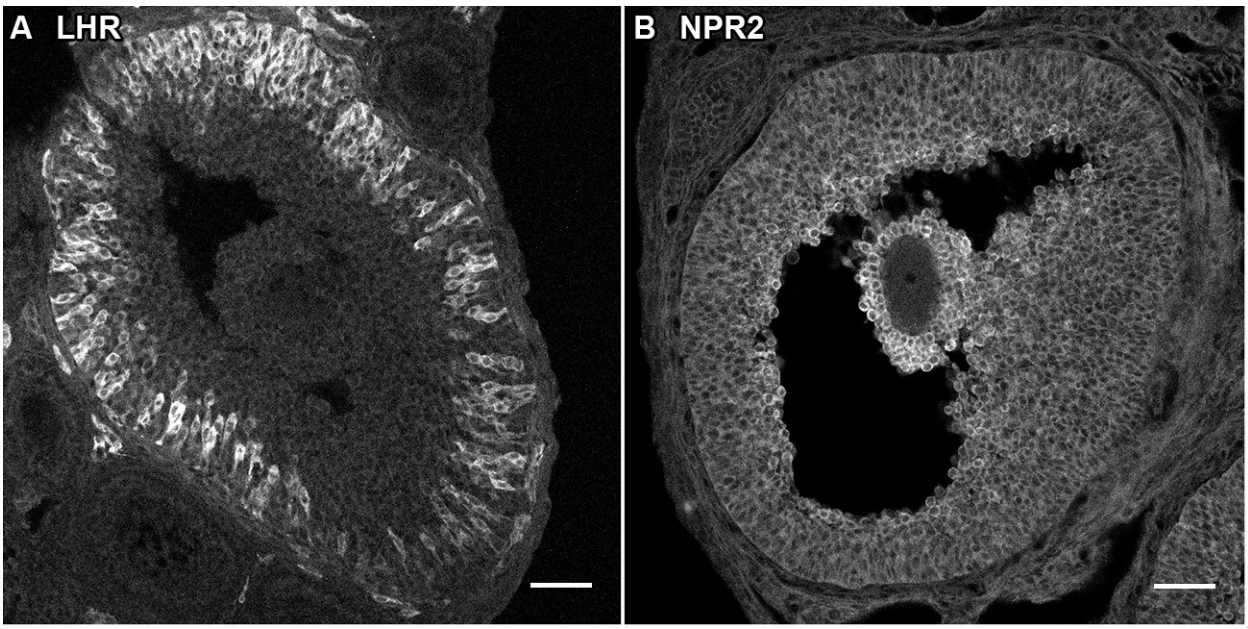

Figure 5.5. Immunofluorescence of HA-tagged LHR and NPR2 in preovulatory follicles. (A) HA-LHR is expressed by preovulatory follicles after treatment with PMSG (FSH analog). Within preovulatory follicles, it is only expressed by some theca cells, and some outer mural granulosa cells. **(B)** HA-NPR2 is expressed by all the gramulosa cells within the follicle, with a higher concentration in cumulus cells and the mural granulosa cells lining the antrum. About 20% of the total NPR2 in the follicle is in the same cells that express LHR (see chapter 4). Scale bars: 50 μm.

What factors influence the heterogeneity of expression of LHR in preovulatory follicles? As explained in the introduction, studies conducted in-vivo and in-vitro have indicated that FSH and components of the basal lamina promote the expression of LHR in granulosa cells (Eppig et al., 1997; Camp et al., 1991) (Fig. 1.6).

Our studies confirmed that FSH induces the expression of LHR. We also found that all LHR-expressing cells, except for a few rare exceptions, were connected to the basal lamina, but not every cell connected to the basal lamina expressed LHR. However, our studies did not provide clues to which factors influence the heterogeneous expression of LHR. For example, we did not see a correlation of LHR expression with the location of blood vessels outside of the follicle, on which FSH is delivered. There was no difference in the average size of the surface area contacting the basal lamina between LHR-positive and LHR-negative cells. And, there was no obvious difference in the ultrastructural organization between LHR-positive and LHR-negative cells as seen by serial section electron microscopy.

It has been shown that FSH promotes the growth of follicles of all sizes (Hardy et al., 2017), however, at the preantral stage, follicles become increasingly dependent on FSH not only for growth but also for survival (Hunzicker-Dunn and Maizels, 2006; Chun et al., 1996; Chu et al., 2018), and the transition from the preantral to antral stage is strictly dependent on FSH (Dierich et al., 1998). Interestingly, as follicles become more dependent on FSH, they also begin to grow more heterogenously. Batches of equally sized primary follicles cultured together in the presence of FSH start their growth at a similar rate, but as they become larger, the growth rates among them start to differ (Fig. 5.6) (Hardy et al., 2017). These results suggest that FSHR expression might vary among cohorts of follicles, which leads me to suggest that its expression might also vary at the cellular level within individual follicles and is the main factor influencing

the heterogeneous expression of LHR. If FSHR expression is heterogeneous, this could be observed directly by creating mice with epitope-tagged FSHR, as we did for LHR and NPR2.

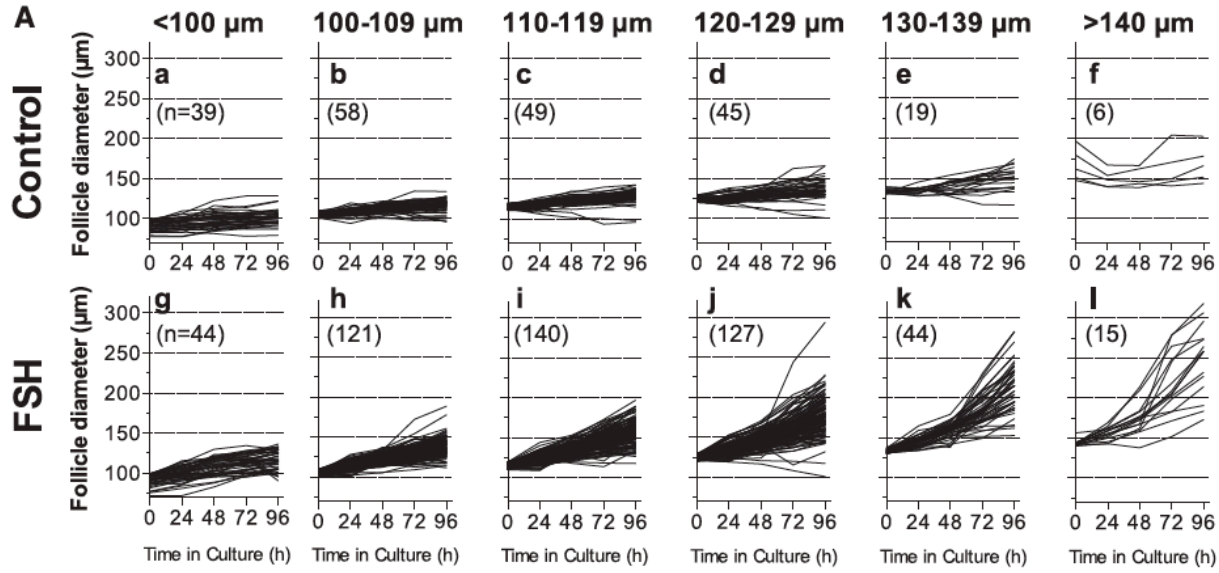

Figure 5.6. Increased heterogeneity of follicle growth in the presence of FSH. (A) Growth rates of follicles cultured in the presence and absence of FSH for 96 hours. Follicles were grouped by size at time 0 (a-l). The number in parenthesis is the number of follicles per group. As the follicles get larger, they grow more heterogeneously in the presence of FSH (j-l). Reproduced from Hardy et al., 2017.

How does a larger follicle influence the levels of FSHR expression in the cells within it? One idea is that with every mitotic cell division, individual granulosa cells increase their expression of FSHR. In other words, the more a cell divides, the more FSHR it expresses. If there is heterogeneity in the frequency of mitosis among granulosa cells, it could be observed by imaging live preantral follicles for prolonged periods of time in the presence of FSH. Individual granulosa cells can then be tracked and the frequency of cell divisions can be acquired (Harder et al., 2009; McDole et al., 2018).

It is possible that granulosa cells must reach a threshold of FSHR activation before they can express LHR. For this theory, I assume that when a follicle reaches the preovulatory stage, its granulosa cells will show the greatest heterogeneity in the expression of FSHR. The cells that

express more FSHR are more sensitive to FSH than their neighbors and other granulosa cells in smaller follicles, and can overcome the threshold of FSHR activation, leading them to express LHR. An additional level of control may be imposed by the basal lamina. In this way, inner mural granulosa cells would not express LHR even if they have high levels of FSHR.

This idea could be tested by culturing isolated follicles with different concentrations of FSH, and then conducting localization studies of HA-LHR on the follicles. High concentrations of FSH might allow granulosa cells that do not have as much FSHR to still reach the threshold of receptor activation and thus LHR would be expressed more homogenously. If the expression pattern does not change, it might indicate that there are at least two subtypes of outer mural granulosa cells, which are different from each other even before the FSH-induced expression of LHR. Single cell RNA sequencing would provide valuable information on the differences in transcription between them (Hwang et al., 2018).

In our studies, LHR expression was induced by injecting pre-pubertal mice with pregnant mare serum gonadotropin (PMSG), a commonly used agonist of the FSHR. We also investigated the expression of LHR in naturally cycling adult females. Follicles acquired with either methodology showed similar patters of heterogeneous expression of LHR, suggesting that the concentration of PMSG used in our study is representative of the natural concentration of FSH in-vivo. However, different concentrations of PMSG (or FSH) could be injected to test the idea mentioned above in an in-vivo model.

LHR expression could also be controlled temporally. As FSH begins to rise at the beginning of the reproductive cycle, the super-sensitive cells of the preovulatory follicle that express the most FSHR would be the first to respond to it. FSH would induce LHR activation in these cells and it could additionally induce them to send a signal to neighboring cells that inhibits

the expression of LHR in them. In this case, even though FSH continues to rise as the reproductive cycle progresses, LHR would only be expressed by the cells that first responded to FSH.

FSHR is a G-protein coupled receptor that induces a wide variety of functions through the cAMP-activated PKA signaling pathway (Jiang et al., 2014; Hunzicker-Dunn and Maizels, 2006). Inhibitors of PKA inhibit the FSH-induced growth of follicles (Hardy et al., 2017). The FSH-induced expression of LHR is thought to be modulated by ERK and Egr-1 signaling downstream of PKA, though this is not fully understood (Yoshino et al., 2002; Russell et al., 2003). There is good in-vitro evidence that shows that LHR expression is inhibited by oocyte-secreted factors. When oocyte-conditioned media or whole oocytes are added to granulosa cell cultures, LHR expression is inhibited, even in the presence of FSH and components of the basal lamina (Eppig et al., 1997) (Fig. 1.6). Discovering the molecular mechanisms for how oocyte-secreted factors inhibit the expression of LHR may give insights to the factors that influence the heterogeneity of LHR expression.

The systems that allow FSH and the oocyte to control the expression of LHR could have evolved to provide a mechanism that prevents follicles from becoming overly sensitive to LH, and thus avoid a premature response to LH at inappropriate times in the cycle. By having a molecular and/or temporal control for the expression of LHR, the premature response of follicles to small spikes of LH could be avoided. Elucidating the mechanisms that control LHR expression is thus crucial for our understanding of female fertility and human reproduction.

References

Albertini, D.F., Rider, V., 1994. Patterns of intercellular connectivity in the mammalian cumulus-oocyte complex. Microsc. Res. Tech. 27, 125–133. https://doi.org/10.1002/jemt.1070270206

Anderson, E., Albertini, D.F., 1976. Gap junctions between the oocyte and companion follicle cells in the mammalian ovary. The Journal of Cell Biology 71, 680–686. https://doi.org/10.1083/jcb.71.2.680

Bächler, M., Menshykau, D., De Geyter, C., Iber, D., 2014. Species-specific differences in follicular antral sizes result from diffusion-based limitations on the thickness of the granulosa cell layer. Mol. Hum. Reprod. 20, 208–221. https://doi.org/10.1093/molehr/gat078

Baena, V., Owen, C.M., Uliasz, T.F., Lowther, K.M., Yee, S.-P., Terasaki, M., Egbert, J., Jaffe, L.A., 2020. Cellular heterogeneity of the LH receptor and its significance for cyclic GMP signaling in mouse preovulatory follicles. bioRxiv 2020.02.06.937995. https://doi.org/10.1101/2020.02.06.937995

Baena, V., Schalek, R.L., Lichtman, J.W., Terasaki, M., 2019. Chapter 3 - Serial-section electron microscopy using automated tape-collecting ultramicrotome (ATUM), in: Müller-Reichert, T., Pigino, G. (Eds.), Methods in Cell Biology, Three-Dimensional Electron Microscopy. Academic Press, pp. 41–67. https://doi.org/10.1016/bs.mcb.2019.04.004

Baena, V., Terasaki, M., 2019. Three-dimensional organization of transzonal projections and other cytoplasmic extensions in the mouse ovarian follicle. Scientific Reports 9, 1262. https://doi.org/10.1038/s41598-018-37766-2

Bellin, M.E., Lenz, R.W., Steadman, L.E., Ax, R.L., 1983. Proteoglycan production by bovine granulosa cells in vitro occurs in response to fsh. Mol. Cell. Endocrinol. 29, 51–65. https://doi.org/10.1016/0303-7207(83)90004-7

Bortolussi, M., Marini, G., Lago, A.D., 1977. Autoradiographic study of the distribution of LH(HCG) receptors in the ovary of untreated and gonadotrophin-primed immature rats. Cell Tissue Res. 183, 329–342. https://doi.org/10.1007/BF00220640

Bortolussi, M., Marini, G., Reolon, M.L., 1979. A histochemical study of the binding of 125I-HCG to the rat ovary throughout the estrous cycle. Cell Tissue Res. 197, 213–226.

Bromfield, J.J., Piersanti, R.L., 2019. Chapter 10 - Mammalian Oogenesis: The Fragile Foundation of the Next Generation, in: Leung, P.C.K., Adashi, E.Y. (Eds.), The Ovary (Third Edition). Academic Press, pp. 157–164. https://doi.org/10.1016/B978-0-12-813209-8.00010-8

Bruzzone, R., White, T.W., Paul, D.L., 1997. Connections with connexins: the molecular basis of direct intercellular signaling, in: Christen, P., Hofmann, E. (Eds.), EJB Reviews 1996, EJB Reviews. Springer, Berlin, Heidelberg, pp. 135–161. https://doi.org/10.1007/978-3-642-60659-5_8

Camp, T.A., Rahal, J.O., Mayo, K.E., 1991. Cellular Localization and Hormonal Regulation of Follicle-Stimulating Hormone and Luteinizing Hormone Receptor Messenger RNAs in the Rat Ovary. Mol Endocrinol 5, 1405–1417. https://doi.org/10.1210/mend-5-10-1405

Chu, Y.-L., Xu, Y.-R., Yang, W.-X., Sun, Y., 2018. The role of FSH and TGF-β superfamily in follicle atresia. Aging (Albany NY) 10, 305–321. https://doi.org/10.18632/aging.101391

Chun, S.Y., Eisenhauer, K.M., Minami, S., Billig, H., Perlas, E., Hsueh, A.J., 1996. Hormonal regulation of apoptosis in early antral follicles: follicle-stimulating hormone as a major survival factor. Endocrinology 137, 1447–1456. https://doi.org/10.1210/endo.137.4.8625923

Clarke, H.G., Hope, S.A., Byers, S., Rodgers, R.J., 2006. Formation of ovarian follicular fluid may be due to the osmotic potential of large glycosaminoglycans and proteoglycans. Reproduction 132, 119–131. https://doi.org/10.1530/rep.1.00960

Clarke, H.J., 2018. History, origin, and function of transzonal projections: the bridges of communication between the oocyte and its environment. Animal Reproduction 15, 215–223. https://doi.org/10.21451/1984-3143-AR2018-0061

Conti, M., Hsieh, M., Zamah, A.M., Oh, J.S., 2012. Novel signaling mechanisms in the ovary during oocyte maturation and ovulation. Mol. Cell. Endocrinol. 356, 65–73. https://doi.org/10.1016/j.mce.2011.11.002

Dahl, R., Staehelin, L.A., 1989. High-pressure freezing for the preservation of biological structure: Theory and practice. Journal of Electron Microscopy Technique 13, 165–174. https://doi.org/10.1002/jemt.1060130305

Dean, J., 1992. Biology of mammalian fertilization: role of the zona pellucida. J. Clin. Invest. 89, 1055–1059. https://doi.org/10.1172/JCI115684

Denk, W., Briggman, K.L., Helmstaedter, M., 2012. Structural neurobiology: missing link to a mechanistic understanding of neural computation. Nature Reviews Neuroscience 13, 351–358. https://doi.org/10.1038/nrn3169

Dierich, A., Sairam, M.R., Monaco, L., Fimia, G.M., Gansmuller, A., LeMeur, M., Sassone-Corsi, P., 1998. Impairing follicle-stimulating hormone (FSH) signaling in vivo: Targeted disruption of the FSH receptor leads to aberrant gametogenesis and hormonal imbalance. Proc Natl Acad Sci U S A 95, 13612–13617.

Dong, J., Albertini, D.F., Nishimori, K., Kumar, T.R., Lu, N., Matzuk, M.M., 1996. Growth differentiation factor-9 is required during early ovarian folliculogenesis. Nature 383, 531–535. https://doi.org/10.1038/383531a0

Egbert, J.R., Shuhaibar, L.C., Edmund, A.B., Van Helden, D.A., Robinson, J.W., Uliasz, T.F., Baena, V., Geerts, A., Wunder, F., Potter, L.R., Jaffe, L.A., 2014. Dephosphorylation and inactivation of NPR2 guanylyl cyclase in granulosa cells contributes to the LH-induced decrease in cGMP that causes resumption of meiosis in rat oocytes. Development 141, 3594–3604. https://doi.org/10.1242/dev.112219

El-Hayek, S., Yang, Q., Abbassi, L., FitzHarris, G., Clarke, H.J., 2018. Mammalian Oocytes Locally Remodel Follicular Architecture to Provide the Foundation for Germline-Soma Communication. Current Biology 28, 1124-1131.e3. https://doi.org/10.1016/j.cub.2018.02.039

Eppig, J.J., 1994. Oocyte-somatic cell communication in the ovarian follicles of mammals. Seminars in Developmental Biology 5, 51–59. https://doi.org/10.1006/sedb.1994.1007

Eppig, J. J., Chesnel, F., Hirao, Y., O'Brien, M.J., Pendola, F.L., Watanabe, S., Wigglesworth, K., 1997. Oocyte control of granulosa cell development: how and why. Hum. Reprod. 12, 127–132.

Eppig, John J., Wigglesworth, K., Pendola, F., Hirao, Y., 1997. Murine Oocytes Suppress Expression of Luteinizing Hormone Receptor Messenger Ribonucleic Acid by Granulosa Cells. Biol Reprod 56, 976–984. https://doi.org/10.1095/biolreprod56.4.976

Fortune, J.E., Armstrong, D.T., 1978. Hormonal Control of 17β-Estradiol Biosynthesis in Proestrous Rat Follicles: Estradiol Production by Isolated Theca Versus Granulosa. Endocrinology 102, 227–235. https://doi.org/10.1210/endo-102-1-227

Gosden, R.G., Hunter, R.H., Telfer, E., Torrance, C., Brown, N., 1988. Physiological factors underlying the formation of ovarian follicular fluid. J. Reprod. Fertil. 82, 813–825. https://doi.org/10.1530/jrf.0.0820813

Griffin, J., Emery, B.R., Huang, I., Peterson, C.M., Carrell, D.T., 2006. Comparative analysis of follicle morphology and oocyte diameter in four mammalian species (mouse, hamster, pig, and human). Journal of Experimental & Clinical Assisted Reproduction 3, 2. https://doi.org/10.1186/1743-1050-3-2

Hadek, R., 1965. The Structure of the Mammalian Egg, in: Bourne, G.H., Danielli, J.F. (Eds.), International Review of Cytology. Academic Press, pp. 29–71. https://doi.org/10.1016/S0074-7696(08)60551-3

Hambleton, R., Krall, J., Tikishvili, E., Honeggar, M., Ahmad, F., Manganiello, V.C., Movsesian, M.A., 2005. Isoforms of cyclic nucleotide phosphodiesterase PDE3 and their contribution to cAMP hydrolytic activity in subcellular fractions of human myocardium. J. Biol. Chem. 280, 39168–39174. https://doi.org/10.1074/jbc.M506760200

Harder, N., Mora-Bermúdez, F., Godinez, W.J., Wünsche, A., Eils, R., Ellenberg, J., Rohr, K., 2009. Automatic analysis of dividing cells in live cell movies to detect mitotic delays and correlate phenotypes in time. Genome Res 19, 2113–2124. https://doi.org/10.1101/gr.092494.109

Hardy, K., Fenwick, M., Mora, J., Laird, M., Thomson, K., Franks, S., 2017. Onset and Heterogeneity of Responsiveness to FSH in Mouse Preantral Follicles in Culture. Endocrinology 158, 134–147. https://doi.org/10.1210/en.2016-1435

Hartmann, J.F., Gwatkin, R.B.L., Hutchison, C.F., 1972. Early Contact Interactions between Mammalian Gametes In Vitro: Evidence That the Vitellus Influences Adherence between Sperm and Zona Pellucida. PNAS 69, 2767–2769. https://doi.org/10.1073/pnas.69.10.2767

Hawkins, S.M., Matzuk, M.M., 2008. Menstrual Cycle: Basic Biology. Ann N Y Acad Sci 1135, 10–18. https://doi.org/10.1196/annals.1429.018

Holt, J.E., Lane, S.I.R., Jones, K.T., 2013. The control of meiotic maturation in mammalian oocytes. Curr. Top. Dev. Biol. 102, 207–226. https://doi.org/10.1016/B978-0-12-416024-8.00007-6

Hoover, B., Baena, V., Kaelberer, M.M., Getaneh, F., Chinchilla, S., Bohórquez, D.V., 2017. The intestinal tuft cell nanostructure in 3D. Sci Rep 7. https://doi.org/10.1038/s41598-017-01520-x

Horner, K., Livera, G., Hinckley, M., Trinh, K., Storm, D., Conti, M., 2003. Rodent oocytes express an active adenylyl cyclase required for meiotic arrest. Dev. Biol. 258, 385–396. https://doi.org/10.1016/s0012-1606(03)00134-9

Hung, V., Udeshi, N.D., Lam, S.S., Loh, K.H., Cox, K.J., Pedram, K., Carr, S.A., Ting, A.Y., 2016. Spatially resolved proteomic mapping in living cells with the engineered peroxidase APEX2. Nat Protoc 11, 456–475. https://doi.org/10.1038/nprot.2016.018

Hunzicker-Dunn, M., Maizels, E.T., 2006. FSH signaling pathways in immature granulosa cells that regulate target gene expression: branching out from protein kinase A. Cell. Signal. 18, 1351–1359. https://doi.org/10.1016/j.cellsig.2006.02.011

Hunzicker-Dunn, M., Mayo, K., 2006. CHAPTER 14 - Gonadotropin Signaling in the Ovary, in: Neill, J.D. (Ed.), Knobil and Neill's Physiology of Reproduction (Third Edition). Academic Press, St Louis, pp. 547–592. https://doi.org/10.1016/B978-012515400-0/50019-1

Hwang, B., Lee, J.H., Bang, D., 2018. Single-cell RNA sequencing technologies and bioinformatics pipelines. Experimental & Molecular Medicine 50, 1–14. https://doi.org/10.1038/s12276-018-0071-8

Inaba, M., Buszczak, M., Yamashita, Y.M., 2015. Nanotubes mediate niche-stem cell signaling in the Drosophila testis. Nature 523, 329–332. https://doi.org/10.1038/nature14602

Jaffe, L.A., Egbert, J.R., 2017. Regulation of Mammalian Oocyte Meiosis by Intercellular Communication Within the Ovarian Follicle. Annual Review of Physiology 79, 237–260. https://doi.org/10.1146/annurev-physiol-022516-034102

Jiang, X., Dias, J.A., He, X., 2014. Structural biology of glycoprotein hormones and their receptors: insights to signaling. Mol. Cell. Endocrinol. 382, 424–451. https://doi.org/10.1016/j.mce.2013.08.021

Kasthuri, N., Hayworth, K.J., Berger, D.R., Schalek, R.L., Conchello, J.A., Knowles-Barley, S., Lee, D., Vázquez-Reina, A., Kaynig, V., Jones, T.R., Roberts, M., Morgan, J.L., Tapia, J.C., Seung, H.S., Roncal, W.G., Vogelstein, J.T., Burns, R., Sussman, D.L., Priebe, C.E., Pfister, H., Lichtman, J.W., 2015. Saturated Reconstruction of a Volume of Neocortex. Cell 162, 648–661. https://doi.org/10.1016/j.cell.2015.06.054

Kellenberger, E., Johansen, R., Maeder, M., Bohrmann, B., Stauffer, E., Villiger, W., 1992. Artefacts and morphological changes during chemical fixation. J Microsc 168, 181–201. https://doi.org/10.1111/j.1365-2818.1992.tb03260.x

Kidder, G.M., Mhawi, A.A., 2002. Gap junctions and ovarian folliculogenesis. Reproduction 123, 613–620. https://doi.org/10.1530/rep.0.1230613

Kornberg, T.B., 2017. Distributing signaling proteins in space and time: the province of cytonemes. Curr. Opin. Genet. Dev. 45, 22–27. https://doi.org/10.1016/j.gde.2017.02.010

Lam, S.S., Martell, J.D., Kamer, K.J., Deerinck, T.J., Ellisman, M.H., Mootha, V.K., Ting, A.Y., 2015. Directed evolution of APEX2 for electron microscopy and proximity labeling. Nat. Methods 12, 51–54. https://doi.org/10.1038/nmeth.3179

Lipner, H., Cross, N.L., 1968. Morphology of the membrana granulosa of the ovarian follicle. Endocrinology 82, 638–641. https://doi.org/10.1210/endo-82-3-638

Liu, X., Xie, F., Zamah, A.M., Cao, B., Conti, M., 2014. Multiple pathways mediate luteinizing hormone regulation of cGMP signaling in the mouse ovarian follicle. Biol. Reprod. 91, 9. https://doi.org/10.1095/biolreprod.113.116814

Macaulay, A.D., Gilbert, I., Caballero, J., Barreto, R., Fournier, E., Tossou, P., Sirard, M.-A., Clarke, H.J., Khandjian, É.W., Richard, F.J., Hyttel, P., Robert, C., 2014. The Gametic Synapse: RNA Transfer to the Bovine Oocyte. Biol Reprod 91, 90. https://doi.org/10.1095/biolreprod.114.119867

Martell, J.D., Deerinck, T.J., Lam, S.S., Ellisman, M.H., Ting, A.Y., 2017. Electron microscopy using the genetically encoded APEX2 tag in cultured mammalian cells. Nature Protocols 12, 1792–1816. https://doi.org/10.1038/nprot.2017.065

Masciarelli, S., Horner, K., Liu, C., Park, S.H., Hinckley, M., Hockman, S., Nedachi, T., Jin, C., Conti, M., Manganiello, V., 2004. Cyclic nucleotide phosphodiesterase 3A–deficient mice as a model of female infertility. J Clin Invest 114, 196–205. https://doi.org/10.1172/JCI200421804

Mayerhofer, A., Garfield, R.E., 1995. Immunocytochemical analysis of the expression of gap junction protein connexin 43 in the rat ovary. Mol. Reprod. Dev. 41, 331–338. https://doi.org/10.1002/mrd.1080410308

McDole, K., Guignard, L., Amat, F., Berger, A., Malandain, G., Royer, L.A., Turaga, S.C., Branson, K., Keller, P.J., 2018. In Toto Imaging and Reconstruction of Post-Implantation Mouse Development at the Single-Cell Level. Cell 175, 859-876.e33. https://doi.org/10.1016/j.cell.2018.09.031

McDonald, K., 1999. High-pressure freezing for preservation of high resolution fine structure and antigenicity for immunolabeling. Methods Mol. Biol. 117, 77–97. https://doi.org/10.1385/1-59259-201-5:77

Mehlmann, L.M., Saeki, Y., Tanaka, S., Brennan, T.J., Evsikov, A.V., Pendola, F.L., Knowles, B.B., Eppig, J.J., Jaffe, L.A., 2004. The Gs-Linked Receptor GPR3 Maintains Meiotic Arrest in Mammalian Oocytes. Science 306, 1947–1950. https://doi.org/10.1126/science.1103974

Mora, J.M., Fenwick, M.A., Castle, L., Baithun, M., Ryder, T.A., Mobberley, M., Carzaniga, R., Franks, S., Hardy, K., 2012. Characterization and Significance of Adhesion and Junction-Related Proteins in Mouse Ovarian Follicles. Biol Reprod 86. https://doi.org/10.1095/biolreprod.111.096156

Motta, P.M., Makabe, S., Naguro, T., Correr, S., 1994. Oocyte Follicle Cells Association during Development of Human Ovarian Follicle. A Study by High Resolution Scanning and Transmission Electron Microscopy. Archives of Histology and Cytology 57, 369–394. https://doi.org/10.1679/aohc.57.369

Niedenberger, B.A., Cook, K., Baena, V., Serra, N.D., Velte, E.K., Agno, J.E., Litwa, K.A., Terasaki, M., Hermann, B.P., Matzuk, M.M., Geyer, C.B., 2018. Dynamic cytoplasmic projections connect mammalian spermatogonia in vivo. Development 145, dev161323. https://doi.org/10.1242/dev.161323

Norris, R.P., Freudzon, M., Nikolaev, V.O., Jaffe, L.A., 2010. Epidermal growth factor receptor kinase activity is required for gap junction closure and for part of the decrease in ovarian follicle cGMP in response to LH. Reproduction 140, 655–662. https://doi.org/10.1530/REP-10-0288

Norris, R.P., Ratzan, W.J., Freudzon, M., Mehlmann, L.M., Krall, J., Movsesian, M.A., Wang, H., Ke, H., Nikolaev, V.O., Jaffe, L.A., 2009. Cyclic GMP from the surrounding somatic cells regulates cyclic AMP and meiosis in the mouse oocyte. Development 136, 1869–1878. https://doi.org/10.1242/dev.035238

Park, J.-Y., Su, Y.-Q., Ariga, M., Law, E., Jin, S.-L.C., Conti, M., 2004. EGF-like growth factors as mediators of LH action in the ovulatory follicle. Science 303, 682–684. https://doi.org/10.1126/science.1092463

Paul, D., Baena, V., Ge, S., Jiang, X., Jellison, E.R., Kiprono, T., Agalliu, D., Pachter, J.S., 2016. Appearance of claudin-5+ leukocytes in the central nervous system during neuroinflammation: a novel role for endothelial-derived extracellular vesicles. J Neuroinflammation 13. https://doi.org/10.1186/s12974-016-0755-8

Peng, J., Li, Q., Wigglesworth, K., Rangarajan, A., Kattamuri, C., Peterson, R.T., Eppig, J.J., Thompson, T.B., Matzuk, M.M., 2013. Growth differentiation factor 9:bone morphogenetic protein 15 heterodimers are potent regulators of ovarian functions. PNAS 110, E776–E785. https://doi.org/10.1073/pnas.1218020110

Revelli, A., Piane, L.D., Casano, S., Molinari, E., Massobrio, M., Rinaudo, P., 2009. Follicular fluid content and oocyte quality: from single biochemical markers to metabolomics. Reprod Biol Endocrinol 7, 40. https://doi.org/10.1186/1477-7827-7-40

Richards, J.S., Pangas, S.A., 2010. The ovary: basic biology and clinical implications. J Clin Invest 120, 963–972. https://doi.org/10.1172/JCI41350

Richards, J.S., Ren, Y.A., Candelaria, N., Adams, J.E., Rajkovic, A., 2018. Ovarian Follicular Theca Cell Recruitment, Differentiation, and Impact on Fertility: 2017 Update. Endocrine Reviews 39, 1–20. https://doi.org/10.1210/er.2017-00164

Robinson, J.W., Zhang, M., Shuhaibar, L.C., Norris, R.P., Geerts, A., Wunder, F., Eppig, J.J., Potter, L.R., Jaffe, L.A., 2012. Luteinizing hormone reduces the activity of the NPR2 guanylyl cyclase in mouse ovarian follicles, contributing to the cyclic GMP decrease that promotes resumption of meiosis in oocytes. Dev. Biol. 366, 308–316. https://doi.org/10.1016/j.ydbio.2012.04.019

Rodgers, R.J., Irving-Rodgers, H.F., 2010. Formation of the Ovarian Follicular Antrum and Follicular Fluid. Biol Reprod 82, 1021–1029. https://doi.org/10.1095/biolreprod.109.082941

Russell, D.L., Doyle, K.M.H., Gonzales-Robayna, I., Pipaon, C., Richards, J.S., 2003. Egr-1 Induction in Rat Granulosa Cells by Follicle-Stimulating Hormone and Luteinizing Hormone: Combinatorial Regulation By Transcription Factors Cyclic Adenosine 3′,5′-Monophosphate Regulatory Element Binding Protein, Serum Response Factor, Sp1, and Early Growth Response Factor-1. Mol Endocrinol 17, 520–533. https://doi.org/10.1210/me.2002-0066

Sanders, T.A., Llagostera, E., Barna, M., 2013. Specialized filopodia direct long-range transport of SHH during vertebrate tissue patterning. Nature 497, 628–632. https://doi.org/10.1038/nature12157

Shuhaibar, L.C., Egbert, J.R., Edmund, A.B., Uliasz, T.F., Dickey, D.M., Yee, S.-P., Potter, L.R., Jaffe, L.A., 2016. Dephosphorylation of juxtamembrane serines and threonines of the NPR2 guanylyl cyclase is required for rapid resumption of oocyte meiosis in response to luteinizing hormone. Developmental Biology 409, 194–201. https://doi.org/10.1016/j.ydbio.2015.10.025

Shuhaibar, L.C., Egbert, J.R., Norris, R.P., Lampe, P.D., Nikolaev, V.O., Thunemann, M., Wen, L., Feil, R., Jaffe, L.A., 2015. Intercellular signaling via cyclic GMP diffusion through gap junctions restarts meiosis in mouse ovarian follicles. Proc Natl Acad Sci U S A 112, 5527–5532. https://doi.org/10.1073/pnas.1423598112

Simon, A.M., Goodenough, D.A., Li, E., Paul, D.L., 1997. Female infertility in mice lacking connexin 37. Nature; London 385, 525–9. http://dx.doi.org/10.1038/385525a0

Simon, A.M., Hwudaurw Chen, Jackson, C.L., 2006. Cx37 and Cx43 Localize to Zona Pellucida in Mouse Ovarian Follicles. Cell Communication & Adhesion 13, 61–77. https://doi.org/10.1080/15419060600631748

Titze, B., Genoud, C., 2016. Volume scanning electron microscopy for imaging biological ultrastructure. Biology of the Cell 108, 307–323. https://doi.org/10.1111/boc.201600024

Vaccari, S., Weeks, J.L., Hsieh, M., Menniti, F.S., Conti, M., 2009. Cyclic GMP Signaling Is Involved in the Luteinizing Hormone-Dependent Meiotic Maturation of Mouse Oocytes. Biol Reprod 81, 595–604. https://doi.org/10.1095/biolreprod.109.077768

Vitt, U.A., Mazerbourg, S., Klein, C., Hsueh, A.J.W., 2002. Bone morphogenetic protein receptor type II is a receptor for growth differentiation factor-9. Biol. Reprod. 67, 473–480.

Wigglesworth, K., Lee, K.-B., Emori, C., Sugiura, K., Eppig, J.J., 2015. Transcriptomic Diversification of Developing Cumulus and Mural Granulosa Cells in Mouse Ovarian Follicles. Biol Reprod 92. https://doi.org/10.1095/biolreprod.114.121756

Yalçın, B., Zhao, L., Stofanko, M., O'Sullivan, N.C., Kang, Z.H., Roost, A., Thomas, M.R., Zaessinger, S., Blard, O., Patto, A.L., Sohail, A., Baena, V., Terasaki, M., O'Kane, C.J., 2017. Modeling of axonal endoplasmic reticulum network by spastic paraplegia proteins. Elife 6. https://doi.org/10.7554/eLife.23882

Yan, C., Wang, P., DeMayo, J., DeMayo, F.J., Elvin, J.A., Carino, C., Prasad, S.V., Skinner, S.S., Dunbar, B.S., Dube, J.L., Celeste, A.J., Matzuk, M.M., 2001. Synergistic Roles of Bone Morphogenetic Protein 15 and Growth Differentiation Factor 9 in Ovarian Function. Mol Endocrinol 15, 854–866. https://doi.org/10.1210/mend.15.6.0662

Yanagishita, M., Hascall, V.C., Rodbard, D., 1981. Biosynthesis of proteoglycans by rat granuloma cells cultured in vitro: modulation by gonadotropins, steroid hormones, prostaglandins, and a cyclic nucleotide. Endocrinology 109, 1641–1649. https://doi.org/10.1210/endo-109-5-1641

Yoshino, M., Mizutani, T., Yamada, K., Tsuchiya, M., Minegishi, T., Yazawa, T., Kawata, H., Sekiguchi, T., Kajitani, T., Miyamoto, K., 2002. Early growth response gene-1 regulates the expression of the rat luteinizing hormone receptor gene. Biol. Reprod. 66, 1813–1819. https://doi.org/10.1095/biolreprod66.6.1813

Zhang, M., Su, Y.-Q., Sugiura, K., Xia, G., Eppig, J.J., 2010. Granulosa Cell Ligand NPPC and Its Receptor NPR2 Maintain Meiotic Arrest in Mouse Oocytes. Science 330, 366–369. https://doi.org/10.1126/science.1193573